A microbial approach to subglacial biogeochemistry

Methane exports, microbial assemblages, and geochemical energy sources of a Greenland subglacial catchment

By

GUILLAUME LAMARCHE-GAGNON

School of Geographical Sciences
UNIVERSITY OF BRISTOL

A dissertation submitted to the University of Bristol in accordance with the requirements of the degree of DOCTOR OF PHILOSOPHY in the School of Geographical Sciences

April 2019

Word count: 36, 000

Abstract

The past two decades demonstrated how subglacial environments are not devoid of life, that the bed of glaciers and ice sheets harbour active microbial communities and in turn, that these ecosystems may impact on biogeochemical cycles outside of the cryosphere. Despite their putative importance, most of our understanding of subglacial microbial communities derive from conceptual models, and there remains large uncertainties as to how widespread and (biogeochemically) influential these microorganisms are beneath the ice, as well as to how (or if) such communities can remain biogeochemically "relevant" over glacial timescales. The present thesis aimed at assessing the metabolic strategies employed by, as well as the impact of, microbial communities indigenous to subglacial ecosystems, and to study the hydrological, geochemical, and mechanical processes that shape and sustain such communities beneath the ice. More specifically, research here focused on a large, well-studied, catchment of the Greenland Ice Sheet (GrIS) to evaluate the methanogenic footprint of the catchment, the make-up of the microbial communities exported from bulk meltwater runoff, as well as the influence of bedrock comminution in fuelling subglacial microbial communities. High-resolution *in situ* sensor measurements of bulk runoff hydrochemistry, as well as stable-isotope and molecular analyses, revealed the GrIS catchment to be a net source of microbial methane to the atmosphere. Molecular (16S rRNA) analyses also hinted that chemolithotrophy centred on both iron and methane cycling likely plays a key role in sustaining local subglacial microbial populations beneath the ice, as well as how glacial hydrology can shape microbial communities beneath the catchment. Lastly, laboratory incubations indicated that crushing of bedrock material liberate bioavailable energy (e.g. H_2), nutrients (NO_3^- and PO_4^{3-}) and also organic carbon (acetate and formate) to indigenous subglacial populations indicating that bedrock comminution by moving ice masses likely act as a microbial fuel to subglacial ecosystems. All in all, results here further the importance of subglacial biota in the context of global biogeochemical cycles, as well as support previous conceptual models on the microbial distribution and energy sources beneath today's ice masses.

Dedication and Acknowledgements

I would first like to thank my supervisor, Jemma Wadham. I obviously need to thank her for the opportunity of carrying this research to begin with, as well as the many opportunities that followed. I need to thank her for her continuous support and (sometimes scarily blind) trust. I'm grateful (and humbled) to have had the chance to work 'alongside' someone that changed the way I now try to understand the natural world (and here I'll disregard comments on how terrifying that may sound...). I believe I now better understand the meaning of the word 'mentor', thank you Jemma.

I of course also need to thank everyone that contributed directly or indirectly to these last years of research, on fieldwork, in the lab, in passing, in sticking around. It was a particular treat to be introduced to (British) Greenland fieldwork by such a fearless team. Thank you Jon, thank you Liz, thank you Alex. And such a pleasure to extend the stay with that merry bunch; thank you Tyler, Jakub, Jade (well, Marek as well if I must...(and I do)). Thank you also to my co-supervisor, Alex Anesio, for unquestionable support during the thesis but especially during that first year, providing refugia from (bio)geochemists when discussing microbiology was still an option. On that note thank you as well to Mischa, which renewed such microbiological interest by bringing these discussions back to the forefront.

Thank you to colleagues that became friends, Jon, Ale, Gaz, Stefan, Sam, Sarah. A special thanks to Mike for the endless discussions on "what lies beneath" (still confused as to whether or not sediments do lie beneath...); obviously thank you Mike for all the rest. Thanks to Moya and Bea, friends in the lab but mostly out of it.

A particular shout again to both Jon Telling and Jon Hawkings, for scientific guidance and support. And I also need to acknowledge all of the co-authors, for the work, but mostly for the research and collaboration opportunities.

Lastly thank you to the taxpayers of Québec and the United-Kingdom that made it possible for me to sustain (and enjoy) myself during these last years. I would like to acknowledge the following institutions for financial support in the present thesis: Fond québécois de recherche nature et technologie (FRQNT), the University of Bristol, and the University of Bristol Alumni and DARO foundations.

Author's declaration

I declare that the work in this dissertation was carried out in accordance with the requirements of the University's Regulations and Code of Practice for Research Degree Programmes and that it has not been submitted for any other academic award. Except where indicated by specific reference in the text, the work is the candidate's own work. Work done in collaboration with, or with the assistance of, others, is indicated as such. Any views expressed in the dissertation are those of the author.

SIGNED: ..... DATE:.....

Table of Contents

1. Context and research objectives

Glaciers, ice-caps and ice-sheets cover over a tenth of Earth landmasses, covered up to 30% during the last glacial maxima, and even potentially the entire planet's surface in Snowball Earth events (Hoffman et al., 1998). More than frozen systems, glacial environments are now considered to significantly impact biogeochemical cycles on a planetary scale (e.g. by releasing large amounts of bioavailable nutrients and trace minerals to surrounding oceans (Wadham et al., 2013; Hawkings et al., 2014)). Glacial systems are also being recognised as intrinsic members of the biosphere, providing habitats for microbial life above, beneath, and even potentially within the ice (Hodson et al., 2008; Anesio and Laybourn-Parry, 2012; Boetius et al., 2015). Microbial and biogeochemical studies on glacial systems remain nonetheless scarce and our understanding of the biological cryosphere limited. Arguments for widespread active microbial communities under glaciers and ice sheets, as well as the extent of microbial influence on subglacial and downstream biogeochemical cycles, need firming up (Skidmore et al., 2010). Among others, preliminary work has indicated that significant amounts of microbially derived greenhouse gases (e.g. methane) may be capped beneath ice sheets, potentially derived from microbially metabolised buried organic carbon and accumulating over glacial periods (Wadham et al., 2008; Wadham et al., 2012). Of special interest are investigations assessing the roles of sub-ice-sheet microbes in influencing global biogeochemical cycles, such as their potential impact on solute and nutrient fluxes in glacier discharges, or emissions of greenhouse gases (e.g. methane) and their potential impact on future climate feedback loops.

The general goal of this research was to evaluate the biological footprint of putatively active subglacial microbial communities on (bio)geochemical cycles occurring beneath glaciers and ice-sheets, as well as the (a)biotic factors that shape these indigenous communities. Special attention was given to the production and fate of subglacial methane, and major nutrients, and their impact on community structure and composition beneath the ice. Overall, the research combined field measurements (e.g. *in situ* methane concentrations), molecular (16S rRNA) analyses and incubation experiments to evaluate the microbial signals and effects from beneath the catchment of the Leverett Glacier (LG) in Southwest Greenland (see section 3.7.1.1 for site description). Results here are presented in the form of three publication, or "publication like", chapters (chapters 3-5), each addressing specific research objectives:

Objective i (chapter 3): To determine the levels, sources (e.g. biotic vs abiotic) and fate of subglacial methane produced beneath the LG catchment. This objective only indirectly addressed the microbiology of the system, and focused more on the hydrological and geochemical processes surrounding methane exports from LG.

Objective ii (chapter 4): To identify the principal microbial populations and metabolic pathways that characterise LG subglacial communities, as well as the potential changes in community structure resulting from changes in subglacial environmental (e.g. hydrological) conditions. This was performed via molecular and geochemical analyses of field-collected samples.

Objective iii (chapter 5): To determine the effects of glacier-driven mineral comminution, and concomitant hydrogen and nutrient releases, on subglacial LG microbial communities. This was performed via laboratory "rock-crushing" experiments and incubations.

2. Scientific background

2.1 Subglacial habitats

The extent, distribution, and quantities of cells subglacially mainly depend on the amount of liquid water (and associated sediments and tills) present beneath the ice. Whereas cold-base regions of glaciers and ice sheets are virtually frozen to the bed, temperate and polythermal ice masses can overlay significant volumes of basal liquid water, kept above the pressure melting point via geothermal and frictional heating (Hodson et al., 2008).

2.1.1 Liquid waters beneath the ice, subglacial hydrology (and oxygen supply)

The differences in supraglacial connectivity, drainage pathways, and levels of isolation beneath the ice directly affect the potential ecological niches found in subglacial systems. A primary consequence of subglacial isolation relates to the scarcity of renewed oxygen supply, which dictates the redox state of potential habitats beneath the ice. Isolated regions of the bed sheltered from supraglacial inputs (e.g. ice-sheet interiors) are considered mostly anoxic, as potentially small supply of oxygen (e.g. from basal melting of the overlaying ice) should be quickly consumed biogeochemically (e.g. via sulphide oxidation; see below) (Wadham et al., 2013).

2.1.1.1 Connection to the supraglacial environment

Supraglacial melt water can enter the subglacial system in temperate and polythermal glaciers, as well as in the margin of the Greenland Ice Sheet (GrIS), reaching the glacier's bed via crevasses and moulins during the melt season, and annually altering the distribution and connectivity of subglacial water channels, alongside periodically supplying the subglacial system with supraglacially derived nutrients, gases, as well as allochthonous cells (Tranter et al., 2005; Das et al., 2008). These latter subglacial hydrological systems are normally partitioned into two components in the context of subglacial drainage pathways: slow-inefficient and rapid-efficient components, respectively referred to as distributed (inefficient) and channelised (efficient) drainage (Nienow et al., 1998; Das et al., 2008). The distributed system is often portrayed as slow-moving, tortuous flow paths draining so called "long residence time" waters, which have remained at the glacier/ice-sheet bed for at least one winter. Such waters are characterised by high solute concentrations derived from the denudation of mineral surfaces via biogeochemical weathering during prolonged contact with bedrock, tills and flour (finely sized - down to sub-

micron levels - and highly geochemically reactive sediments) generated by physical plucking and grinding of the bed by the moving overlaying ice (Tranter et al., 2002).

Waters from either system consequently bear specific geochemical signatures depending on their residence time subglacially. Hydrolysis of carbonate bearing minerals is considered the first and quickest weathering reaction on freshly exposed mineral surfaces in subglacial systems (Tranter et al., 2002). Carbonation reactions, but perhaps more importantly sulphide oxidation, can further contribute to carbonate dissolution beneath the ice, especially when distributed systems become supplied with fully oxygenated surface waters and atmospheric carbon dioxide (see below); sulphide oxidation coupled to iron reduction following oxygen depletion is also considered to further contribute to dissolution reactions (Bottrell and Tranter, 2002). The more rapid dissolution kinetics of carbonates (over silicates) tend to enrich subglacial waters with divalent cations, which normally characterise the runoff of alpine and smaller arctic glaciers (Tranter et al., 2002; Dubnick et al., 2017). Beneath larger ice masses (e.g. ice-sheets), longer water residence times there are believed to promote the slower dissolution of silicate mineral once carbonate dissolution has been exhausted (or saturation with respect to calcite achieved), normally releasing monovalent cations (Wadham et al., 2010a; Wadham et al., 2010b). The degree of carbonate and silicate dissolution can therefore inform on the residence time of subglacial waters exported from beneath the ice (Hatton et al., 2019); such concept is further explored and utilised in chapter 4.

2.1.1.2 Evolution of subglacial drainage systems

In the early melt season, meltwaters draining out of subglacial catchments are mostly sourced from distributed-system waters located near the margin of the ice. As the melt season progresses, these slow, inefficient pathways are supplanted by the channelised drainage system, mostly sourced from supraglacial melt, and which progressively expands headwards following the retreat of the snowline on the ice surface (Nienow et al., 1998; Chandler et al., 2013). Rapid routing of supraglacial waters to the bed, sometimes accentuated during episodic supraglacial lake drainage events (see section 3.7.2.2) (Nienow et al., 1998; Bartholomew et al., 2011; Hoffman et al., 2018), connects distributed sources to the main drainage pathways in the channelised system (Fig. 2.1). Earlier in the melt season, large inputs of supraglacial waters to the bed exceed (pre) existing drainage channels' capacities, leading to momentary rises in water pressures at the bed exceeding that of the ice overburden pressure, which in turn increases basal sliding via ice elevation and bed lubrication, enhancing physical erosion from the accelerating ice (Chu, 2014; Nienow et al.,

2017). Whilst overpressure is maintained within main drainage channels, newly inputted supraglacial waters is forced into flanking subglacial tills and sediments of the distributed system. In turn, pressure drops following channel expansion result in the drainage of distributed sources into main channelised flow paths following steepest hydraulic pressure gradients. Once fully expanded, diurnal changes in meltwater input to the bed alter the subglacial water pressure resulting in diurnal "replenishments" and drainages of distributed waters beneath the ice (Nienow et al., 2017). More nuances likely apply in explaining subglacial drainage behaviours, especially beneath larger ice masses, than a "simple two-component model" (Hoffman et al., 2016), but this dichotomic view of the subglacial system is considered accurate enough to contextualise the biogeochemical and microbial discussions of chapters 3 and 4. More details regarding the evolution of the hydrological system specific to Leverett Glacier (LG) studied here is included in section 3.7.2.2.

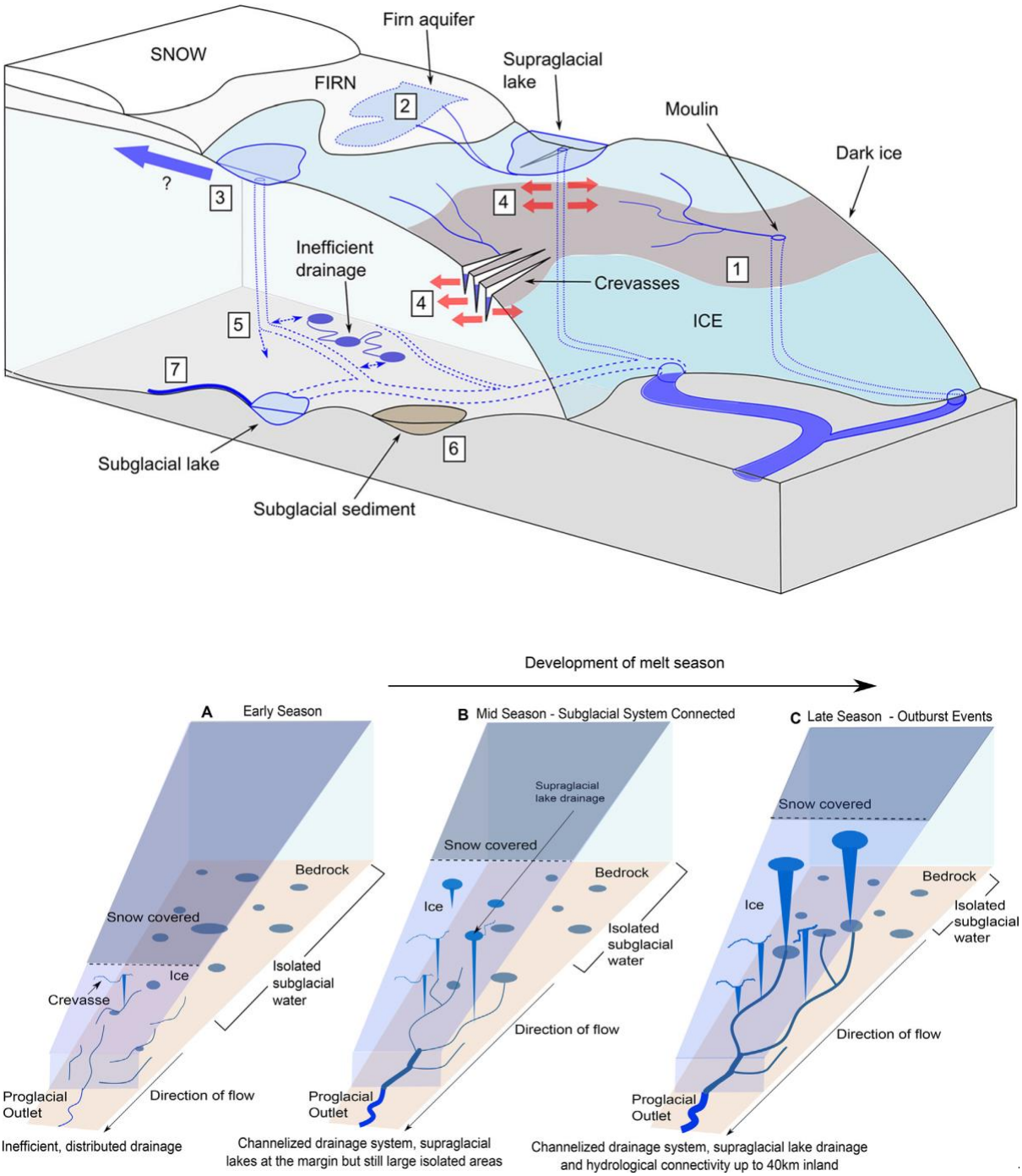

Figure 2. 1 Schematic diagrams of the different hydrological components in land-terminating glaciers of the GrIS.

Both diagrams illustrate conceptual views of distributed and channelised subglacial systems, as well as supraglacial water inputs to the bed during the melt season. The bottom diagram is meant to more specifically depict a transition from inefficient to efficient drainage system in the LG glacier. The top diagram is taken from Nienow et al. (2017) and the bottom one from Hatton et al. (2019).

2.1.1.3 Distribution of microbial niches within an evolving subglacial drainage system

In terms of potential ecological niches available to microbes beneath the ice, transitions from distributed to channelised drainage pathways offer a range of redox conditions dictated by the

supply and residence time of oxygenated supraglacial melt water subglacially. Tranter et al. (2005) postulated that hydrology indeed plays a first level control in shaping different ecological niches beneath the ice; this ecological niche gradient driven by changes in redox potentials was further conceptualised by Hodson et al. (2008). Figure 2.2 illustrates how different microbial populations may be distributed relative to subglacial drainage channels, with more anaerobic populations further away from channel centres (and aerobic ones constrained to channel margins or top sediment layers). Of interest here is the concept of a "channel marginal zone" surrounding main drainage pathways, a putative accumulation zone of till an sediments flanking subglacial conduits, somewhat akin to the river banks of non-glacial rivers, yet sandwiched between underlying bedrock and tills and overlaying ice (Hubbard et al., 1995; Tranter et al., 2005; Hodson et al., 2008). This hypothetical zone sits between the channelised and distributed system, and therefore likely undergoes largest and most dynamic changes in redox potential, as well as "buffering" exchanges of nutrients, ions, and cells in a similar fashion to hyporheic zones of rivers (Tranter et al., 2005; Hodson et al., 2008). These concepts surrounding microbial niches relative to subglacial drainage systems are further discussed as part of chapter 4.

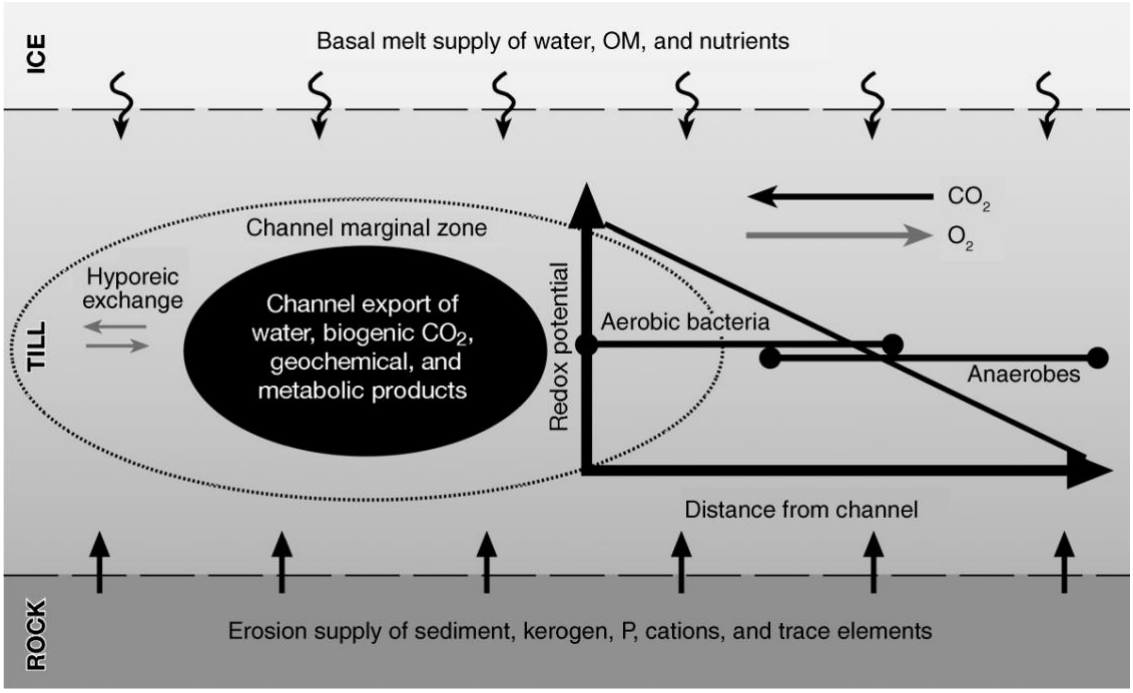

Figure 2. 2 Conceptual view of hydraulic exchange, redox conditions, and broad microbial metabolisms at the bed of hydrologically active ice masses; taken from Hodson et al. (2008). The depicted channel should probably be, at least partly, incised in the overlaying basal ice following classical views of "R", "H", or "N" subglacial channels (Fountain and Walder, 1998).

2.1.2 Microbial presence and activity in subglacial systems

Typical cell densities from polythermal and temperate glacier runoff and basal ice range from 10^4-10^7 cells mL^{-1} (Sharp et al., 1999; Skidmore et al., 2000; Hodson et al., 2008; Montross et al., 2013a). Studies on basal and silty layers of GrIS ice cores have revealed cells numbers as low as 10^3 and as high as 10^8 cells mL^{-1} from melted ice from NGRIP and GISP2 samples, respectively (Miteva et al., 2004; Tung et al., 2005; Christner et al., 2012). The cell density in subglacial sediments beneath the Kamp ice stream in Antarctica has been reported at 10^7 cells g^{-1} of sediments and that of the Subglacial Lake Whillans (SLW) waters at around 10^5 cells mL^{-1} (Lanoil et al., 2009; Christner et al., 2014). Overall, these ranges in cell concentrations are similar to those reported in other aquatic environments on Earth, and mostly larger than densities found in the open ocean, estimated to contain on the order of 10^5 cells mL^{-1} seawater (Whitman et al., 1998). Considering the entire Antarctic Ice Sheet (AIS) hydrological system, latest estimates put microbial abundances to 10^{26} to 10^{27} cells in subglacial Antarctica, numbers on par with, and potentially exceeding, those reported for all other terrestrial freshwater bodies on Earth combined (Whitman et al., 1998; Lanoil et al., 2009). How much of these subglacial biomasses truly constitute indigenous, active populations remains, however, debated (Skidmore et al., 2010).

The argument for an active subglacial biota arguably arose from conspicuous gas concentrations at the base of ice cores, disagreeing with expected atmospheric signatures, and suggesting microbial sources (Souchez et al., 1995a; Tison et al., 1998). It truly is the work of Sharp et al. (1999) on the Haut Glacier d'Arolla, however, that transformed the way we portrayed subglacial environments by exposing how bacteria indigenous to the glacier's subglacial system almost certainly impacted on weathering reactions beneath the ice. Laboratory-based experiments on subglacial samples have now confirmed that at least some of the cells from native subglacial communities are active under near *in situ* conditions, capable of both auto- and heterotrophic metabolism (e.g. Murray et al. (2012); Montross et al. (2013a); Skidmore et al. (2000)). Molecular surveys and geochemical assessments also argue for a subglacial biodiversity as diverse as the subglacial systems themselves, encompassing virtually all known metabolic lifestyles, with the exception of photosynthesis (Boetius et al., 2015) and incubation assays targeting specific metabolic processes from subglacially-derived samples have confirmed a wide range of chemolithotrophic capabilities from subglacial populations including nitrate reduction (denitrification), nitrification, pyrite oxidation, sulphate reduction, methanogenesis, as well as

iron reduction (Kivimaki, 2005; Boyd et al., 2010; Boyd et al., 2011; Stibal et al., 2012b; Mitchell et al., 2013; Nixon et al., 2016). More recently, an entire microbial ecosystem was confirmed to populate the water and sediments of SLW in Antarctica, with microbial populations capable of (an)aerobic, hetero- and autotrophic, as well as lithotrophic metabolisms (Christner et al., 2014), although exhibiting very low metabolic rates (Vick-Majors et al., 2016).

2.1.3 Carbon and energy sources beneath the ice

The subglacial environment is normally considered a nutrient poor, oligotrophic system. Aside from episodic supraglacial inputs in temperate and polythermal glaciers, subglacial ecosystems are dependent on glacially buried substrates for sustenance. However, a variety of geochemical reactions and substrates can, in theory, support microbial activity under glaciers. Physical weathering of the bed (abrasion, grinding or fracturing) by moving basal ice or overridden ice pressure exposes reactive mineral surfaces prone to further chemical transformation, supplying essential elements (N, P, S, etc.) and trace nutrients (e.g. Fe) to subglacial biota and downstream ecosystems (Wadham et al., 2010b). Local composition of bedrock (lithology), overridden paleosol, and sediments, necessarily dictate the nature of potentially bioavailable nutrients and energy sources subglacially (Wadham et al., 2010b; Mitchell et al., 2013). But it is also the mass of the overlaying ice, which in turn affects subglacial hydrology, that is considered a main control of water chemistry in subglacial systems and microbial colonisation of the bed (Tranter et al., 2005; Wadham et al., 2010b). That is, the presence, extent, provenance, and retention time of liquid water limit and shape microbial distribution, but also biogeochemical weathering reactions that are tightly coupled with O_2 and CO_2 levels beneath the ice, and will influence on the release of crustal nutrients (see section 2.1.1 above).

2.1.3.1 Organic carbon

Significant amounts of organic carbon (OC) are considered capped beneath today's ice masses. The bioavailability of such carbon is, however, thought tightly linked with the age of the overlying ice (i.e. residence time) and the type of overridden organic matter; relative simple soluble OC and simple polymers (e.g. hemicellulose) should be less recalcitrant than lignin and lignified cellulose (Wadham et al., 2008). The AIS is estimated to have overlain on the order of 21,000 Pg of OC upon glaciation, most of which in the form of relatively labile marine and lacustrine sediments (Wadham et al., 2012). In contrast, the overridden paleosols of the GrIS have been considered to contain more recalcitrant, less bioavailable OC (Wadham 2012). However, more

recent studies are challenging this view (Wadham et al., *In review*); Lawson et al. (2014) reported exports between ~ 0.3-1.5 Tg C yr^{-1} for the GrIS, mostly in the form of particulate organic carbon (POC), of which about 9% was considered readily bioavailable to indigenous microorganisms. Even if some of this exported OC originated from supraglacially formed carbon, most of the analysed POC was attributed a subglacial origin, mostly derived from eroded sources, as well as potentially from microbially fixed inorganic C (Lawson et al., 2014). Despite the presence of appreciable amounts of OC beneath ice masses, chemolithoautotrophic metabolisms are considered to dominate over heterotrophic ones in several subglacial environments (Hamilton et al., 2013; Boetius et al., 2015; Vick-Majors et al., 2016).

2.1.3.2 Inorganic energy sources

Sulphide oxidation (e.g. of pyrite) is often described as one of the most important chemical reaction in shaping subglacial habitats (Tranter et al., 2002; Tranter et al., 2005; Wadham et al., 2010b; Wadham et al., 2013). Not only chemically driven, the oxidation of sulphide minerals has also been shown to fuel chemolithotrophic aerobic respiration under alpine glaciers, a metabolic process that likely extends to a range of subglacial environments (Sharp et al., 1999; Mitchell et al., 2013; Boyd et al., 2014). The same process is thought to also apply anaerobically on larger spatial scales in subglacial anoxic regions where alternative oxidants (e.g. NO_3^-, Fe^{3+}) liberated by regelation and physicochemical weathering would be available (Tranter et al., 2005; Wadham et al., 2013; Nixon et al., 2016).

The bed of glaciers and ice-sheets are also considered rich in iron minerals, and iron-dependent metabolism has often been stated as playing a major role in fuelling subglacial communities (Tranter et al., 2005; Tung et al., 2006; Wadham et al., 2010b; Montross et al., 2013b; Nixon et al., 2016). The subglacial outflow Blood Falls, in Antarctica, represents one such environment where bacterial lifestyles are centred around iron-dependency and sulphur cycling (Mikucki et al., 2009). Hawkings et al. (2014) have shown that the GrIS, and most likely the AIS as well, export significant amounts of putatively bioavailable iron species to the surrounding oceans, again most likely liberated by crushing of the bed. Similarly, the GrIS has been reported to contribute large fluxes of putatively bioavailable phosphorus to downstream environments (Hawkings et al., 2016).

2.1.3.3 Unaccounted-for energy and nutrient sources from basal rock comminution

A recent study by Telling et al. (2015) have furthered the importance of rock comminution in providing energy sources to subglacial ecosystems. Significant amounts of (H_2) gas were indeed shown to be generated at 0°C upon wetting freshly grounded (bed)rock material, most likely as a result of rock-water reactions with freshly exposed free radicals from crushed silicate minerals. High concentrations of H_2 (~200-550 nM) have been reported from the base of the NGRIP ice core, centre Greenland (Christner et al., 2012), and comminution the ice-sheet bed by the moving ice could potentially explain the origin of this subglacial hydrogen. H_2 is an electron donor that fuels a variety of microbial metabolisms, including sulphate reduction and methanogenesis, and renewable supplies of minerally formed H_2 could be key in supporting a subglacially active biota (Conrad and Wetter, 1990; Telling et al., 2015). Mineral H_2 formation has been shown to support, and even be promoted by, microbial populations from the deep biosphere at higher temperatures (>20°C) (Parkes et al., 2011). Whether the same applies to colder subglacial habitats remains to be tested, but seems likely, and is one of the objective of chapter 5. In addition to H_2 generation, the grinding of glaciers' beds has also been hypothesised to increase organic carbon bioavailability via the mechanochemical "re-working" of overlain ancient carbon (Tranter, 2015).

2.2 Potential large-scale impacts of microbial activity beneath ice masses

If truly widespread beneath ice masses, the presence of an active biota has the potential to not only significantly affect subglacial geochemical processes *in situ*, but also on external systems, with potential global repercussions.

2.2.1 Impacts of biogeochemical weathering

As mentioned above, effects of microbial activity on weathering processes have been shown to not only be influenced by (e.g. indirectly via CO_2 generated during respiration), but also driven by, microbial respiration (Sharp et al., 1999; Tranter et al., 2002). Montross et al. (2013b) measured an eightfold increase in major cation release in biotic versus abiotic weathering incubations with glacial sediments of alpine and Norwegian glaciers, indicating significant microbial involvements in driving such reactions. However, microbial impacts on subglacial weathering are considered to be greater in larger, supraglacially isolated sub ice-sheet environments, where microbial metabolism would not only affect carbonate dissolution, but also

silicate dissolution post calcite saturation/depletion (Wadham et al., 2010b). Silicate minerals normally contain elevated amounts of iron, manganese, as well as trace nitrogen and potassium levels; silicate dissolution therefore leads to the release of bioavailable and essential nutrients, further supporting microbial populations (Wadham et al., 2010b; Wadham et al., 2013). The large-scale impacts of microbially-driven weathering can be more appreciated when considering subglacial exports to downstream environments (e.g. surrounding oceans), providing bioavailable nutrients and trace minerals to external systems. For example, it is estimated that between 14-37% of total solutes released from subglacial weathering processes in long residence time environments can be attributed to CO_2 releases from microbial respiration/fermentation and protons generated during biological sulphide oxidation (Wadham et al., 2010b). Furthermore, biological iron reduction subglacially may be key in replenishing the pool of bioavailable (and mobile) iron that can then be exported to iron-limited polar oceans in glacial runoff, impacting on the marine primary productivity around the Earth ice sheets (Wadham et al., 2013; Hawkings et al., 2014; Nixon et al., 2016).

2.2.2 Evidence for methane cycling beneath glaciers and ice sheets

The estimated amount of organic carbon (OC) present beneath the Earth's ice-sheets surpasses the permafrost global carbon pool by up to one order of magnitude (Wadham et al., *In review*). Most of this OC (~21,000 Pg) is thought to comprise overlaid marine sediments in Antarctica (Wadham et al., 2012), whereas the GrIS is believed to mostly overlay more modest stocks of soil carbon (~ 40 Pg OC (Wadham et al., *In review*)). Unlike in permafrost, however, most of this OC is not "locked away" in a frozen state, with geochemical conditions beneath the ice conducive to methanogenesis (i.e. wet, reducing; see previous sections). The hypothesised role of ice-sheets in the global methane cycle relies on the assumption that subglacial OC is converted to methane by methanogens (and/or via thermogenic reactions), which then accumulates as hydrates over long timescales under high pressures and low temperatures beneath the ice (Wadham et al., 2008; Wadham et al., 2012). Because methane is a powerful greenhouse gas, destabilisation of subglacial hydrates during periods of significant ice thinning and retreat, followed by methane release to the atmosphere, may have the potential to influence global climate during rapid deglaciation (Wadham et al., 2008; Wadham et al., 2012).

Evidence now points toward the presence of appreciable amounts of methane (capped) beneath all three of Earth's ice sheets. Earlier signs came from analyses of the Greenland GRIP ice-core,

which revealed CH_4 concentrations of 6000 ppmv in its basal region (Souchez et al., 1995a). Studies from the later drilling campaigns GISP2 and NGRIP also reported excess methane concentrations of respectively 11 600 ppmv and 70-79 nM (about 60 times CH_4 concentrations in air-equilibrated water) in refrozen basal meltwaters (Miteva et al., 2009; Christner et al., 2012). Overall, the origin of subglacial methane remains speculative. It is often unclear whether such large quantities of methane are currently and continuously being produced, or are mainly derived from older sources, capped upon glaciation (Wadham et al., 2008).

Most subglacial samples examined to date, however, did reveal the presence of viable methanogenic organisms. Methanogenesis have been shown in basal ice and water samples from Alpine, Arctic and Antarctic glaciers incubated under approximated *in situ* (cold) conditions (Boyd et al., 2010; Stibal et al., 2012b; Wadham et al., 2012). The putative activity of methanogenic populations was also supported by molecular data from basal sediments from the Robertson glacier, Canada (Hamilton et al., 2013). The presence of apparently active methanogenic archaea was found in bottom GISP2 ice-core samples (Tung et al., 2005), and the isotopic signature of the methane in both the GRIP and GISP2 cores were consistent with a microbial origin (respective $\delta^{13}C\text{-}CH_4$ of ~ -83‰ and -76‰) (Souchez et al., 2006; Miteva et al., 2009). The large sedimentary basins present under the Antarctica ice sheets have also been considered to source large amounts of methane, derived from the microbial and thermal conversion of buried organic carbon under *in situ* anoxic conditions (Wadham et al., 2012).

More recently, high concentrations of methane, alongside the detection of DNA sequences related to methanogenic archaea, were also found in the sediments of subglacial Lake Whillans (SLW) in Antarctica (Michaud et al., 2017). Elevated concentrations of methane of apparent subglacial origin were also detected near the southwestern margin of the GrIS, highlighting the fact that the GrIS might represent a source of atmospheric methane (Dieser et al., 2014). However, both studies have also reported the presence of active aerobic methane-oxidising populations, alluding to a potentially efficient microbial methane sink beneath and near the ice. Moreover, it seems likely that microbial anaerobic oxidation of methane (AOM) could also be carried out subglacially given the abundance of suitable electron acceptors, namely, sulphate, iron, manganese, and even potentially nitrate (Beal et al., 2009; Boyd et al., 2010; Ettwig et al., 2010; Wadham et al., 2013). All in all, it will be important to evaluate the sources, sinks, and fate of (microbial) methane beneath ice sheets; addressing those points was the main objective of the following section.

3. Greenland melt drives continuous export of methane from the ice-sheet bed

Guillaume Lamarche-Gagnon[1*], Jemma L. Wadham[1], Barbara Sherwood Lollar[2], Sandra Arndt[3], Peer Fietzek[4], Alexander D. Beaton[5], Andrew J. Tedstone[1], Jon Telling[6], Elizabeth A. Bagshaw[7], Jon R. Hawkings[1], Tyler J. Kohler[8], Jakub D. Zarsky[8], Matthew C. Mowlem[5], Alexandre M. Anesio[9], Marek Stibal[8]

[1]School of Geographical Sciences, University of Bristol, Bristol BS8 1SS, UK
[2]Department of Earth Sciences, University of Toronto, Toronto, M5S 3B1, Canada
[3]Department of Geoscience, Environment & Society, Université Libre de Bruxelles, Brussels, Belgium
[4]Kongsberg Maritime Contros GmbH, Kiel 24148, Germany
[5]National Oceanography Centre, Southampton SO14 3ZH, UK
[6]School of Natural and Environmental Sciences, Newcastle University, Newcastle NE1 7RU, UK
[7]School of Earth and Ocean Sciences, Cardiff University, Cardiff, CF10 3AT, UK
[8]Department of Ecology, Faculty of Science, Charles University, Prague, 128 44, Czechia
[9]Department of Environmental Sciences, Aarhus University, 4000 Roskilde, Denmark

3.1 Preface

For the most part, this section has been published in the journal *Nature* under the full citation:

Lamarche-Gagnon, G., Wadham, J.L., Sherwood Lollar, B., Arndt, S., Fietzek, P., Beaton, A.D., Tedstone, A.J., Telling, J., Bagshaw, E.A., Hawkings, J.R., Kohler, T.J., Zarsky, J.D., Mowlem, M.C., Anesio, A.M., and Stibal, M. (2019). Greenland melt drives continuous export of methane from the ice-sheet bed. Nature *565*, 73-77, doi: 10.1038/s41586-018-0800-0.

The post-print version including methods and supplementary information have been copied *verbatim*. A perspective section (section 3.8) not included in the published manuscript has been included following the article. Writing, experimental procedures, analyses and interpretations were performed by G. L. G., except for the modelling of subglacial methane hydrates and the analysis of stable isotopes. The section below summarises the authors' contributions:

Author contribution:

J.L.W. and G.L.G. designed the study. B.S.L. supervised stable-isotope analyses. S.A. performed the reaction-transport hydrate model calculations. P.F. assisted in the interpretation and analysis of the CONTROS HydroC®-CH_4 raw results. G.L.G., J.T., E.A.B., A.D.B., M.C.M. and J.R.H. conducted field logistical preparations. J.L.W., J.T. and M.S. led the 2015 Greenland field campaign. G.L.G., A.D.B., A.J.T., J.T., E.A.B., J.R.H., T.J.K., J.D.Z. and M.S. collected the sensor field data. G.L.G. and J.D.Z. collected manual water samples in the field. G.L.G. and A.M.A. analysed molecular data. G.L.G. performed the data analysis and wrote the manuscript with significant contribution from all co-authors.

Competing interests: P.F. works for the sensor manufacturer but the discussed sensor data was validated by independent measurements. The remaining authors declare no competing interests.

3. 2 Abstract

Ice sheets are currently ignored in global methane budgets (Kirschke et al., 2013; Schaefer et al., 2016). They have been proposed to cap large reserves of methane that may contribute to a rise in atmospheric methane concentrations if released during periods of rapid ice retreat (Wadham et al., 2008; Wadham et al., 2012), but no data on the current methane footprint of ice sheets currently exist. Here we find that subglacially-produced methane is rapidly flushed to the ice margin by the efficient drainage system of a subglacial catchment of the Greenland Ice Sheet. We report the continuous export of methane-supersaturated waters ($CH_{4(aq)}$) from the ice sheet bed during the melt season. Pulses of high $CH_{4(aq)}$ concentrations coincided with supraglacially-forced subglacial flushing events, confirming a subglacial source and highlighting the influence of melt on methane export. Sustained methane fluxes over the melt season were indicative of subglacial methane reserves in excess of export, with an estimated 6.3 (2.4 – 11) tonnes of $CH_{4(aq)}$ laterally transported from the ice sheet bed. Stable isotope analyses revealed a microbial origin for methane; most likely derived from a mixture of inorganic and ancient organic carbon buried beneath the ice. We show that subglacial hydrology is crucial for controlling methane fluxes from the ice sheet, with efficient drainage limiting the extent of methane oxidation (Dieser et al., 2014) to about 17% of methane exported. Atmospheric evasion is the main methane sink once runoff reaches the ice margin, with estimated diffusive fluxes (4.4 – 28 mmol-CH_4 m^{-2} d^{-1}) rivalling that of other world rivers (Stanley et al., 2016). Overall, our results provide evidence that ice sheets overlay extensive, biologically active methanogenic wetlands, and that high rates of methane export to the atmosphere can occur where efficient subglacial drainage pathways exist. Our findings suggest that such environments should be considered a previously underappreciated component of Earth's methane budget.

3.3 Article

The role of ice sheets in the global methane cycle depends on the ability (thermogenic or microbial) of subglacial environments to evolve large quantities of methane (e.g. as hydrates) (Weitemeyer and Buffett, 2006; Wadham et al., 2008; Wadham et al., 2012), as well as the mechanisms responsible for methane export to the ice margin and subsequent release to the atmosphere.

Subglacial CH_4-hydrates have been suggested to currently exist beneath the Antarctic Ice Sheet, large enough to raise atmospheric methane concentrations if released rapidly during deglaciation (Wadham et al., 2012). However, recent research has revealed the presence of active methane-oxidizing communities in subglacial ecosystems, suggesting the possibility of an efficient methane buffer by an active biological sink (Dieser et al., 2014; Michaud et al., 2017). There is also ambiguity in the paleo-record. New ice core data suggests that geological methane (e.g. from permafrost, but also potentially of ice sheet origin) had little role in affecting atmospheric methane concentrations over the Younger Dryas-Preboreal transition (Petrenko et al., 2017); but previous estimates do suggest large subglacial methane releases from retreating Paleo-ice sheets of the Northern Hemisphere following the onset of the last deglaciation (Portnov et al., 2016). Confounding scenarios on the potency of sub-ice-sheet methane mostly result from the scarcity of empirical data, limited to point measurements in ice cores (Souchez et al., 1995b; Miteva et al., 2009; Christner et al., 2012), Greenland marginal streams (Dieser et al., 2014), and an Antarctic subglacial lake (Michaud et al., 2017).

Here we provide direct evidence from the GrIS for the existence of large subglacial methane reserves, where production is not offset by local sinks and there is net export of methane to the atmosphere during the summer melt season. We focused on a 600 km^2 catchment of the GrIS which has been extensively studied over the last decade, both in terms of ice dynamics and subglacial geochemistry (section 3.7.1.1). Between 19 May and 13 July 2015, we deployed a CONTROS HydroC® CH_4 sensor (Schmidt et al., 2013) (Kongsberg Maritime Contros, Germany) < 2 km of the ice margin in the proglacial river of the Leverett Glacier (LG) (section 3.7.1.1; Extended Data Fig. 3.5) (Cowton et al., 2012; Kohler et al., 2017). Manual measurements supported sensor readings and CH_4 stable isotope analyses ($\delta^{13}C$ and δ^2H) and 16S rRNA gene sequence data from LG runoff were employed to infer methane origin. A one dimensional reaction-transport model was further applied to test for the possibility of hydrate formation beneath the ice in the catchment. Features of the study area suggest that results obtained are likely to be applicable to other ice-sheet catchments (section 3.7.1.1), and are informative on a global scale, serving as a first-step assessment of subglacial methane contribution to present-day methane budgets.

Sensor measurements revealed that LG runoff was supersaturated in methane with respect to the atmosphere over the entire monitoring period (mean concentration of ~271 nM, compared with an atmospheric equilibrium concentration of ~ 4.5 nM) (Fig. 3.1). This is consistent with the

high concentrations (up to ~24 μM) of methane detected in the basal regions of the GRIP, GISP2, and NGRIP ice cores (Souchez et al., 1995b; Miteva et al., 2009; Christner et al., 2012), in marginal runoff from a small neighbouring Greenland glacier (~3-83 μM) (Dieser et al., 2014) and during experimental incubations of Greenland subglacial sediment (Stibal et al., 2012b). Stepwise increases in methane concentrations closely followed the seasonal evolution of the subglacial drainage system, indicating the crucial role of hydrology in controlling methane export from the ice sheet. Clear differences in $CH_{4(aq)}$ concentrations were observed between a) the early part of the season during times of very low discharge when the subglacial portal was completely ice-sealed, and methane concentrations were low (mean ~64 nM) (Fig. 3.1, section 3.7.2.2), b) the emergence of a subglacial upwelling through the river ice in front of the LG on June 1, which released over-winter stored waters enriched in methane from the ice margin (mean ~4 μM prior to the melt season; see section 3.7.1.2, Extended data Fig. 3.1), and c) the later season (from June 19 onwards) with elevated $CH_{4(aq)}$ concentrations (pulses) coincident with a series of four subglacial outburst events (Supplementary section 3.7.2.2; Fig. 3.1). These outburst events were characterised by pulses in suspended sediment concentrations (SSC), electrical conductivity (EC), and pH (Fig. 3.1), indicative of subglacial origin as previously inferred (Bartholomew et al., 2011). The high concentrations of $CH_{4(aq)}$ observed during these events suggest the evacuation of methane-rich subglacial waters from progressively up-glacier sources (Supplementary section 3.7.2.2). We attribute the overall decreasing trend in methane concentration following the second outburst event to dilution by rising supraglacial icemelt inputs to the subglacial system over the melt-season. The sustained methane load observed during this period, however, indicates that subglacial methane reserves are not exhausted despite increases in meltwater discharge (Fig. 3.1).

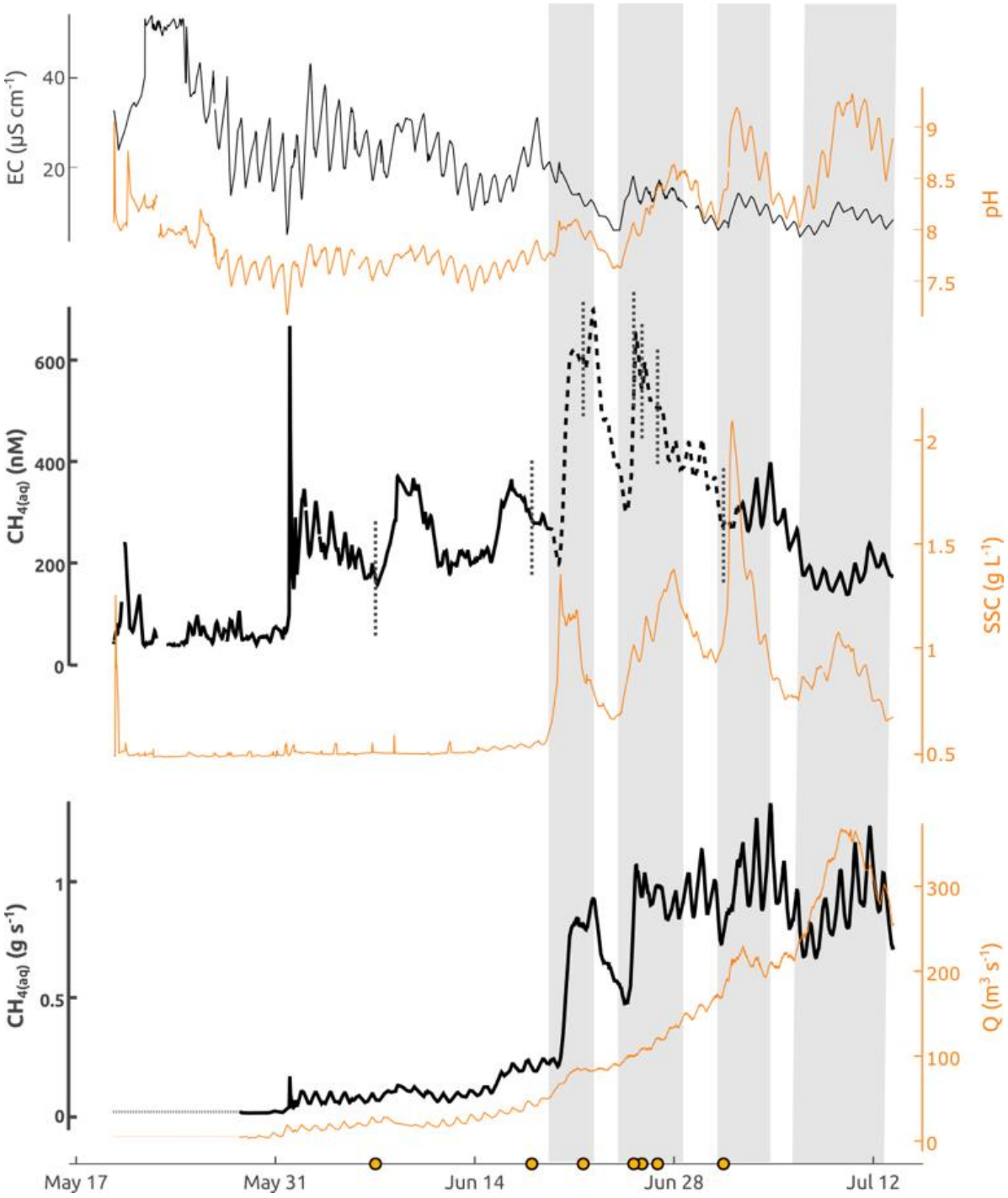

Figure. 3.1 Geochemical time series of the LG proglacial river – Top: Electrical-conductivity (EC) and pH. Middle: $CH_{4(aq)}$ (HydroC®) and suspended sediment concentrations (SSC); the dashed section corresponds to times when the HydroC® sensor experienced slower response times (see Supplementary section 3.7.2.1, Extended Data Fig. 3.6). Orange dots and vertical dashed lines indicate sampling time of waters used for stable isotope analysis (see Extended Data Table 3.2). Bottom: $CH_{4(aq)}$ lateral flux and discharge (Q); the first data points on May 28 are extended to the first data point of the above sensor measurements (dashed horizontal lines). Abrupt increases in SSC, EC, pH, and $CH_{4(aq)}$ correspond to outburst events (shaded sections) and reflect sudden drainage of sub-ice sheet waters and sediments driven by supraglacial melt water entering the subglacial system (Supplementary section 3.7.2.2). Y axes corresponding to black and orange datasets are located on the left and right, respectively.

The cumulative lateral flux of $CH_{4(aq)}$ from LG amounted to ~1.87 (1.64 – 2.10) tonnes (t) over the measurement period. However, we estimate that at least 2.78 (2.43 – 3.12), but more likely ~6.28 (5.19 – 7.36) t of $CH_{4(aq)}$, were laterally transported at the measuring site over the entire 2015 melt season (Fig. 2, see methods for details). Methane measurements provide conservative estimates of total methane production across the glacier, since recorded concentrations would have been influenced by oxidative and diffusive processes upstream of the measuring site, and hence subglacial methane production beneath the catchment are likely larger. Based on previously measured microbial oxidation rates (Dieser et al., 2014), we estimate that the bacterial methane sink at LG to have amounted to ~ 1.22 t prior to subglacial discharge reaching the ice margin, or about 16% of total methane export at the measuring site over the melt season, based on a sustained flux scenario (Fig. 3.2; Supplementary section 3.7.2.3).

We employ scaling relationships between gas transfer velocities and river hydrology (Raymond et al., 2013) to derive conservative approximations of diffusive fluxes of methane from the LG proglacial river. We infer that there will be some evasion of methane from subglacial runoff to air spaces in subglacial channels close to the margin (Chandler et al., 2013) and to the atmosphere after emergence at the glacier subglacial portal. We estimate that such atmospheric evasion constitutes the main sink of $CH_{4(aq)}$ when compared to microbial oxidation, with diffusive fluxes responsible for at least 1.72 (0.51 – 3.19) t of CH_4 released to the atmosphere between the ice margin and the measuring site (Fig. 2; compared to ~ 0.09 t of CH_4 oxidised for the same distance, or ~ 1% of exports, data not shown). Recent work on white-water streams have indicated that these traditionally used scaling relationships can grossly underestimate (by several orders of magnitude) diffusive fluxes in white-water systems (Hall et al., 2012; Maurice et al., 2017). Considering the high degree of turbulence observed on the LG river (Extended Data Fig. 3.5), we therefore stress that our estimates here constitute lower limit values. What is clear is that the LG catchment is a source of atmospheric methane, with our minimum estimates indicating that over 18% (7.5 – 26%) of exported methane reaches the atmosphere within 2 km of the ice sheet margin.

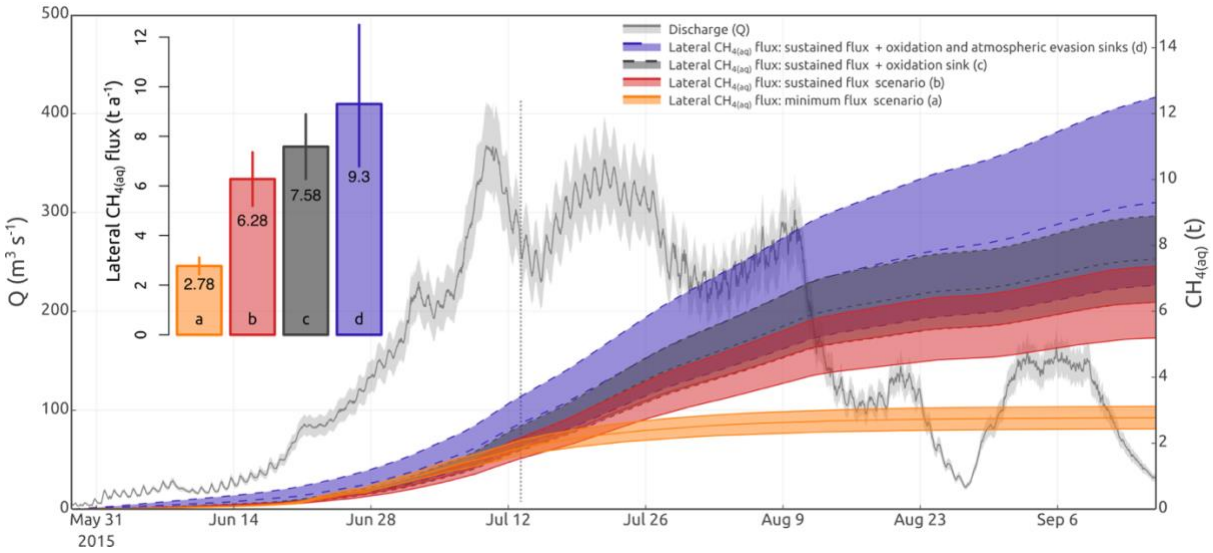

Figure 3.2 Cumulative lateral export of LG $CH_{4(aq)}$ over the 2015 melt season – Orange and red lines correspond to minimum and sustained methane flux scenarios respectively at the measuring site (see methods). Dark grey lines account for a methanotrophic methane sink on a sustained flux scenario and represent the expected lateral methane flux that would have occurred without a methanotrophic sink. Blue lines account for the combined estimated methanotrophic and diffusive flux sinks of methane prior to reaching the measuring site, added to a sustained flux scenario. The annual methane fluxes depicted on the bar plot correspond to the cumulative fluxes at the end of the melt season for each of the estimated scenarios. The vertical line marks the last day of CH_4-sensor measurements (July 13). Width of shaded areas corresponds to errors from sensor measurements and estimates of gas transfer velocities (see methods). The pale grey time series corresponds to discharge measurements over the entire melt season.

Methane concentrations at LG fell within the global range reported for streams and rivers (Fig. 3.3). A recent survey of riverine methane indeed revealed that streams have previously been overlooked as net contributors of atmospheric methane, estimated to emit over 27 Tg of CH_4 annually, or ~ 15-40% of global wetland and lake effluxes respectively (Stanley et al., 2016). Results presented here suggest that streams draining subglacial basins are probably no exception, with the estimated diffusive fluxes of methane at LG falling in the higher range of reported world averages for rivers, comparable to the large fluxes observed in the Congo basin (Fig. 3.3; Extended data Table 3.1). Because of the high uncertainties surrounding LG methane diffusive fluxes, it is difficult to accurately determine the overall contribution of methane to the atmosphere from the LG catchment, and by extension from the GrIS margin as a whole.

In order to more directly compare methane fluxes at LG with other systems, we calculated a catchment-wide areal yield of $CH_{4(aq)}$ that contributed to the observed $CH_{4(aq)}$ lateral flux. When comparing catchment area-normalised yields of $CH_{4(aq)}$, the lateral $CH_{4(aq)}$ flux from LG translates into a yield significantly higher than, or within the range, of other large rivers worldwide, and highlight that the GrIS may act as a relatively important source of atmospheric methane (Extended Data Table 3.1, Supplementary 3.7.1.3). Ultimately, the atmospheric footprint of GrIS CH_4 will partly depend on the overall surface area of the ice sheet contributing to the overall diffusive fluxes, as well as the magnitude of such fluxes at points of first contact between the atmosphere and subglacial runoff (e.g. within open channels beneath the ice).

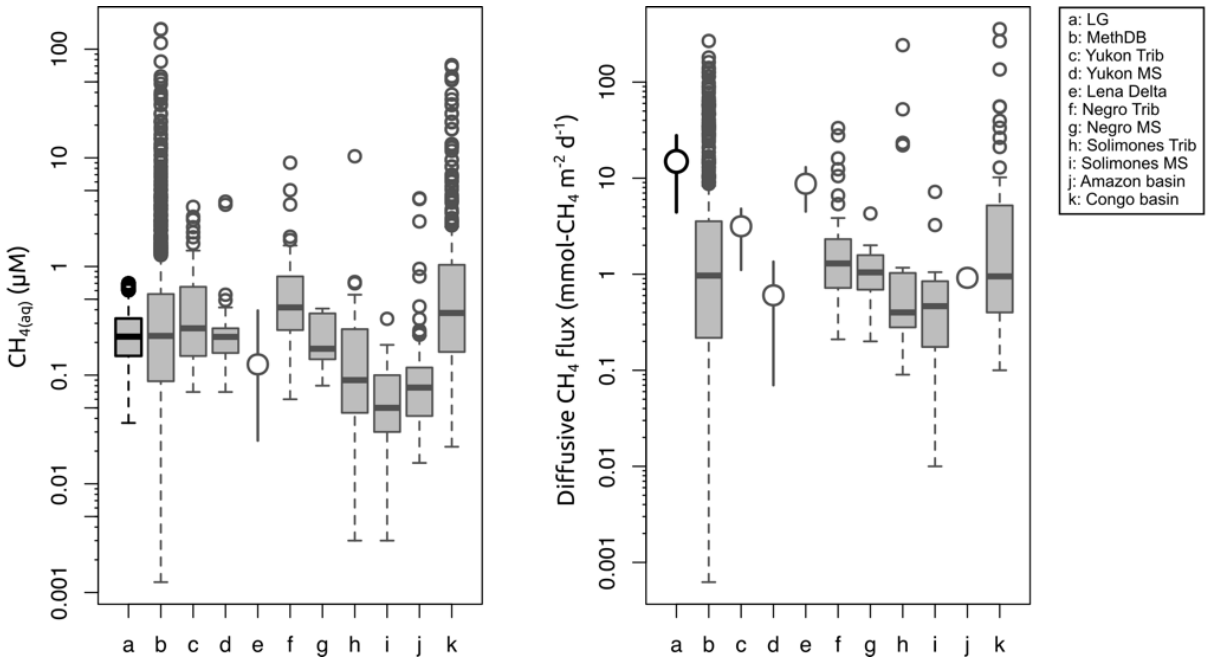

Fig. 3.3 Box plots of $CH_{4(aq)}$ concentrations and diffusive fluxes for the LG and other major world river systems – Box mid lines represent medians; the interquartile range (IQR) is represented by the lower and upper box boundaries and denote the 25th and 75th percentiles, respectively; whiskers indicate 1.5 times IQR confidence intervals and points are outliers. Where no raw data was available, averages and reported ranges are depicted by circles and error bars (see Supplementary section 3.7.1.3 for details). MethDB refers to a worldwide $CH_{4(aq)}$ dataset for rivers (Stanley et al., 2016). "Trib" and "MS" refer to rivers' tributaries and mainstems, respectively.

Stable isotope analyses ($\delta^{13}C$ and $\delta^{2}H$) revealed that LG methane was microbial in origin, with most samples falling in a well-defined range characteristic of acetoclastic methanogenesis, although with some degree of mixing with methane likely produced by a CO_2-reduction pathway (Fig. 3.4). This mixed origin of methane by CO_2-reduction and acetate fermentation is also supported by molecular evidence from the LG proglacial stream, which identified the presence of 16S rRNA gene sequences related to both hydrogenotrophic and acetoclastic methanogens (Extended Data Fig. 3.8; Supplementary section 3.7.2.4). A mixed methane source at LG suggests the availability of several methanogenic substrates beneath the ice, likely derived from the recycling of overridden old carbon (e.g. acetate), such as seen in GrIS marginal lakes (Walter Anthony et al., 2012), potentially supplemented by H_2 gas generated from rock comminution hypothesised to fuel methanogens beneath ice masses over extended glaciation (Telling et al., 2015) (see Supplementary 3.7.2.4).

Partial oxidation during transit from the subglacial system likely enriched the sampled methane with heavier stable isotopes (Whiticar, 1999) (Supplementary section 3.7.2.3), yet there is no strong isotopic trend that conclusively identifies methanotrophy as a major control on the isotopic signatures observed here (Fig. 3.4; Extended Data Fig. 3.7). This contrasts with patterns we observed for stagnant waters beneath the LG proglacial river-ice (this study, Extended Data Fig. 3.7) and waters sampled from Antarctic Subglacial Lake Whillans (Supplementary section 3.7.2.3). We infer the limited methanotrophic signature here to reflect the largely anoxic conditions at the sites of methane production (and thus limited aerobic oxidation of methane) and the rapid evacuation of methane from the production site via a fast and efficient drainage system (Supplementary section 3.7.2.2).

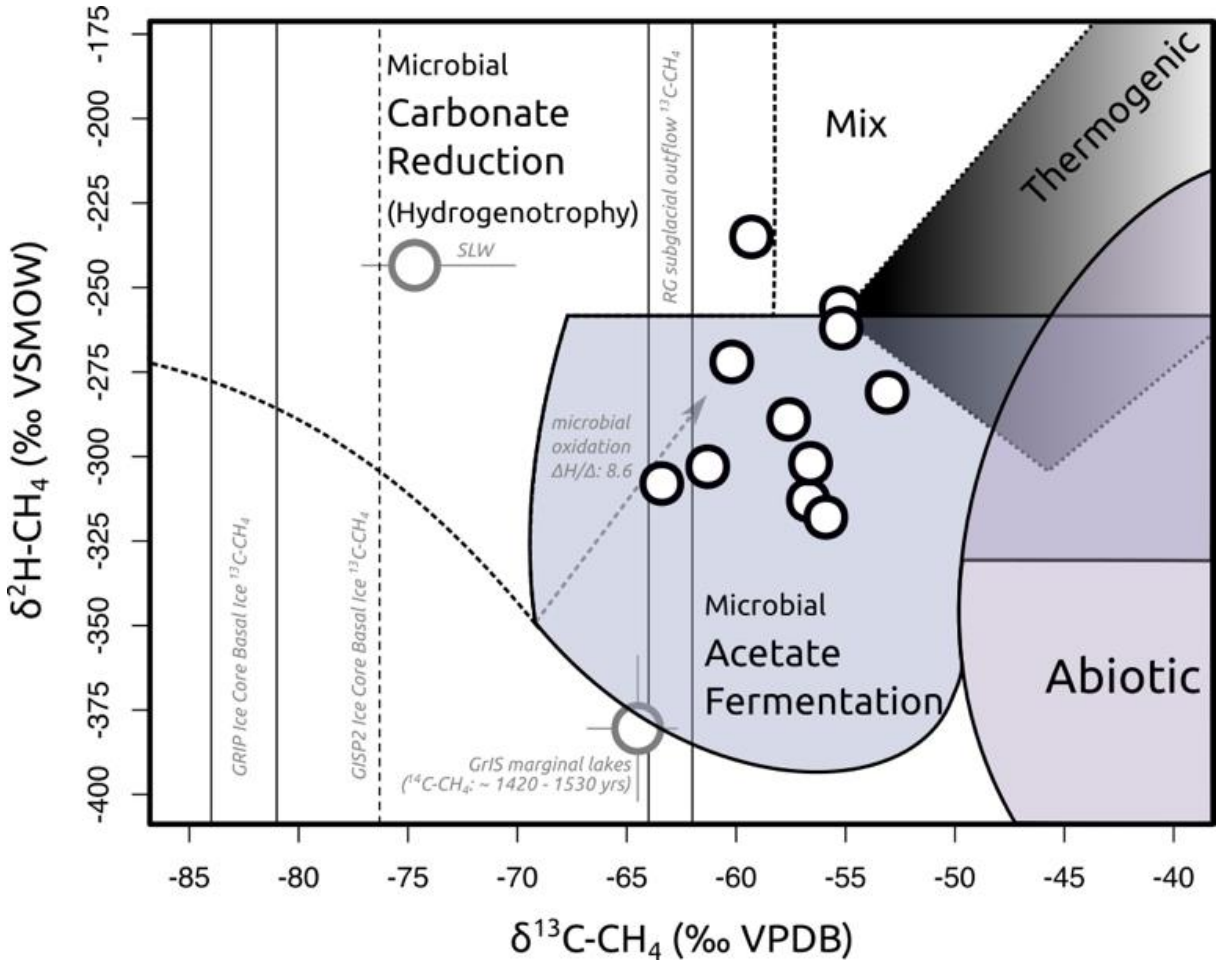

Fig. 3.4 **Carbon-Hydrogen isotopic diagram of LG $CH_{4(aq)}$** – Black points denote dual stable isotopic values ($\delta^{13}C$ and $\delta^{2}H$) for LG $CH_{4(aq)}$ samples (sample values are summarised in Extended Data Table 2). Average $\delta^{13}C$- and $\delta^{2}H$-CH_4 values and ranges from Subglacial Lake Whillans (SLW) in Antarctica (Michaud et al., 2017) and GrIS marginal lakes (Walter Anthony et al., 2012) are added as references (grey points), as well as $\delta^{13}C$-CH_4 data from GrIS ice core basal ice (Souchez et al., 2006; Miteva et al., 2009) and from the subglacial outflows of the Greenland Russell Glacier (RG) (Dieser et al., 2014) (marked by vertical lines). Arrow denotes microbial oxidation effect on CH_4 stable isotope signatures; classification zones and definitions of methane origins are derived and adapted from (Whiticar, 1999; Etiope and Sherwood Lollar, 2013).

The impact of subglacial methane on atmospheric concentrations partially depends on the presence of methane hydrates beneath ice sheets, as catastrophic CH_4-hydrate destabilization during periods of rapid ice thinning could likely result in very large fluxes of methane to the atmosphere (Wadham et al., 2008; Wadham et al., 2012). We employed a 1D reaction-transport model to identify the conditions required to allow for CH_4-hydrate formation beneath the LG catchment. Our results indicate that relatively high methanogenic rates (larger than observed in Greenland basal ice incubation experiments (Stibal et al., 2012b); Extended Data Fig. 3.9) and thick sediment layers (at least several tens of meters) are required to evolve and sustain methane hydrates beneath the LG catchment (Supplementary section 3.7.2.5-6). The high methane flux that would be generated at the ice-sediment interface under CH_4-hydrate conditions (estimated at 10 to 1,000 times larger than the observed lateral flux depending on hydrate conditions; Extended Data Fig. 3.10) makes it unlikely that a significant portion (if any) of the exported CH_4 measured from the LG comes from subglacial CH_4-hydrates. Importantly, however, the model results suggest that conditions favourable to hydrate formation are likely present in other regions of the GrIS, where there has been sustained thick ice cover (e.g. for > 10,000 years), and where thick sedimentary layers exist (e.g. Walter et al. (2014); Supplementary section 3.7.2.6).

Using high-resolution *in situ* sensor measurements, we show that an extensive area of the GrIS continuously releases methane-supersaturated runoff from its bed during the melt season. Our results constitute the first measurements of sustained methane export from an ice sheet catchment, and highlight the need to better gauge the footprint of ice sheets on current methane budgets. The release of several tonnes of microbial methane from beneath the GrIS represents one of the strongest lines of evidence to date for significant microbial production of methane in subglacial ecosystems, and reinforces the view that large methane reserves may accumulate beneath past and present day ice sheets (Weitemeyer and Buffett, 2006; Wadham et al., 2008). This methane can reach the atmosphere where fast-flowing drainage networks enable its rapid transport beyond the ice margin prior to being oxidised to carbon dioxide, whether driven by supraglacial forcing in the GrIS ablation zone, or potentially also during episodic subglacial lake drainage events in Antarctica (Wingham et al., 2006). The influence of meltwater discharge on methane export observed here further suggests that projected increases in warming and melting rates could also lead to increases in subglacial methane release to the atmosphere. Our findings that subglacial environments in Greenland can generate high levels of methane emphasise the

need to directly measure methane reserves in subglacial systems containing high quantities of organic carbon, such as the thick sedimentary basins beneath the Antarctic Ice Sheet, where much larger amounts of methane, as hydrates, are expected to be present (Wadham et al., 2012).

Acknowledgments

We thank all of those who assisted with fieldwork at LG, especially Jade Hatton, as well as Dr Fotis Sgouridis and Mr James Williams in LOWTEX laboratories at the University of Bristol. This research is part of the UK NERC funded DELVE programme (NERC grant NE/I008845/1) to J.L. Wadham and G. Lamarche-Gagnon was funded via the University of Bristol Scholarship Program and FRQNT Scholarship (scholarship ID 185136) for his PhD. The work was also supported via Leverhulme Trust, via a Leverhulme research fellowship to JLW, a UK NERC grant (NE/J02399X/1) to A.M. Anesio for DNA analyses, as well as Czech Science Foundation grants (GACR; 15-17346Y and 18-12630S) to M. Stibal. Isotopic analyses were conducted by Dr. Georges Lacrampe-Couloume at the University of Toronto with support provided by the Natural Sciences and Engineering Research Council of Canada (NSERC) to B.S.L. We also thank the Kangerlussuaq International Science Station, especially Rikka Møller, for support with field logistics, as well as Michael A. Cooper, Moya Macdonald, and Stefan Hofer for comments.

Data availability

The data used in this article are available from the corresponding author (guillaume.lg@bristol.ac.uk) on request. The 16S rRNA gene sequence data are available in the NCBI Sequence Read Archive (https://www.ncbi.nlm.nih.gov/sra) under BioProject PRJNA495593 (BioSamples SAMN10228172-SAMN10228185; SAMN10228190-SAMN10228206).

3.4 METHODS

3.4.1 Site description and hydrogeochemical analyses

The hydrology of LG has been extensively studied and described previously (see Supplementary Information 3.7.1.1). A detailed description of the proglacial study site, as well as the hydrological and geochemical monitoring performed during the 2015 melt season can be found in two parallel studies (Beaton et al., 2017; Kohler et al., 2017). Briefly, a suite of hydrogeochemical sensors

[logging for pH, (Honeywell Durafet), water temperature (Aanderaa and Campbell Scientific), electrical conductivity (Campbell Scientific 547), and turbidity (Partech C)] were deployed in the LG proglacial river ~ 1.6 km downstream from the subglacial ice portal at the glacier's terminus (Extended Data Fig. 3.5). Turbidity measurements were converted to suspended sediment concentrations by calibration against manual sediment samples collected over the span of the melting season as per Hawkings et al. (2014). Discharge measurements were derived from pressure transducers (Druck and Hobo) and stage sensors (Campbell Scientific SR50A) fixed in a bedrock section ~ 2 km downstream from the glacier's terminus. Stage measurements were converted to discharge using a stage-discharge rating curve generated from calibration against repeat Rhodamine dye injections over the full range of river stages during the melt season as per Bartholomew et al. (2011). Uncertainties (RMSD) on discharge measurements were calculated to be ~ 12.1%.

3.4.2 Manual sampling

Manual samples were collected a few meters (~ 5-10 m) upstream of the HydroC®. Water samples were collected inside pre-evacuated (at most 500 mTorr) 120 mL borosilicate vials sealed with 2 cm thick butyl-rubber stoppers, pre-flushed with 5.0 grade argon, and pre-poisoned with ~24 mg of $HgCl_2$ to fix the samples and prevent any microbial activity affecting the gases post-sampling; after the method of Ward et al. (2004). 10 mL (at room temperature and pressure) of helium (grade 5.0) was added to the evacuated vials to maintain a headspace during sampling. Most water samples (n=53) were collected using a peristaltic pump (Portapump-810, Williamson Manufacturing) equipped with silicone tubing; a small number of samples were collected using plastic syringes (n=2) or passively using the vials' vacuum pressure by directly piercing the septum of submerged vials with a needle (n=8). Vials containing apparent air contamination or vacuum loss (e.g. resulting in abnormally large headspace post sampling) were excluded from analyses. Samples for stable isotopic analysis were collected as above (n=9 collected using the peristaltic pump, n=2 using syringes).

Methane concentrations were calculated using the headspace method. Headspace samples were analysed on an Agilent 7980A gas chromatograph equipped with a Porapak Q 80-100 mesh, 2.5 m X 2.0 mm SS column and flame ionization detector. Standard curves were calculated from certified (± 5%) gas standard measurements. Gas concentrations were converted to molar concentrations using the ideal gas law and dissolved methane concentrations were obtained using

Bunsen coefficients (Wiesenburg and Guinasso Jr, 1979). Internal vial pressures were calculated using the ideal gas law from the difference between the headspace volume post-sampling and the theoretical headspace volume of 10 mL at 1 atm and 20°C. The average internal pressure of 3.5 (± 0.9 standard deviation) atm was assigned to all manual samples for calculations.

3.4.3 CONTROS HydroC® CH4 sensor

Methane measurements were performed using a CONTROS HydroC® CH_4 system (Kongsberg Maritime), an optical (infrared), headspace-based underwater sensor. An underwater pump (SBE 5T, Sea-Bird Scientific) mounted to the sensor continuously feeds water to the membrane equilibrator. Dissolved gases diffuse through a composite membrane into the internal gas circuit where partial-pressure is measured via tunable diode laser absorption technology; concentrations (i.e. partial-pressures) are derived from laser light intensities converted from firmware-stored calibration coefficients (Schmidt et al., 2013). The CONTROS HydroC® sensor was deployed completely submerged within a solid metallic cage moored by cables attached to boulders on the river bank, with the sensor head facing the river current (Extended Data Fig. 3.5). Measurements were logged every minute between May 19 and June 4; the logging interval was changed to 5 minutes on June 4 until the end of the measuring period on July 13.

The ideal gas law and Bunsen coefficients were used to convert µatm measurements (Extended Data Fig. 3.11c) to molar concentrations (Fig. 3.1). Water temperatures ±0.05°C were recorded using an Aanderaa Optode 3830 sensor deployed in parallel (Extended Data Fig. 3.11a). The CONTROS HydroC® CH_4 reported overall uncertainty is 2 µatm (~ 5nM) or ±3% of reading, whichever is greater. The HydroC® had been factory calibrated a few months prior to deployment. Factory calibration procedures, linearity of measurements, and detection limits are described in Schmidt et al. (2013). Briefly, the sensor is calibrated within a semi closed, insulated and temperature controlled water tank, preventing gas exchange with the atmosphere. The tank water is continuously equilibrated with standard gas mixtures and the linearity of the sensor to dissolved gas concentrations recorded (see Fig. 4 in Schmidt et al. (2013); the calibration tank is described in Fietzek et al. (2013), although with the pCO2 version of the CONTROS HydroC®). Dissolved methane concentrations within the calibration tank is further verified by parallel measurements using the headspace method and gas chromatography (Schmidt et al., 2013). Here, methane concentrations obtained from sensor measurements were compared to manual samples in order to validate precision and accuracy of the measurements over the range of the

deployment season and recorded concentrations (see Extended Data Fig. 3.6 and supplementary discussion; section 3.7.2.1).

3.4.4 Calculation of lateral methane flux

$CH_{4(aq)}$ measurements stopped on July 13. $CH_{4(aq)}$ fluxes estimated during the rest of the ablation season were based on two scenarios: i) assuming that methane levels would immediately decrease until reaching river baseline concentrations on September 15 (last discharge measurement), or alternatively, ii) continue to follow a discharge-dependent trend for the duration of the ablation season.

3.4.4.1 Constant concentration-decrease scenario (annual lateral flux of 2.78 t-CH_4)

In the constant concentration-decrease scenario, a baseline $CH_{4(aq)}$ concentration was set based on manual water samples collected during a return visit to the sampling site on October 28, at a time during which the proglacial river was partially frozen, and where no runoff contribution to the proglacial river stream was apparent. October concentrations averaged ~18.5 nM (beneath river ice at that time, n=6).

The minimum flux scenario was calculated using a natural log decrease behaviour of the form:

$$y=C\,e^{-(kt)}$$

where y is the methane flux (e.g. in g s^{-1}), C is the last flux measurement on July 13 (i.e. 0.71 g s^{-1}), t is the time elapsed between July 13 and the flux y, and k is the reaction constant obtained assuming a baseline concentration of 18.5 nM and using the discharge of 32 m^3 s^{-1} (last discharge measurement) on September 15.

3.4..4.2 Sustained-flux scenario (annual lateral flux of 6.28 t-CH_4)

The sustained-flux scenario was calculated using the discharge-weighted mean $CH_{4(aq)}$ concentration of 271 (± 34) nM obtained from measurements up to July 13; the error reflects errors on discharge measurements (12.1%) as well as the HydroC®-CH_4 measurement errors (2 µatm or %, whichever is greater).

3.4.5 Estimation of methane sink via methanotrophic oxidation

The recorded methane concentrations at LG most likely underestimated the original methane levels present beneath the catchment because of the water travel time between the subglacial methane source and the measurement site. In addition to atmospheric evasion of methane, aerobic microbial oxidation of methane would have lowered methane concentrations prior to reaching the observation site once fully oxygenated meltwater runoff entered the subglacial system (O_2 concentrations in runoff were either in near atmospheric equilibrium or supersaturated for most of the monitoring period; Extended Data Fig. 3.11a). Methanotrophy was observed qualitatively in a small number of un-fixed river samples collected in parallel to fixed manual samples, with up to a 100 fold decrease in $CH_{4(aq)}$ concentrations in unfixed versus fixed vials upon analyses back in the home laboratory (data not shown). However, no time series incubation was set-up and consequently no methanogenic rates were calculated for the LG site.

The quantity of methane oxidized by methanotrophic bacteria prior to reaching the measuring site was estimated using the methanotrophic rate reported for the marginal stream of the neighbouring Russell Glacier (i.e. 0.32 μM d^{-1}) (Dieser et al., 2014). Justifications for using the Russell Glacier oxidation rate are discussed in Supplementary section 3.7.2.3. The time during which runoff was subject to methane oxidation (i.e. water travel-time) was estimated from water velocities and subglacial drainage evolution calculated based on a previous study at LG by Chandler et al. (2013). We assumed that subglacial aerobic methane oxidation occurs between the location of supraglacial runoff-input, where oxygenated supraglacial waters enter the subglacial system, and the measuring site located 1.6 km downstream of the LG glacier terminus.

Water velocities were estimated using the relationship between maximum tracer velocity (v0.5) and cumulative discharge ($\sum Q$) described for the gaseous SF6 tracer in ref. (Chandler et al., 2013), which takes the form:

$$v0.5 = A * \ln(\sum Q) + B$$

with regression parameters A and B calculated to be 0.235 m s^{-1} and -3.59 m s^{-1} respectively (Chandler et al., 2013). We fixed a minimum velocity of 0.4 m s^{-1}, which corresponds to the minimum v0.5 calculated for tracer injections performed 7 km inland from the LG portal at times of low cumulative discharge by Chandler et al. (2013).

We estimate the inland evolution of an efficient channelized subglacial hydrological system based on the relationship between cumulative discharge and v0.5 at moulin injection sites (see Fig. 2.a in Chandler et al. (2013)). We derived the progression of supraglacial water-inputs using the lowest value of cumulative discharge observed where v0.5 at an injection site fell onto the regression line of v0.5 to cumulative discharge for the L7 injection in Chandler et al. (2013) (see Figure S2.8 in Chandler et al. (2013)). That is, we fixed that the channelized subglacial channel would reach 7 km at a cumulative discharge of 1.9 x 10^7 m^3, 14 km at a cumulative discharge of 9.4 x 10^7 m^3 and 41 km at 7.8 x 10^8 m^3 based on figure S2.8 and Table S1 in Chandler et al. (2013). We acknowledge that such calculations are approximate at best, but they allow the use of a dynamic distance of travel during the melt season. We fixed a maximum travel distance of 41 km from the LG terminus, after which the LG subglacial system is considered to become primarily inefficient and distributed for the duration of the ablation season (Chandler et al., 2013). To account for potential methane sources and methanotrophic activity occurring downstream of the supraglacial-runoff input into the subglacial channelized-system, we used an average distance of travel in our calculation (i.e. half of the distance of travel obtained from cumulative-discharge calculations above).

3.4.6 Calculation of diffusive methane flux

Accurately calculating methane losses due to atmospheric evasion was beyond the scope of the present study, and therefore, flux numbers should be considered conservative estimates of the amount of methane originally generated and exported from the LG catchment.

Diffusive fluxes for the LG stream were estimated following the approach by Raymond et al. (2013), which estimates gas transfer velocity coefficients (*k*) from stream slope and water velocity (fitted equation 5 in Raymond et al. (2012)). Fluxes were estimated for the first 1.6 km of the proglacial river, from the ice margin to the measuring site. Stream slope was obtained via Google Earth and approximated 0.04; a slope value of 0.01, 0.03, and 0.05 was used to generate minimum, medium, and maximum *k* values. A water velocity of 1 m s^{-1} was used which corresponds to the discharge weighted mean of subglacial water velocities (v.05) used for methanotrophic sink calculations (see above).

Methane gas transfer velocities (k_{CH4}) were converted from the calculated k_{600} values following relationships between Schmidt numbers and k for CO_2 and CH_4 (see equations 2 and 3 in Raymond et al. (2012)); Schmidt numbers were calculated using an average water temperature value of 0.22°C (Extended Data Fig. 3.11d) (Wanninkhof, 2014). Minimum, medium, and maximum slope values, as we well as standard deviations on k_{600} equation parameters (Raymond et al., 2012) resulted in minimum, medium, and maximum k_{CH4} of 16, 49, and 84 m d^{-1} respectively.

Methane diffusive fluxes were calculated using the discharge-weighted mean $CH_{4(aq)}$ concentration for the observation period (271 nM) and assuming an atmospheric methane concentration of 1.8 ppmv (resulting in an equilibrium concentration of about 4.6 nM). Diffusive flux occurring upstream of the measuring site was calculated using 1 m retroactive bins, adjusting upstream dissolved methane concentrations for methane loss by both diffusive flux and microbial oxidation losses in downstream bins; a fixed river width of 40 m, water velocity of 1 m s^{-1}, and average discharge of 150 m^3s^{-1} were used in calculations. The reported diffusive flux values correspond to the average flux calculated for the 1.6 km of stream for each minimum, medium, and maximum scenarios. Cumulative fluxes were calculated for the discharge-measurement period (i.e. ~ 110.5 days) and normalized to estimated water velocities (see above section). Details on the diffusive fluxes of other world rivers can be found in Supplementary section 3.7.1.3.

3.4.7 Stable Isotope Analyses

Analyses for $\delta^{13}C$ values were performed by continuous flow compound specific carbon isotope ratio mass spectrometry with a Finnigan MAT 252 mass spectrometer interfaced with a Varian 3400 capillary GC. Hydrocarbons were separated by a Poraplot Q™ column (25m x 0.32mm ID) with temperature program: initial 40°C hold 1 minute, increase to 190°C at 5°C/min., hold 5 minutes. Total error incorporating both accuracy and reproducibility is ± 0.5‰ with respect to V-PDB standard (Sherwood Lollar et al., 2007). The δ^2H analysis was performed on a continuous flow compound specific hydrogen isotope mass spectrometer which consists of an HP 6890 gas chromatograph (GC) interfaced with a micropyrolysis furnace (1465°C) in line with a Finnigan MAT Delta$^+$-XL isotope ratio mass spectrometer. H_2 and CH_4 were seprated by a Molecular Sieve 5A column (25m x 0.32 mm ID) with a carrier gas flow rate of 1.2 mL/min with the temperature program: initial 20°C, hold minutes followed by an increase to 280°C at 25°C/min. Higher hydrocarbons were separated using the same column and temperature

program as the carbon isotope analysis. Total error incorporating both accuracy and reproducibility for hydrogen isotope analysis is ± 5 ‰ with respect to V-SMOW (Ward et al., 2004).

3.4.8 CH_4-Hydrates

In order to evaluate the potential for hydrate formation beneath the LG catchment, we employed a one-dimensional reaction-transport model that has been originally developed for simulating hydrate formation in marine sediments (Davie and Buffett, 2001) and has previously been adapted for subglacial Antarctica (Wadham et al., 2012). We assumed physical properties for sediments similar to those previously employed for ocean sediment modelling (Davie and Buffett, 2001). Extended Data Table 3.3 summarizes site-specific model parameters, their model values and units. The model solves the one-dimensional diffusion-advection-reaction equations for dissolved methane, gaseous methane and methane hydrates. The implemented reaction network accounts for a constant methane production rate R_m over a predefined sediment depth z_m, methane hydrate, as well as methane gas formation and dissociation. At the upper boundary, the boundary concentrations are set to zero (i.e. Dirichlet boundary condition) reflecting warm-based conditions and allowing for diffusive flux of methane through the ice-sediment interface. In addition, initial conditions for dissolved and gaseous methane, as well as methane hydrates were set to zero. A "best case" scenario was designed to reflect optimal, but plausible physical and biogeochemical conditions for hydrate formation to assess the maximum potential for hydrate accumulation in the catchment. More specifically, we assigned a thick methanogenic sediment layer beneath the catchment (i.e. up to 100 metres), a 10,000 year ice sheet overburden to allow for hydrate evolution, complete anoxic conditions, an overlaying ice thickness set to 1,000 metres (ice thickness over the LG catchment exceeds 1,000 metres at ~ 39 km from the ice margin (Chandler et al., 2013)), a basal temperature of -1°C, and assumed the absence of a methane sink within the sediment layer (e.g. no anaerobic oxidation of methane). This "best case" model set-up was run over a wide range of constant methane production rates (Rxn= 10^{-17} to 10^{-13} g-CH_4 g^{-1} wet sediment s^{-1}) to determine the order of magnitude of methane production rates required to accumulate hydrates. After this initial screening, methane production rates were varied systematically between Rxn= 10^{-15} to 10^{-14} g-CH_4 g^{-1} wet sediment s^{-1}.

3.5 Extended Data Tables and Figures

Extended Data Table 3.1 | $CH_{4(aq)}$ concentration, fluxes, and areal yield from LG, the GrIS, and other world rivers*

River	Catchment Area (10^6 km^2)	Discharge (km^3 a^{-1})	Concentration (µM $CH_{4(aq)}$)	Diffusive flux (mmol-CH_4 m^{-2} d^{-1})	Diffusive flux (Gg-CH_4 a^{-1})	Lateral flux (Gg-$CH_{4(aq)}$ a^{-1})	Areal Yield Diffusive (mmol-CH_4 m^{-2} a^{-1})	Areal Yield Lateral (mmol-$CH_{4(aq)}$ m^{-2} a^{-1})
LG runoff	**0.0006**	**1.45**	**0.27**	**14.94**	**-**	**0.0063**	**-**	**0.65**
GrIS runoffs†	-	*418*‡	*0.27*	-	-	*2.1*	-	-
Lena Delta	2.49	821	0.07	9.22	150	0.9	3.8	0.02
Yukon Trib	0.19	48	0.75	3.16	12	0.6	4.0	0.19
Yukon MS	0.82	206	0.38	0.60	8	1.3	0.6	0.10
Negro Trib	0.69	455	0.87	-	-	6.0	-	1.29
Negro MS	0.69	1634	0.26	2.00	79	4.2	7.2	0.38
Solimões Trib	0.99	1985	0.33	-	-	10.6	-	1.17
Solimões MS	0.99	3507	0.06	1.60	160	3.3	10.1	0.21
Amazon	6.03	5444	0.18	0.92	490	15.5	5.1	0.16
Congo	3.71	1270	3.17	16.42	1906	64.6	32.1	1.10

*Diffusive fluxes are calculated grand means except for the LG runoff diffusive flux which corresponds to the medium flux scenario (data point Fig. 3.3; see methods for details). Except for the Amazon and Congo, lateral fluxes and yields are calculated using discharge-weighted means; see Supplementary section 3.7.1.3 for reference and calculation details.

†GrIS-wide $CH_{4(aq)}$ flux was estimated using the LG discharge-weighted $CH_{4(aq)}$ concentration mean applied to the entire GrIS runoffs; this number is therefore speculative and was included as reference only.

‡From Tedesco et al. (2013)

Areal yields are for entire catchment areas whereas diffusive fluxes refers to stream surface areas.

Extended Data Table 3.2 | Stable isotope details of CH_4 and CO_2

Sampling Time	$\delta^{13}C$-CH_4 (‰ VPDB)	$\delta^{2}H$-CH_4 (‰ VSMOW)	$\delta^{13}C$-CO_2 (‰ VPDB)
2015-05-04 12:00	-48.9	-	-16.9
2015-05-04 12:00	-46.1	-	-18.4
2015-05-30 11:30	-6.1	-	-12.2
2015-06-07 12:00	-61.3	-303	-15.3
2015-06-07 12:00	-53.1	-281	-16.0
2015-06-17 23:00	-56.7	-313	-15.8
2015-06-17 23:00	-55.2	-256	-14.5
2015-06-21 16:15	-59.3	-235	-22.2
2015-06-21 16:15	-57.6	-289	-24.1
2015-06-25 15:40	-63.4	-308	-14.6
2015-06-25 05:20	-56.6	-302	-14.8
2015-06-26 18:15	-60.2	-272	-23.6
2015-07-01 09:55	-55.9	-318	-26.8
2015-07-01 09:30	-55.2	-262	-26.2

First three rows correspond to borehole and chainsawed-hole collected samples (see Supplementary section 3.7.1.2; Extended Data Fig. 3.7).

Extended Data Table 3.3 | Site specific parameters applied in the 1D hydrate model

Symbol	Parameter	Value	Unit
z_{xn}	Sediment thickness	20-100	m
h	Ice thickness	1,000	m
G	Geothermal gradient	0.025	°C m^{-1}
T(0)	Basal Temperature	-1	°C
sed	Sedimentation rate	0	m s^{-1}
vup	Upward fluid flux	0	m s^{-1}
φ0	Porosity	0.6	-
R_{xn}	Constant methane production rate	10^{-17} - 10^{-13}	g-CH_4 g^{-1} wet-sediment s^{-1}

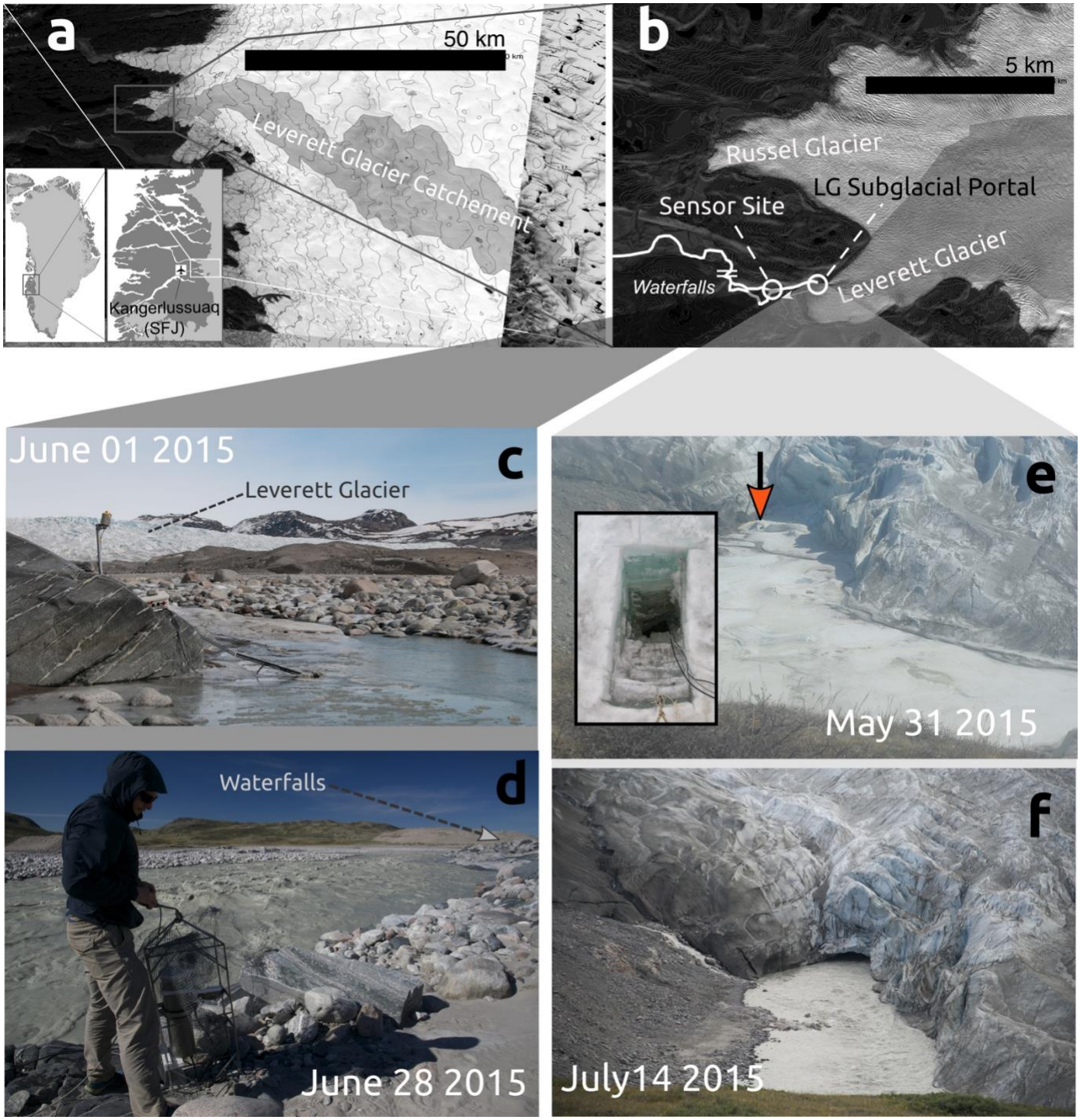

Extended data Fig. 3.5 | Leverett Glacier and proglacial stream. a Leverett Glacier with catchment boundaries(Palmer et al., 2011) outlined in grey. b Zoomed image of the LG with sampling site and portal marked by dots. c Sensor deployment site during the early season with the LG is visible in the background; image faces upstream. d Sensor deployment site in late June; image faces downstream. Also visible is the HydroC® sensor inside steel cage during inspection before re-deployment. e LG portal in late May whilst still covered with both glacial and river ice. Picture was taken an hour before the apparition of the glacial upwelling (see Supplementary section 3.7.2.2). Arrow marked the location of the chainsawed hole, visible in the inlet image. Image of the chainsawed hole was taken on May 10 2015. f LG portal in mid-July 2015. Map images courtesy of USGS/NASA Landsat.

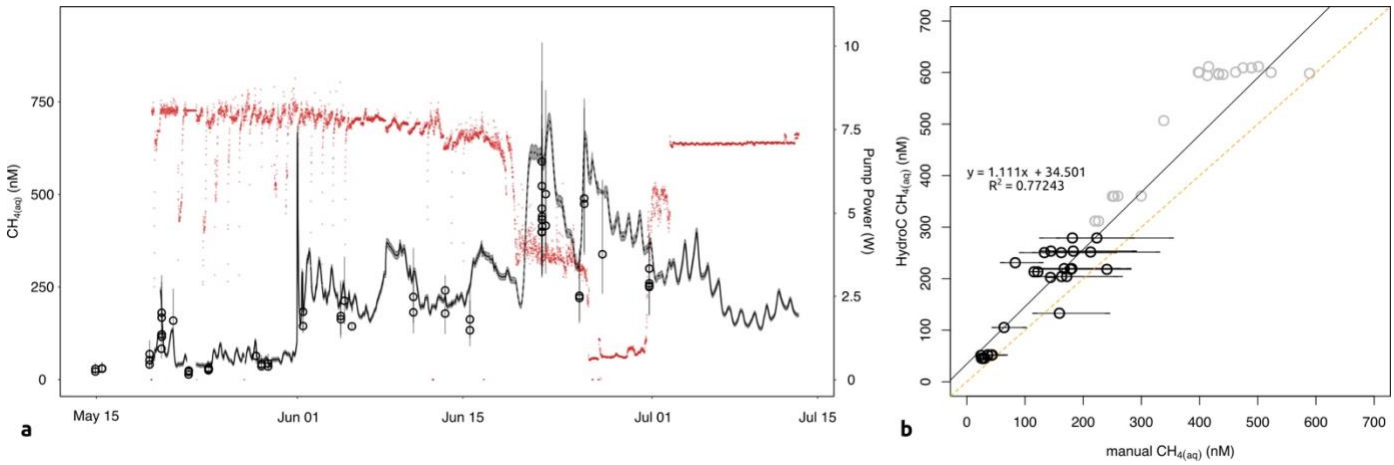

Extended data Fig. 3.6 | Comparison of CONTROS HydroC® and manual sample $CH_{4(aq)}$ concentrations. a $CH_{4(aq)}$ time-series; red points correspond to the CONTROS HydroC® pump power during operation. Continuous line depicts CONTROS HydroC® measurements with the dashed section corresponding to times when the sensor experienced low pump power and thus a reduced water flow induced by the pump (~ June 19 to July 01); open circles correspond to manual samples. The thin shaded grey area ribbon around the $CH_{4(aq)}$ time-series corresponds to the uncertainty of the CONTROS HydroC® measurements (~ ± 3%); uncertainty on manual measurements indicated through error bars reflects error on vial internal pressures and volumes (119 ± 0.76 mL standard deviation; internal pressures are derived from volumes, see Methods for details). b Regression plot between the CONTROS HydroC® and manual sample measurements. Only manual samples taken during times where CONTROS HydroC® pump power was above ~ 7W were considered for the regression (black circles, black line); grey circles correspond to samples taken during times of lower pump power. Horizontal error bars reflect errors on manual measurements; vertical error bars are smaller than size of circles. Orange line depicts a hypothetical 1:1 relationship between the sensor and manual measurements.

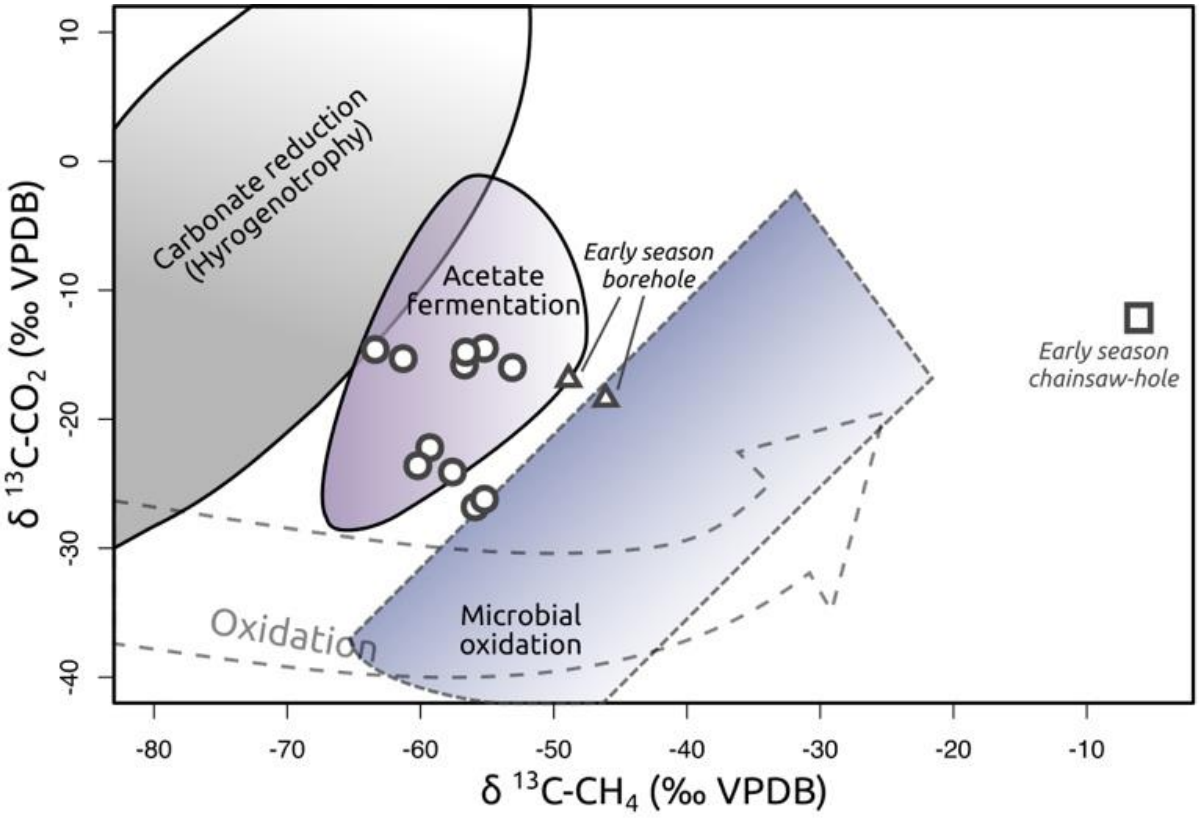

Extended Data Figure 3.7 | Combination plot of $\delta^{13}C$-CO_2 and $\delta^{13}C$-CH_4 of LG runoff. Points denote $\delta^{13}C$ CO_2-CH_4 values for LG manual samples. Methanogenesis and microbial oxidation classification zones are derived and adapted from Whiticar (1999).

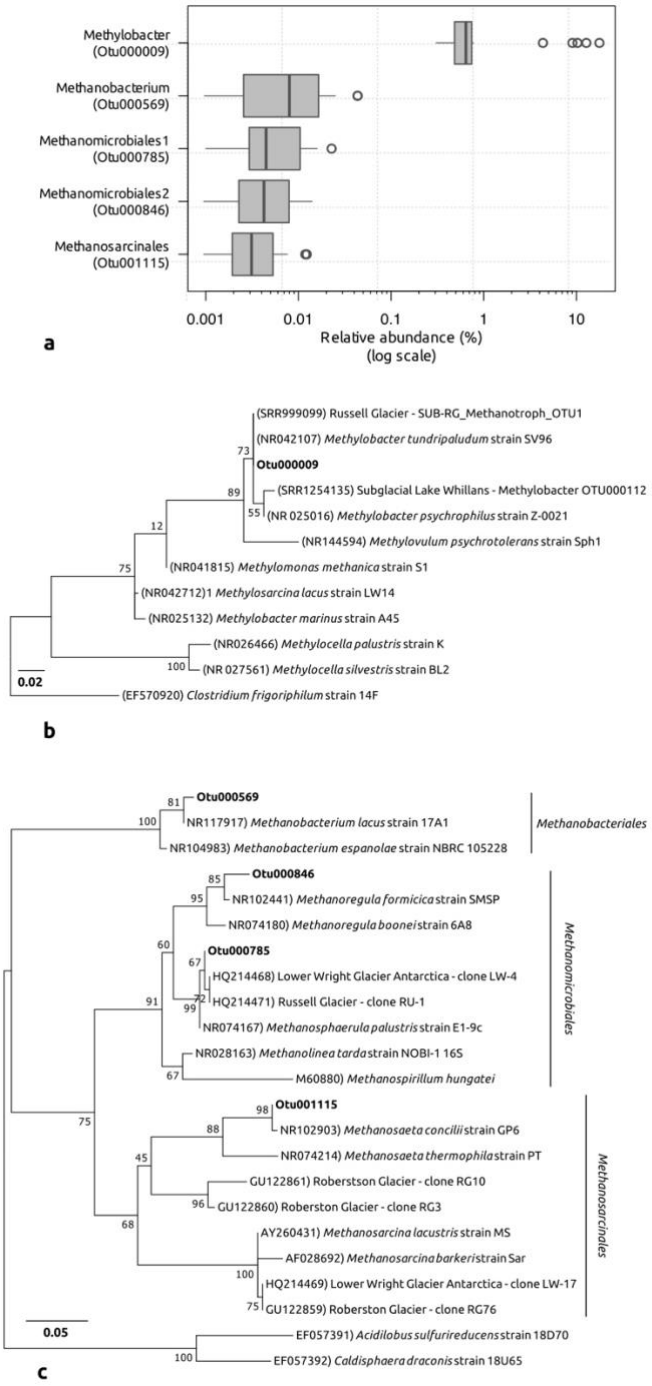

Extended Data Figure 3.8 | LG 16S rRNA gene sequences related to methanotrophic and methanogenic clades. a Relative abundance of the dominant OTUs related to bacterial methanotrophs (OTU00009) and archaeal methanogens; box mid lines represent medians; the interquartile range (IQR) is represented by the lower and upper box boundaries and denote the 25th and 75th percentiles, respectively; whiskers indicate 1.5 times IQR confidence intervals and points are outliers. b, c Maximum likelihood trees of 16S rRNA sequences related to methanotrophs rooted with the sequences of *Clostridium frigoriphilum* (b), and methanogens rooted with the sequences of *Acidibilus sulfurireducens* and *Caldisphaera draconis* (c).

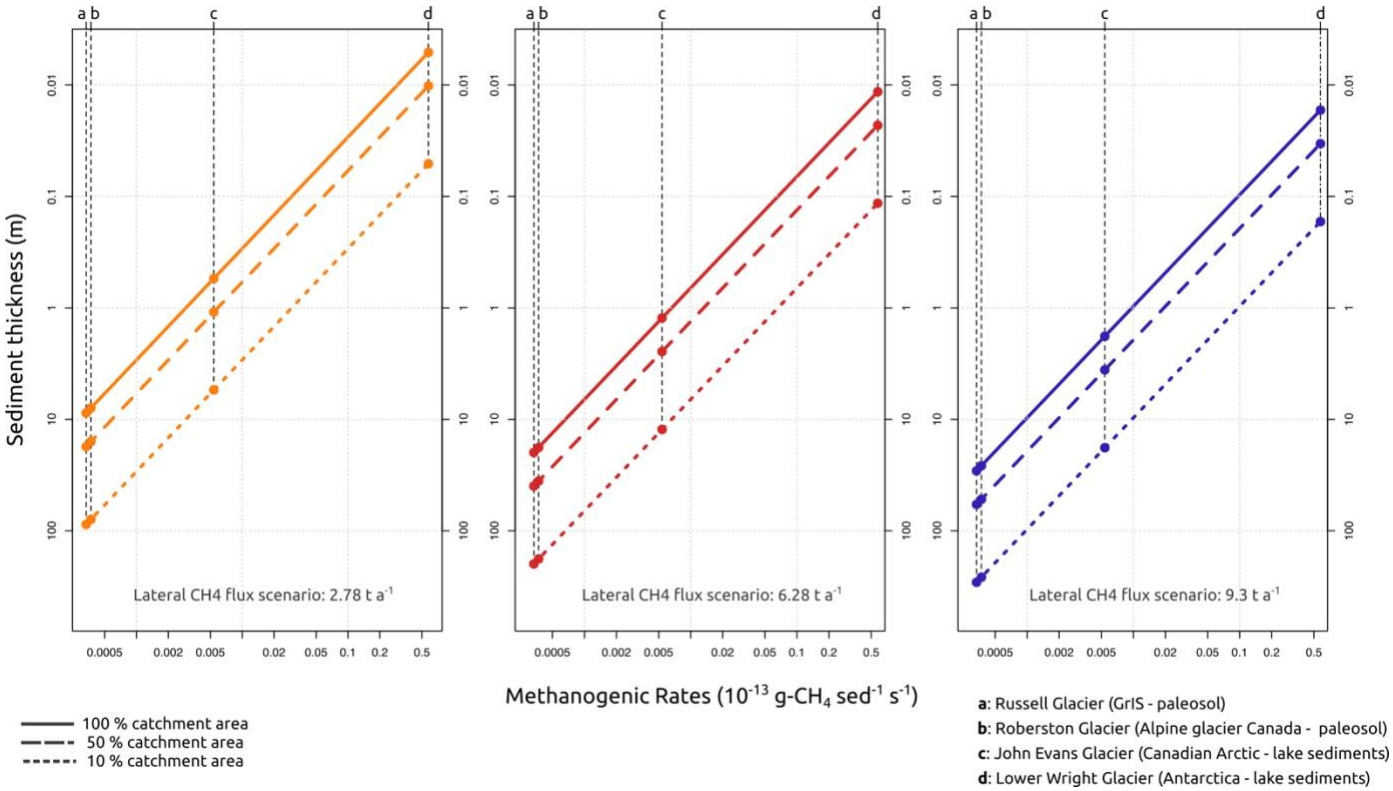

Extended Data Figure 3.9 | Relationship between rates of subglacial methanogenesis, sediment thickness and observed annual CH_4 flux at LG. Each panel corresponds to the different yearly lateral $CH_{4(aq)}$ flux estimates measured in 2015 (see Fig. 2). Each line type corresponds to the sediment thickness required under different catchment area conditions; whether 100%, 50%, or 10% of the subglacial catchment contribute to the observed CH_4 flux. Any point on a line corresponds to the required methanogenesis rate and subglacial sediment thickness to generate the observed lateral CH_4 flux. The four points on each line correspond to known methanogenic rates recorded from different subglacial habitats (Stibal et al., 2012b).

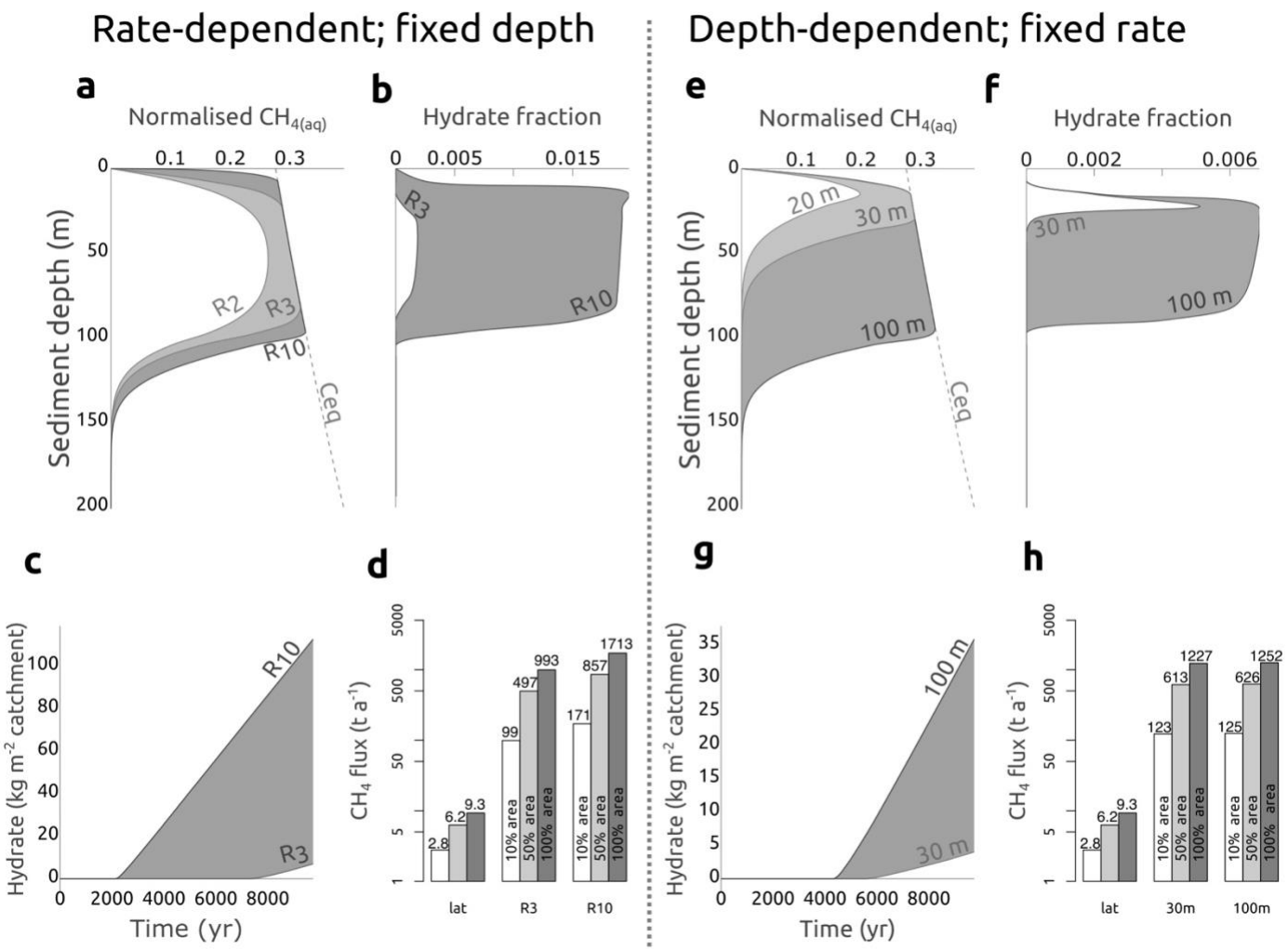

Extended Data Figure 3.10| Summary plot of model conditions required for subglacial methane hydrate formation. Left panel indicate model results under a fixed methanogenic depth (100 m) but varying methanogenic rates (R_2 to R_{10}, i.e. 2 to 10^{-15} g-CH_4 g-sediment^{-1} s^{-1}); right panel outputs model runs under a fixed methanogenic rate (5^{-15} g-CH_4 g-sediment^{-1} s^{-1}) but varying methanogenic depths (20-100 m). a, b, e, f: Vertical profiles of methane solubility, dissolved methane, and methane hydrates; methane concentrations are normalised to Ceq (equilibrium concentration). c, g: Time required for methane hydrate formation under modelled conditions. d, h: Diffusive CH_4 flux at the sediment-ice interface under CH_4-hydrate conditions assuming three different catchment CH_4-hydrates cover area (i.e. 10, 50, and 100 % of the LG catchment), compared to the three lateral flux scenarios (a, b, d; Fig. 2) – see supplementary section 3.7.2.6.

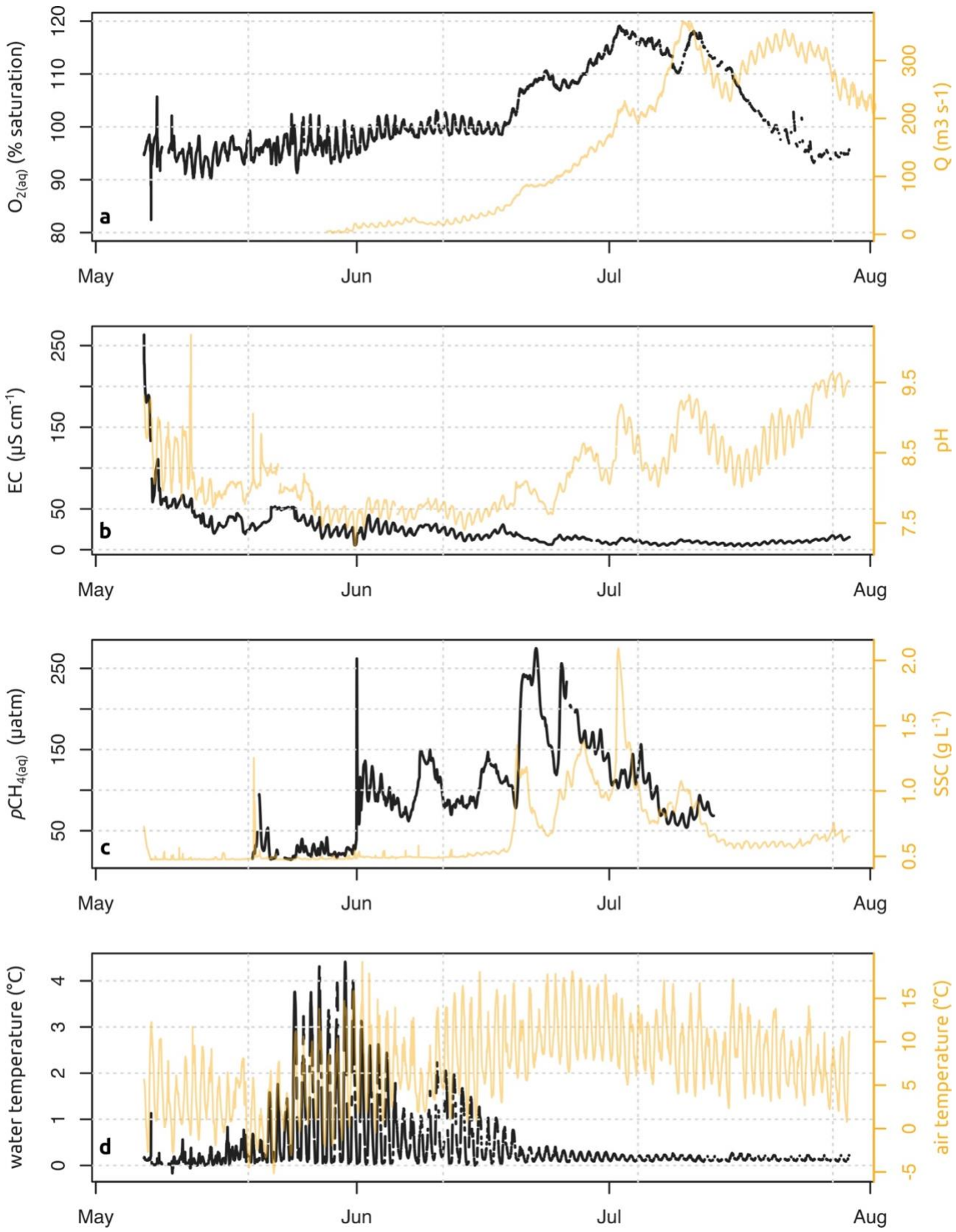

Extended Data Figure 3.11 | Extended time series of geochemical measurements from the LG proglacial river. EC, pH, and SSC time series include the same as the ones depicted on Fig. 1, but extending to measurements before, and after, the methane record. Note that the $CH_{4(aq)}$ data in c are the CONTROS HydroC® partial pressure (µatm) measurements. Y axes corresponding to black and orange datasets are located on the left and right, respectively.

3.7 Supplementary Information

3.7.1 Supplementary Methods

3.7.1.1 Site Description – Leverett Glacier (LG) catchment hydrology and catchment area

The LG acts as the main outlet to the Russell-Leverett catchment, one of the three large GrIS hydrological basins of the Kangerlussuaq area in South West Greenland (Lindbäck et al., 2015). The LG catchment has been the focus of numerous ice-dynamics, hydrology and subglacial biogeochemistry studies in the last decade, and is considered to be highly representative of large areas of Greenland due to its relatively large catchment area, underlying geology (Precambrian orthogneiss and granite) common to much of Greenland (Dawes, 2009), and hydrology easily scalable to large regions of the GrIS based on modelled ice sheet runoff and LG discharge (Bartholomew et al., 2010; Bartholomew et al., 2011; Cowton et al., 2012; Chandler et al., 2013; Tedstone et al., 2013; Hawkings et al., 2014; Hawkings et al., 2016). Basal conditions at LG are polythermal, similar to much of the Western margin of the ice sheet which is considered thawed at the bed (MacGregor et al., 2016). The southwestern margin of the GrIS has also experienced the highest degrees of warming in the past decades and is considered the most sensitive ice-sheet region in Greenland to projected temperatures increases in the 21st century, consequently bearing the largest meltwater contribution from the ice sheet (Tedesco et al., 2013); the LG catchment is therefore located in a hydrological "hotspot" of the ice sheet margin.

The LG (surface) catchment covers an area of ~ 1200 km^2 based on surface elevation, extending up to ~ 80 km from the GrIS margin (Palmer et al., 2011); an area of ~ 600 km^2, however, more accurately depicts the extent of the subglacial catchment (Cowton et al., 2012), with an efficient, fast flowing channelized subglacial system extending to at least 41 km, but less than 57 km, from the ice margin (Chandler et al., 2013). The relatively large area of the catchment, but, arguably more importantly, the relatively large runoff contribution and very high basal erosion rates at LG makes it of particular interest to understand and evaluate GrIS-wide processes. Overeem et al. (2017) recently surveyed > 160 Greenland outlet glaciers and illustrated that *in situ* measurements of sediment export at LG agreed with satellite and model estimates of Greenland-wide sediment exports to the global ocean. Based on the authors' estimates, the LG catchment ranked 22nd in terms of subglacial catchment area and experienced the 10th largest annual water discharge and 4th highest sediment load of all surveyed catchments.

3.7.1.2 Pre melt-season measurements of ice-margin $CH_{4(aq)}$

In early May, prior to the onset of the melt season, water samples were collected and sensor measurements performed beneath the frozen proglacial river, directly in front of the LG portal (~20 m downstream of the then-closed subglacial portal; Extended Data Figure 1). Water samples (n=4) were collected on May 2 and 4 through river-ice boreholes (ice thickness ~ 3 m) using the peristaltic pump (see methods). The HydroC® CH_4 sensor was also temporally (~24 hours) deployed in a chainsaw-cut hole on May 13. $CH_{4(aq)}$ concentrations in the borehole were ~5.6±0.8 µM and chainsaw hole ~3.5±0.4 µM respectively (mean ± standard deviation).

3.7.1.3 Catchment-normalised areal $CH_{4(aq)}$ yield calculations

In order to allow catchment-wide comparison between methane fluxes observed at LG and other systems, catchment-normalised areal yields of $CH_{4(aq)}$ were calculated instead of catchment-wide yields from diffusive fluxes normally reported for gaseous species. Lateral fluxes of $CH_{4(aq)}$ most likely account for a larger portion of overall fluxes in glaciated catchments (because most of the catchment is capped by ice) than non-glaciated river basins, where they only amount to a very small fraction of the total fluxes (Extended Data Table 3.1). Lateral inputs of $CH_{4(aq)}$ feeding proglacial streams are also constrained to a focal source (i.e. ice margin) at the head of the river (as opposed to continuous lateral inputs from smaller-order streams and tributaries to river mainstems), and lateral fluxes from downstream and upstream of the measuring site at LG would be lower and higher, respectively, dependent on methane losses relative to our measuring site.

As opposed to diffusive fluxes, riparian $CH_{4(aq)}$ yields (derived from lateral fluxes) are directly dependent on discharge (and upstream catchment area). LG $CH_{4(aq)}$ concentration measurements were constrained to a single measuring location; consequently, the reported yield is also constrained to the measurement site (methane yields obtained upstream of the measuring sites would be larger and downstream ones smaller, due to $CH_{4(aq)}$ sinks). To more directly compare $CH_{4(aq)}$ yields between LG and other river systems, we focused comparisons to published datasets where both $CH_{4(aq)}$ concentrations and discharge measurements, and ideally drainage-basin area, were available for the same sampling location.

i. Leverett Glacier

The catchment-normalised $CH_{4(aq)}$ yield for the LG site was calculated using the product of the $CH_{4(aq)}$ discharge-weighted mean (i.e. 271 nM) and the total 2015 cumulative discharge (i.e. 1.45

km^3), normalised to the entire glacier catchment (i.e. 600 km^2). Details on estimates of diffusive fluxes at LG are present in the methods section.

ii. Yukon river

Yields for the Yukon river and tributaries were calculated using USGS datasets for specific Yukon-basin gauging stations, which included locations for the Yukon mainstem (i.e. Pilot, Stevens village, and Eagle stations), as well as locations for Yukon tributaries (Koyukuk, Tanana, and Porcupine stations). Except for the Koyukuk station, 2001-2004 $CH_{4(aq)}$ concentration averages were used for calculations (Schuster, 2003; 2005b; a; 2006); the $CH_{4(aq)}$ concentration value for lower-Yukon tributaries in Striegl et al. (2012) (i.e. 0.77 μM) was used for the Koyukuk station. Discharge-weighted means for each station were used in calculations. Station-specific annual discharge, as well as drainage-basin area, were obtained from the USGS database (U.S. Geological Survey, 2016), and a grand average for all available yearly discharge measurements was used in yield calculations. The reported $CH_{4(aq)}$ yields for the Yukon basin were calculated using the grand mean of discharge-weighted concentration means of Koyukuk, Tanana, and Porcupine for the Yukon tributaries, and Pilot, Stevens village, and Eagle for the Yukon mainstem. Diffusive fluxes and associated catchment-wide yields were directly taken from Striegl et al. (2012).

iii. Lena Delta

Yields obtained for the Lena delta were derived using the overall discharge-weighted mean of the 2009-2010 median $CH_{4(aq)}$ concentrations reported for all three main delta channels (i.e. Trofimovskaya, Bykovskaya, and Olenekskaya channels) in Bussmann (2013). The complete Lena basin area, as well as the 2002-2012 annual discharge mean (total Lena basin as well as specific channel discharges) were used in calculations Fedorova et al. (2015).

Diffusive fluxes were calculated using the average of the three Lena Delta channel fluxes(Bussmann, 2013) assigned to the entire surface area of Lena Delta channels. We assumed that the surface area of all river channels within the delta (3,480 km^2) represents 12% of the entire delta area (29,000 km^2) based on ref. (Muster et al., 2012). The diffusive flux of the delta was then normalised to the entire Lena river basin area (2,486,000 km^2) in order to obtain a catchment-wide areal yield.

iv. Amazon lower-basin (Negro and Solimões rivers)

The Amazon lower basin yields were calculated using discharge-weighted means of site-specific $CH_{4(aq)}$ concentrations and discharges integrated over a range of water level conditions (i.e. low, high and falling water levels) in 2011-2012 (Barbosa et al., 2016). Because drainage area information was not available for each sampling site, discharge-weighted catchment areas of the Negro and Solimões were used when calculating yields of their respective tributaries. In the case of the Negro, we assigned 290,459 km^2 as the catchment area of its tributaries out of the 686,810 km^2 for the Negro mainstem; 560,747 km^2 of catchment area was assigned to the Solimões tributaries out of the 990,780 km^2 for the mainstem (Moreira-Turcq et al., 2003). Diffusive fluxes were directly taken from Table 6 in Barbosa et al. (2016), and associated catchment-wide yields calculated using the mainstem total basin area (Moreira-Turcq et al., 2003).

v. Congo and Amazon basins

The Congo basin and Amazon-wide basin $CH_{4(aq)}$ yields were calculated using the overall mean of $CH_{4(aq)}$ concentrations reported for the entire Amazon and Congo basins, as well as the basin-wide annual discharge and drainage area (Borges et al., 2015a). Unlike the previous sites, the calculated yields only represent gross estimates because no information on sampling-site discharge and drainage-basin area was available. Diffusive fluxes and associated yields for the Amazon- and Congo-wide basins were obtained from Sawakuchi et al. (2014) and Borges et al. (2015b) respectively. In the case of the Congo, the average of the fluxes reported using the "Auf" and "Ray" methods was used (see Borges et al. (2015b)).

3.7.1.4 Molecular analyses of LG runoff

Between ~ 600 – 2000 mL of LG bulk runoff was filtered through Sterivex filters (Millipore, USA) between May 04 and July 26 (n = 31). Sterivex filters were preserved in MoBio RNA LifeGuard solution (MoBio Laboratories, USA) immediately after sampling, frozen inside portable freezer within 1 hour of collection. DNA was extracted using the DNeasy PowerWater Sterivex kit (MoBio Laboratories, USA) following the manufacturer's protocol. Extracted DNA samples were sequenced at the Mr. DNA Molecular Research facility (Shallowater, TX, USA; http://www.mrdnalab.com/) on an Illumina MiSeq platform using the 515f/806r primer pair, which targets the 16S rRNA V4 hypervariable region (Bates et al., 2010).

Sequences were analysed on the mothur platform v.1.38.1 (Schloss et al., 2009) following the mothur MiSeq standard operation procedure (Kozich et al., 2013). Sequences were binned into operational taxonomical units (OTU) at a 97% sequence identity level and classified against the

SILVA (v.123) database. Maximum likelihood phylogenetic trees containing the representative sequence of the dominant OTUs related to methanotrophic and methanogenic sequences were assembled in MEGA v.7.0.26.

3.7.2 Supplementary Discussion

3.7.2.1 Manual samples and CONTROS HydroC® response time

$CH_{4(aq)}$ concentrations obtained by manual samples generally agreed with HydroC® results for most of the measuring period when the sensor's pump power was maintained over ~ 7W; the large error on manual measurements relates to uncertainties of internal vial pressures (i.e. 3.5 ± 0.9 atm) (Extended Data Fig. 3.6). The small deviation between HydroC® and manual sample measurements (Extended Data Fig. 3.6b) may also relate to the presence of air bubbles during manual sampling. Whilst care was taken to exclude any air bubble during sampling, we cannot exclude the possibility that a small amount of air bubbles may have been present in some samples due to the highly turbulent waters during sampling. Air contamination in manual samples would result in a slight underestimation of methane concentrations.

The repetitive drops in pump power during the first parts of the measurement period (May 19 – June 19, Extended Data Fig. 3.6) correspond to the changes in power sources (i.e. solar-charged battery versus back-up generator) to the sensor that were necessary during evenings and mornings. Only solar-charged batteries were used after June 19 (due to increased solar irradiance), reflected by the more stable power output (Extended Data Fig. 3.6). A drop in power to the HydroC® pump (SBE-5T) between June 19 – 30, however, most likely affected the HydroC® response time and measurements during that period may not have accurately captured changes in $CH_{4(aq)}$ concentrations as reflected by a more pronounced difference between manual samples and sensor measurements. The high degree of uncertainty associated with manual measurements, however, limits their use as exact reference points during that period (Extended Data Fig. 3.6). Inefficient pumping of water to the HydroC® can affect the CH_4 equilibration time between the membrane and the detector chamber of the sensor, causing measurement lags.

This drop in pump power was most likely caused by the rapid increases in suspended particulate matter levels during the first two outbursts (Fig. 3.1), which may have impeded the movement of the magnetically coupled impeller (pump power is proportional to pump rate). Despite a probable slower measurement response from the sensor during times of lower pump power,

sharp peaks and troughs in $CH_{4(aq)}$ levels were still captured by the sensor during that period, reflective of outburst events and discrete subglacial methane flushing, as well as diurnal patterns (Fig. 3.1). Because the overall changes in $CH_{4(aq)}$ mimicked changes in SSC, E.C., and pH, we consider them to approximately depict evolution of $CH_{4(aq)}$ concentrations, even if the magnitude of those exports may be under-represented. Correcting for HydroC® measurement lags (Fiedler et al., 2012; Atamanchuk et al., 2015) are unlikely to change the overall $CH_{4(aq)}$ concentration trend observed here with respect to outburst events and diurnal cycles, which happen on the timescale of several hours to days (the HydroC® response time, t_{63}, under optimal conditions at 2-3°C water temperature is < 30 minutes).

3.7.2.2 Evolution of the LG subglacial drainage system and concomitant methane export behaviour

The LG hydrological system displays features which are reported in many glaciers worldwide, and likely is typical of GrIS catchments more generally. Surface meltwaters are routed to the bed via supraglacial openings (e.g. crevasses and moulins) caused by fracturing of the ice, connecting sub- and supraglacial environments. The subglacial drainage system consequently undergoes a seasonal evolution following the upglacier progression of the snowline driven by the increase in surface runoff entering the subglacial environment (Das et al., 2008; Chandler et al., 2013; Hoffman et al., 2016; Christoffersen et al., 2018). It evolves from a slow, inefficient hydrological system with tortuous flow pathways early in the melt season, to a rapidly draining efficient system (Chandler et al., 2013). At LG, subglacial runoff ultimately exits the catchment via a well-defined portal that feeds its proglacial river (Extended Data Fig. 1).

Early melt-season (prior to June 19 2015)

During early sensor deployment, most of the proglacial river was still ice-covered, with waters at the measuring site largely derived from a mixture river-ice meltwaters and marginal runoff (Extended Data Fig. 3.5). The very high EC and pH values recorded during that period, however, also indicate a significant contribution from basal meltwaters (Fig. 3.1). Elevated EC and high pH are indeed typical of subglacial environments, and the geochemistry of the LG proglacial river prior to major melt events in the season is mostly influenced by slow inefficient marginal basal meltwaters from the distributed subglacial system(Bartholomew et al., 2011). Because of the very small discharge in the early melt season, even a small contribution from subglacial waters has an important influence on the hydrochemistry profile of the proglacial river.

Methane concentrations during this period were the lowest recorded (mean ~55 nM) but were significantly higher than background-equilibration concentrations (~4 nM at local water temperatures). The abrupt pulse in methane on May 31-June 01 coincided with the opening of the subglacial conduit at LG, marked by the appearance of a water upwelling through river ice in front of the then ice-sealed LG portal, and resulting in a relative increase in discharge indicative of larger influences from meltwaters (Fig. 3.1). The dramatic increase in methane concentrations and sustained high EC during and following the appearance of the subglacial upwelling most likely reflects the release of over-winter stored subglacial waters enriched in methane from the ice margin (see Supplementary Information 1b). Similarly, the two methane peaks recorded on June 8 and 15 likely represent the connection of proximal distributed system waters, also consistent with rises in EC during those two events (Fig. 3.1).

Outburst period (June 19 to July 13 2015)

Export of long-residence-time subglacial waters from the glacier bed is accentuated during increases in the rate of supraglacial meltwater delivery into the subglacial drainage system, often producing distinct pulses of enhanced water runoff superimposed on the general pattern of runoff growth (Bartholomew et al., 2011). Large pulses of meltwater alter the basal water pressure and enable the expansion of efficient subglacial drainage pathways into previously inefficient areas of the ice sheet bed (Nienow et al., 1998; Stevens et al., 2015). The precise timing of distinct runoff pulses is generally associated with sudden catastrophic drainage of meltwater stored in supraglacial lakes which force a surface-to-bed drainage connection through hydro-fracture, or routing of large volumes of meltwater to the ice-sheet bed via englacial conduits such as crevasses and moulins (Bartholomew et al., 2011; Stevens et al., 2015). Periods of subglacial water release via outbursts are typically accompanied by peaks in electrical conductivity (EC) and suspended sediment, reflecting the evacuation of sediments and solute-rich water from basal environments; pH spikes (Fig. 3.1) are also consistent with increased mobilisation of long residence time subglacial waters which have undergone substantial chemical weathering (Tranter et al., 2002). Herein, we refer to such events as outbursts.

The first outburst on June 19 marked a pronounced increase in meltwater discharge, and the growth of an efficient subglacial drainage system at LG, allowing the rapid evacuation of meltwaters to the ice margin. From this point forward, and during the rest of the observation

period, the subglacial drainage system at LG undergoes a rapid upglacier expansion (Chandler et al., 2013). A series of supraglacially forced outburst events are normally observed at LG during this expansion period where new regions of the bed become accessible and connected to efficient drainage channels (Bartholomew et al., 2011); in 2015 these events occurred broadly coincidently with the step-wise retreat of the snowline to higher elevations, increasing the supraglacial catchment area (Kohler et al., 2017).

The four methane concentration pulses that accompanied the recorded four outburst events during the observation period indicate that newly connected methane-bearing regions of the bed act to sustain methane fluxes beyond the early melt period (Fig. 3.1). It also illustrates that sediment-rich, long-residence-time waters from the distributed drainage system contain high concentrations of methane, which can be rapidly exported to the ice-margin once connected to efficiently-draining channels.

Supraglacially forced pulses in methane concentrations appear to lag those of other geochemical parameters (EC, pH, and SSC; Fig. 3.1). We attribute this lag to a momentary dilution of methane-rich subglacial waters by the sudden input of high volumes of low-methane-concentration supraglacial runoff waters, illustrated by abrupt, but brief, drops in methane concentrations at the onset of the recorded outburst events, where the latter caused increased subglacial pressures. The subsequent abrupt rises in methane levels (most evident during the first two outbursts; Fig. 3.1) can be explained by mobilisation of methane rich distributed system water, associated with the water pressure decrease that likely followed the rapid evacuation of supraglacial lake waters in a newly expanded channelized system. This promoted the flow of distributed water sources along the pressure gradient towards the main subglacial channel (Tranter et al., 2002; Das et al., 2008).

This behaviour is most evident during the first two recorded outbursts, most likely due to a closer proximity to the ice margin and lower discharge, which translate into a more pronounced effect on the methane concentration graph (Fig. 3.1). The effects of these localised events on methane concentrations later in the melt season (outbursts 3 and 4) are indeed dwarfed by a larger meltwater contribution from a more developed channelized drainage system, reflected by the absence of sharp methane pulses following the onset of the two later outbursts, as well as the persistence of a strong diurnal pattern observed during the rising limb of the methane-concentration peaks (Fig. 3.1). Because the overall methane load remained high during those

later outbursts (Fig. 3.1), the absence of sharp methane concentration peaks is likely caused by the continuous dilution from ice melt generated from a larger overall catchment area.

Outburst occurrences at LG are normally limited to the first half of the ablation season, when supraglacial lakes and melt ponds drain and drive rapid expansion of the efficient subglacial drainage system (Bartholomew et al., 2011; Cowton et al., 2012). The evolution of an efficient subglacial hydrological system at LG progresses to ~ 41 km upglacier after reaching a cumulative discharge of ~ 0.78 km^3 based on SF_6 injection tracer experiments (Chandler et al., 2013) (in 2015 a cumulative discharge of 0.78 km3 was reached on July 26). Once fully established, sustained fluxes of solute and suspended sediments in runoff indicate a continued flow contribution by distributed system waters during the rest of the season (i.e. SSC and ions; (Bartholomew et al., 2011; Cowton et al., 2012; Hawkings et al., 2014)). The continuous methane record ended on July 13; the sustained load of methane observed during the end of the measuring period did not indicate any sign of exhaustion of subglacial methane reserves (Fig. 3.1). Like other chemical species (major ions, dissolved organic carbon (Lawson et al., 2014)), we hypothesize that methane export during the second period of the melt season will follow similar behaviour to SSC (Extended Data Fig. 3.11c).

3.7.2.3 Inferred methanotrophy in LG runoff

Methanotrophic rates at LG were not directly measured. However, non-poisoned water samples (without $HgCl_2$ to inhibit microbial activity) revealed a decrease in methane concentrations up to 100-fold relative to microbially fixed samples upon analyses back in the home laboratory (data not shown), indicating that active methanotrophs were present at the site. Moreover, a strong microbial oxidation isotopic signature (Whiticar, 1999) characterised the borehole and chainsaw hole manual samples collected through river ice in front of the LG prior to the onset of the melt season. We attribute the stronger methanotrophic effect (enrichment in heavy stable isotope) of the samples collected in the chainsawed open-hole versus the borehole-collected waters to the likely higher oxygen concentrations present in the surface waters of the chainsaw hole, which had been exposed to the atmosphere for 20 days prior to sampling (Extended Fig. 3.7).

To estimate the impact of aerobic microbial oxidation upon methane concentrations in subglacial channels *en route* to the glacier terminus, we used a previously measured methanotrophic rate from proglacial stream samples of the neighbouring Russell Glacier (RG) (Dieser et al., 2014). RG is part of the same overall ice-sheet catchment as the LG, overlaying same geological settings;

environmental factors impacting microbial oxidation at LG should therefore be similar to the ones present at RG. Moreover, molecular analyses of the LG river revealed that the dominant methanotrophic clade sampled had identical (100% identity) partial 16S rRNA-gene sequences to the one identified at RG (Extended Data Fig. 3.8b).

We therefore consider that the use of the Dieser et al. 2014 reported microbial rate to be representative of the methanotrophic sink at LG. In fact, the RG oxidation rate likely exceeded *in situ* methanotrophy at LG for most our measuring period, given the higher temperature (i.e. 4°C) and higher methane concentrations in meltwaters employed in the Dieser et al. (2014) incubations. The lower LG river temperatures (Extended Data Fig. 3.11d), as well as lower overall methane concentrations (i.e. lower substrate availability), should result in overall lower methanotrophic rates (Lofton et al., 2014; Yvon-Durocher et al., 2014). Additionally, a smaller methanotrophic footprint at LG relative to RG is consistent with the lower relative abundance of 16S rRNA gene sequences related to methanotrophic clades detected in the LG runoff (~ 0.5 to 10 % of total OTUs at LG (Extended Data Fig. 3.8.a)) than at RG (~ 1 – 60 %) (Dieser et al., 2014). As such, we consider the use of the Dieser et al. (2014) microbial oxidation rate to be conservative and likely represent higher limits.

A small methanotrophic impact on subglacial methane during its transit through the glacier drainage system is also consistent with the $\delta^{2}H$- and $\delta^{13}C$-CH_4 isotopic signature of samples collected later in the season, at a time of higher flow and thus, short residence times (see methods). Conversely, water samples collected earlier in the season show more oxidised signatures (Extended Data Fig. 3.7) which is consistent with their source from mostly stagnant waters beneath the river ice in front of the LG, where methane production and oxidation would be expected to be in a near equilibrium state.

A similar methanotrophic effect to these latter stagnant or more slowly flowing meltwaters was also observed in the Antarctic Subglacial Lake Whillans, where microbial oxidation was found to strongly impact the concentrations and isotopic signature of methane diffusing from the underlying lake sediments (Michaud et al., 2017). We therefore suggest that microbial oxidation may have a strong buffering effect on subglacial methane fluxes in steady-state systems (e.g. stagnant subglacial lake waters or in systems dominated by passive, diffusive fluxes), but that the microbial sink observed under such stable conditions may have a much smaller buffering impact

during rapid subglacial drainage events, such as the ones observed here in Greenland, which completely alter the nature of the putative methanotrophic layer.

3.7.2.4 LG methanogen populations and subglacial methanogenic substrates

Overall, archaeal sequences constituted a minority of the recovered microbial diversity of the LG proglacial stream, amounting to less than 1% of the total microbial classified OTUs. Focusing on archaeal diversity alone, however, identified the presence of archaeal sequences related to both hydrogenotrophic and acetoclastic clades of methanogens amongst the most abundant archaeal OTUs (here defined to OTUs amounting to >1% archaeal relative abundance). Interestingly, whereas methane stable isotopes pointed to a dominance of acetate-derived methane generated from the LG catchment (Fig. 3.4; Extended Data Fig. 3.7), three of the four most abundant methanogen-related OTUs from the LG stream most closely matched sequences from hydrogenotrophic methanogens (i.e. related to *Methanobacteriales* and *Methanomicrobiales* strains; Extended Data Fig. 4). It is important to point out that 16S rRNA gene data alone cannot infer microbial activity. The low relative abundance of the methanogen-related OTUs (<0.1% of overall 16S rRNA gene library) further limits the use of molecular data to conclude on the relative contribution of each methanogen clade towards the overall LG methane pool and original methanogenic substrate (H_2 or acetate) utilised by subglacial methanogen populations beneath the catchment.

Acetate-derived methane beneath the LG is consistent with findings of CH_4 originating from relatively old OC from recently deglaciated marginal lakes in the Kangerlussuaq area (Walter Anthony et al., 2012) (Fig. 3.4). The lighter CH_4 stable isotopic signature found in these lakes compared to the LG CH_4 (Fig. 3.4) could partially result from substrate maturation (Whiticar, 1999), where methane from the LG catchment would be generated from older source material. Recent ^{14}C analyses of particulate organic carbon at LG indeed demonstrated average radiocarbon ages of > 4,000 years (Kohler et al., 2017), compared to CH_4 bearing a ^{14}C signature of 1,400 – 1,500 years for Greenland marginal lakes (Walter Anthony et al., 2012). The likely contribution to methane production from multiple pathways at LG is suggestive of a progressive transition from organic (e.g. acetate) to inorganic (H_2/CO_2) methane substrates (e.g. derived from bedrock comminution (Telling et al., 2015)) reflecting a depletion of the labile organic carbon pool in further inland regions, overlaid by the ice sheet for longer time periods. This putative "inorganic switch" is consistent with GISP2 and GRIP ice core, as well as Subglacial Lake Whillans sediment data, which all identified subglacial methane to be derived from H_2

oxidation/CO_2 reduction, as indicated by stable isotopes (Souchez et al., 2006; Miteva et al., 2009; Michaud et al., 2017) (Fig. 3.4).

3.7.2.5 Subglacial methanogenic rates and sediment thickness

The methanogenic rates required to sustain the observed methane flux at LG are dependent on the subglacial habitat present beneath the ice. No consensus exists regarding the state of the bed beneath the GrIS. Studies at LG often assumed a hard bed directly underlying the ice (e.g. in Cowton et al. (2012)), whilst others have alluded to at least meters-thick subglacial sediments for a neighbouring catchment (Dow et al., 2013), as well as sediment layers potentially hundreds of meters thick in other regions of the GrIS (Walter et al., 2014). Orders of magnitude also separate methanogenic rates measured from different subglacial environments, with rates from lacustrine- or marine-derived subglacial sediments from Antarctic glaciers much higher than those reported for Greenland and alpine glaciers overlaying paleosol (Stibal et al., 2012b).

Extended Data Fig. 3.9 describes the relationship between subglacial methanogenic rates and sediment thickness required to sustain the observed methane cumulative exports recorded in 2015. Interestingly, if methanogenic rates observed for Greenland basal ice sediments apply to the LG catchment, at least ~ 9 - 29 m of sediment across the catchment are required for subglacial methanogenic populations to match the annual $CH_{4(aq)}$ flux recorded in 2015 (Extended Data Fig. 3.9). It should be noted that these estimates represent a lower limit on both methanogenic rates and sediment thickness needed to exactly match 2015 methane export, under a scenario where the entire catchment is warm-based with a uniform sediment layer, and where subglacial methane production exactly matches annual methane discharges, ignoring (residual) methane build-up beneath the catchment. The possibility for residual methane to build-up under LG, potentially leading to methane hydrate formation is discussed below. Would only a subsection of the LG catchment contribute to methane export (likely), then thicker sedimentary pockets would be required to account for the observed methane flux (Extended Data Fig. 3.9). Recent seismic evidence from the Russell-Leverett catchment suggests the presence of a sedimentary layer beneath the ice (Kulessa et al., 2017). However, ice flow observations and models, as well as borehole investigations from Western Greenland indicate that if thick sedimentary layers do exist beneath the ice, they likely are patchily distributed (Ryser et al., 2014; Harper et al., 2017).

3.7.2.6 Subglacial CH_4-hydrate evolution

A 1D reaction-transport model was used to assess the plausibility of methane hydrate accumulation in the LG catchment. For this purpose, the model was applied to quantify the magnitude of methane production rates that would be required to accumulate CH_4-hydrates under plausible, but optimal environmental conditions in the LG catchment. Methane hydrates form in the sediment when constant methane production rates exceed the diffusive methane loss through the sediment-ice interface and allow for the accumulation of methane in porewaters beyond the saturation concentration. Simulation results indicated that several tens of meters of sediments, and at least several thousand years are required in order to form and maintain CH_4-hydrate reservoirs at LG (Extended Data Fig. 3.10). Assuming a 100 m thick methanogenic-sediment layer, a methane production rate of ~ 3×10^{-15} g-CH_4 g^{-1} sediment s^{-1} (about two orders of magnitude higher than that observed in GrIS basal ice incubations (Stibal et al., 2012b), Extended Data Fig. 3.9) is required to form CH_4-hydrates after just under 8,000 years of sustained methane production (Extended Data Fig. 3.10 a, b, c). Thinner sediments would require higher methane production rates; e.g. at least 30 m thick sediments are needed to form CH_4-hydrates assuming a sustained methanogenic rate of 5×10^{-15} g-CH_4 g^{-1} sediment s^{-1} (Extended Data Fig. 3.10 e, f).

Because CH_4-hydrate formation requires oversaturation of porewaters, model scenarios that result in the formation of methane hydrates in the LG catchment are associated with high dissolved methane concentrations (close to the methane-hydrate equilibrium line) in shallow sediments and, thus, large concentration gradients at the sediment-ice interface. As a consequence, the catchment wide diffusive methane fluxes through the sediment-ice interface generated under such CH_4-hydrate-stable conditions would result in hundreds of t-CH_4 a^{-1}, over an order of magnitude larger than the observed lateral fluxes at LG (i.e. 2.5-9.3 t-CH_4 a^{-1}; Extended Data Fig. 3.10 d, h). These estimates, however, depend on the overall catchment area bearing CH_4-hydrates (Extended Data Fig. 3.10 d, h). Considering the likely patchiness of sedimentary layers beneath the ice sheet (see above section), it may be possible that distributed, deep sediment sections do exist beneath the LG catchment that could favour methane hydrate evolution and potentially account for some of the methane flux observed at LG. Given our current estimations of overall methane export from the catchment, however, it seems unrealistic that the bulk of methane measured at LG originates from CH_4-hydrate-bearing sediments. That being said, the required conditions to form CH_4-hydrate layers beneath 1,000 m of ice are not

unrealistic for other regions of the GrIS, where thick ice cover has been present for long time periods (>10,000 years) and where thick sedimentary layers are also likely present (Walter et al., 2014).

3.8 Perspective on present-day subglacial methane emissions

As mentioned in section 3.3, the overall GrIS footprint on atmospheric methane emissions is impossible to fully assess currently due to the scarcity of available data. The total quantities of LG subglacial methane estimated to have reached the atmosphere in 2015 upstream of our measurement site (i.e. ~ 1.72 Mg-CH_4; see section 3.3) are extremely small when compared to global annual emissions, which fall in the 100s of Tg a^{-1}, even when upscaled to the entire GrIS (using discharge – e.g. Table 3.1). However, those calculations consisted in very conservative estimates based on global scaling relationships between gas transfer velocities and river hydrology, which we stressed likely underestimated atmospheric methane evasion upstream of our measurement site. Underestimation may result from the under-representation of river turbulence derived from velocity in Raymond et al. (2012) (used in our calculations), but arguably more importantly, the very large pressure differential between the hydrostatic pressure of subglacial waters (and therefore dissolved gases herein) and the local atmospheric pressure at points of first contact between subglacial runoff and the atmosphere (e.g. in channelised subglacial conduits that may not be water-filled near the ice margin). The rapid pressure equilibration that likely occurs during those first contact, may, therefore, lead to very high gas diffusion that could not be measured, nor estimated, in the present study.

The above is supported by observations from two extra studies on subglacial methane emissions, published within only a week/few days of the acceptance date of the manuscript by Lamarche-Gagnon et al. (2019); because each respective research was carried independently and nearly simultaneously, findings could therefore not be considered in the context of each respective publication. Burns et al. (2018) revealed that the bulk runoff from the Icelandic glacier Sólheimajökull was also rich in subglacially-produced microbial methane. There, the authors calculated methane fluxes to the atmosphere about 700 hundred times larger than our estimates from the LG river. Unlike the LG catchment in Greenland, the Sólheimajökull system is largely influenced by geothermal and volcanic activity, and results obtained there can therefore not be directly applied to different ice systems more generally. However, the methane evasion rates measured from their proglacial river largely exceeded (by about two orders of magnitude) non-ebullitive fluxes normally found in non-glacial rivers.

The other recent study was performed very close to the LG site in Greenland, in subglacial cavities on the flanks of the Isunnguata Sermia Glacier (Christiansen and Jørgensen, 2018). The team measured methane gas concentrations in the headspace found beneath the ice margin and marginal subglacial runoff. The fluxes to the atmosphere they calculated were also 100 to > 1,000 times larger than what we could estimate from our more downstream LG site. However, Christiansen and Jørgensen (2018) performed their measurements on a very small section of the ice-sheet during only a few days and they also could not extrapolate their findings more generally. Taken together, however, these three studies suggest that overall methane fluxes from Arctic ice masses could have a measurable imprint on global methane emissions currently, and therefore needs to be better constrained. Unfortunately, latest estimates on both current and future methane emissions from the Arctic still ignore methane of glacial origin (Christensen et al., 2019).

On a different note, a putatively larger subglacial methane budget at LG than those measured by Lamarche-Gagnon et al. (2019) raises questions on the overall (relatively modest) carbon reserves estimated to underlay the present day GrIS (Wadham et al., *In review*). Lawson et al. (2014) calculated that LG exports around 0.5 Gg-C of dissolved organic carbon (DOC) per year (for the 2009 and 2010 melt season). The authors also reported particulate organic carbon (POC) concentrations at LG ranging from about 0.6 to 4 g-C m^{-3}. The reported lateral $CH_{4(aq)}$ flux at LG for the 2015 melt season was estimated to ~ 6.3 Mg-CH_4 (up to ~ 9.3 Mg when accounting for oxidative and evasive losses; see Fig. 3.2). Assuming similar DOC and POC flux at LG in 2015 than for the 2009-2010 melt season, and using the 2015 annual runoff discharge of 1.45 km^3, a back on the envelope calculation indicates that the overall estimated 2015 LG methane export amounted to ~ 0.1 to 0.5 % of all DOC and POC flux. However, would those methane fluxes be underestimated by factors of 100 to 1000, they would account for the majority of, or exceed, overall organic carbon exports from LG. Even if some of the exported LG CH_4 is derived from inorganic carbon, it is estimated that the majority of the methane measured at LG to be generated from acetate (i.e. organic carbon) fermentation (fig. 3.4).

Understandably, the above calculations are currently only based on speculations, but understanding the GrIS subglacial methane reserves arguably has repercussions beyond constraining current day global methane budgets. Larger subglacial methane reserves in Greenland would imply larger microbial habitats (e.g. sedimentary or till layers) conducive to methane production and accumulation (e.g. see section 3.7.2.5; Fig. 3.9), which in turn would

affect the overall estimates of subglacial carbon beneath the ice (Wadham et al., *In review*). The nature of the bed (i.e. hard bedrock or soft sediments or tills) beneath the western margin of the GrIS is highly debated, with reports of both hard bedrock and soft sediments beneath the ice (Nienow et al., 2017). Estimates of subglacial sediments or tills also constrained estimates of overall carbon reserves beneath the ice sheet (Wadham et al., *In review*). Lastly, larger methane reservoirs beneath the GrIS than currently estimated would add more credence to the existence of methane hydrates beneath the ice sheet (see section 3.7.2.6), which could further impact on feedback mechanisms to greenhouse gas emissions during future warming.

4. A microbial window into subglacial Greenland: molecular and biogeochemical interpretation of exported microbial assemblages from a subglacial Greenland catchment

Guillaume Lamarche-Gagnon[1*], Jemma L. Wadham[1], Alexandre M. Anesio[1,2], Jakub D. Zarsky[3], Tyler J. Kohler[3,4], Marek Stibal[3]

[1]School of Geographical Sciences, University of Bristol, Bristol BS8 1SS, UK
[2]Department of Environmental Sciences, Aarhus University, Aarhus, 4000 Roskilde, Denmark
[3]Department of Ecology, Faculty of Science, Charles University, Prague, 128 44, Czechia
[4]School of Architecture, Civil and Environmental Engineering, Ecole Polytechnique Fédérale de Lausanne, CH-1015 Lausanne, Switzerland

4.1 Preface

The present section is intended for publication but has yet to be sent for review.

Author contribution:

G.L.-G. and M. S. designed the study. G.L.-G., J.D.Z., T.J.K. and M. S. collected field samples and extracted nucleic acid. A.M.A. assisted with the bioinformatics analyses. Writing, experimental procedures, analyses and interpretations were performed by G. L. G., with significant contribution from J.L.W.

4.2 Abstract

Ice-sheets overlay putatively widespread and active microbial ecosystems. An active subglacial biota has the potential to impact strongly on the (bio)geochemistry of local, but also downstream, environments. Such impacts partly depend on the distribution of microbial populations, the types of habitats present beneath the ice, but also their (inter)connectivity subglacially as well as to external systems. In the ablation zone of the Greenland Ice Sheet (GrIS), supraglacial meltwaters are routed to the ice-sheet bed during the melt season, flushing out stored subglacial waters, sediments (and cells) to proglacial environments and driving the evolution of the drainage system from distributed (delayed, inefficient flow) to channelised (quick, efficient flow) drainage forms. Here, we report on the diversity, composition, and niche differentiation of microbial assemblages exported in bulk runoff from a large (~600 km^2) subglacial Greenland catchment during the 2015 melt season. Proglacial river samples were collected over a period of subglacial drainage system evolution in order to capture shifts in the putative microbial community alongside hydrochemical transitions. We use high-resolution hydrochemical and hydrological information from the proglacial river to guide microbial (16S rRNA gene) interpretations. Results confirmed that

different microbial community assemblages accompanied major hydrological periods in the seasonal hydrograph, and that periods of enhanced subglacial flushing coincided with specific shifts in microbial composition. Core microbial populations were however retained throughout the melt season and phylogenetic characterisation of dominant populations alluded to a centre role for iron and methane cycling in the catchment, and probably beneath ice-sheets more generally.

4.3 Introduction

The beds of ice sheets and glaciers contain liquid water, glacial tills, and sediments (flour and till) that are hosts to indigenous, active microbial communities (Christner et al., 2014). However, our understanding of the role this subglacial microbiome, as well as its distribution and homogeneity, remains mostly speculative (e.g. Tranter et al., 2005; Hodson et al., 2008). Indirect observations and proof-of-concept experiments suggest that microbial activity has an impact on both subglacial and downstream environments; e.g. by enhancing weathering reactions beneath the ice (e.g. Wadham et al., 2010b; Montross et al., 2013b; Wadham et al., 2013). But validating conceptual models of subglacial ecosystems proves challenging (Hodson et al., 2008).

An increasing number of (molecular) surveys have been performed on samples of subglacial origin, shedding light on the metabolic diversity of subglacial microbes and giving credence to theoretical portrays of subglacial ecosystems (e.g. Hamilton et al., 2013); mainly that they seem driven by chemolithotrophic reactions derived from bedrock minerals and the recycling of buried organic matter by advancing glaciers and ice-sheets during glaciation (Boetius et al., 2015). However, these surveys are often limited to point sampling (e.g. of single marginal basal ice blocks or sediment cores) with poor temporal and geographical resolutions (e.g. Stibal et al., 2012a; Doyle et al., 2013; Montross et al., 2013a; Christner et al., 2014). This is especially true for larger ice-sheet systems where direct accessibility to the subglacial world still hinders on our ability to portray a holistic view of these ecosystems.

Sampling of proglacial rivers draining subglacial catchments offers an indirect access to the subglacial system of land terminating glaciers (e.g. Wilhelm et al., 2013). During the ablation season, surface meltwaters are routed to the glacier's bed, flushing subglacial flours (sediments), basal waters, and concomitantly, cells, to glacial margins and proglacial landscapes (Sharp et al., 1999; Skidmore et al., 2000). Dubnick et al. (2017) combined molecular surveys to high-resolution hydrochemical and hydrological analyses of proglacial waters draining the Kiattuut

Sermiat (KS) glacier in South Greenland over an entire melt season. Closely monitoring the geochemical (e.g. major ions) and hydrological evolution of proglacial runoff can inform as to the provenance of subglacial waters (e.g. subglacial residence time, degree of rock:water contact and weathering), and, consequently, as to the potential separate ecological niches beneath the ice (Tranter et al., 2002; Tranter et al., 2005). The authors demonstrated how hydrological forcing shapes microbial assemblages exported from beneath the glacier during the melt season, supporting previous assumptions (Tranter et al., 2005). However, similar approaches have not been performed on large catchments which might be considered more representative of the wider GrIS.

Here, we take on the approach of Dubnick et al. (2017) and apply it to a much larger (~20 times), well characterised, catchment; that of the Leverett Glacier (LG; >600 km^2 estimated subglacial catchment) draining the Southwestern margin of the Greenland Ice Sheet (GrIS) (Cowton et al., 2012). Similar to KS (and other GrIS glaciers), the LG hydrological subglacial system undergoes an evolution from slow-inefficient, distributed drainage early in the melt-season, to a rapid-efficient channelized drainage later in the ablation period (Bartholomew et al., 2011) (see section 3.7.2.2). However, the LG seasonal hydrological evolution is more expansive than in smaller catchments such as KS, draining longer residence-time waters from more remote, upglacier subglacial sources. The LG seasonal hydrograph also features episodic and abrupt subglacial "outburst" events, which flush out high concentrations of subglacial sediments from poorly hydrologically connected parts of the ice sheet bed; sampling during the outburst period, therefore, allows us to better capture microbial information from more isolated (e.g. distributed) sections of the bed.

A timeseries of microbial assemblages exported into the LG proglacial channel, and downstream mainstem Watson River, has been reported previously. However, it lacked the detailed bulk meltwater hydrochemical data required to link microbial diversity to subglacial hydrology, via inferences around the geochemical environment (Cameron et al., 2017). Subglacial microbial activity was also recently evidenced at LG by the observation of the sustained export of microbial methane from beneath the catchment throughout the 2015 melt-season, alongside DNA sequences related to both methanogens and methane oxidizing bacteria in the proglacial waters (Lamarche-Gagnon et al. (2019); see Fig. 3.8). Here, we push the microbial investigation of the LG catchment further, adding a temporal dimension to the analysis. We also do not limit the investigation to methane cycling, but take a more holistic approach, interrogating the entirety of

the exported microbial assemblages, to see whether different communities are exported during different hydrological periods, and whether the evolution in exported community structure permits inferences regarding potentially different habitats and geochemical conditions beneath the catchment. We then draw some conclusions on the putative functions of key microbial players and parallels with other glacial systems, expanding our results in an attempt to inform on a more generalist microbial view of subglacial environments.

4.4 Methods

4.4.1 Sampling site

The LG is a polythermal land-terminating glacier in Southwest Greenland. The LG hydrochemical system has been extensively studied over the last decade, and is considered highly representative of (sub)glacial processes characteristic of the western margin of the GrIS (Bartholomew et al., 2011; Hawkings et al., 2016). A detailed description of the LG can be found in the Supplementary Information of Lamarche-Gagnon et al. (2019) (section 3.7.1.1).

4.4.2 Water sampling of molecular samples

A brief methods description of water sampling, DNA extraction, sequencing, and bioinformatics analyses is included in Lamarche-Gagnon et al. (2019). More specifically, between ~ 600 – 2000 mL of LG bulk runoff was filtered through Sterivex filters (Millipore, USA) between June 07 and July 26 2015. Earlier samples (May 04-13) were also collected beneath river ice through boreholes and a chainsawed hole in front of the LG prior to the onset of the melt-season and a set of samples collected on June 7th from a subglacial upwelling through river ice ~ 50 m from the glacier's terminus (see Lamarche-Gagnon et al. (2019)). The remainder of the samples were collected approximately 500 m downstream from the LG portal. Supplementary Table 1 details sampling volume, location and pooling of replicate samples. Waters were either collected using 60 mL plastic syringes, or filtered with a peristalitc pump (Portapump-810, Williamson Manufacturing) equipped with silicon tubing. Sterivex filters were preserved in MoBio RNA LifeGuard solution (MoBio Laboratories, USA) immediately after sampling and frozen inside a portable freezer (<10°C) within 1 hour of collection.

4.4.3 Molecular analyses and mothur commands

DNA was extracted using the DNeasy PowerWater Sterivex kit (MoBio Laboratories, USA) following the manufacturer's protocol. Except for L1 and L3 samples, extracted DNA samples were then pooled into triplicates prior to sequencing (Supplementary Table 1). Sequencing was performed at the Mr. DNA Molecular Research facility (Shallowater, TX, USA; http://www.mrdnalab.com/) on an Illumina MiSeq platform using the 515F/806r primer pair (Bates et al., 2010), which targets the 16S rRNA V4 hypervariable region.

Raw sequences were analysed on the mothur platform v.1.38.1 (Schloss et al., 2009) on a remote server, mostly following the mothur MiSeq standard operation procedure (Kozich et al., 2013) – full details on the specific mothur commands used are provided in the Supplementary Section below. In short, sequences were binned into operational taxonomical units (OTU) at a 97% sequence identity level and classified against the SILVA (v.123) database, following quality and chimera checks. OTUs composed of two reads or less (doubletons) were removed from further analyses. Downstream analyses (e.g. alpha/beta diversity analyses) were performed on a local machine on mothur v.1.37.5. Visualisation was performed in R (version 3.5.0) (Team, 2018); the phyloseq package (McMurdie and Holmes, 2013) was used for basic analyses and visualisation of taxonomical data (Fig. 3-4).

In order to simplify interpretations, replicates were merged into a single sample per time point. Merged samples were created by summing up reads for each respective OTUs amongst the same group of replicates. Subsampling of reads for biodiversity analyses was performed on both merged and replicate samples (see below). Most analyses were performed on both merged and replicate samples but some graphical interpretations are limited to merged samples only.

4.4.4 Biodiversity analyses

Beta diversity amongst all samples was visualised using principal coordinate analyses (PCoA) on an OTU similarity matrix calculated using the Bray-Curtis calculator. Prior to the generation of the similarity matrix, samples were first randomly subsampled to an equal number of reads (i.e. 62242 and 124484 for the replicate and merged samples, respectively); subsampling resulted in the omission of samples collected on July 1st (L7s) and L8A (see Supplementary Table 2). Samples L7s and L8A were excluded from all analyses, and, therefore, are not mentioned further

in the present manuscript. Alpha diversity calculations (i.e. Shannon and Inverse Simpson) were performed on the same subsampled files generated for the calculation of beta diversity.

Shannon-Weaver (Shannon) diversity index:

$$H = -\sum_{i=1}^{s}(p_i \, lnp_i)$$

Simpson's diversity index:

$$D = \frac{1}{\sum_i^s p_i^2}$$

Where H and D denote the Shannon-Weaver, and Simpson's indices, respectively, s the number of OTUs in the community, and p_i the proportion of the community represented by OTU i. D^{-1} corresponds to the Inverse Simpson diversity index.

The Shannon index biases diversity measurements more towards overall richness (i.e. the total number of species/OTUs within a sample), whereas evenness (i.e. relative abundance of the separate species/OTUs within a sample) is more heavily weighted in the (inverse) Simpson index (Kim et al., 2017).

4.4.5 Phylogenetic trees

Sequence alignment and phylogenetic tree generation were performed in MEGA v.7.0.26. Sequences were first aligned by ClustalW using default settings. Aligned sequences were then trimmed to the region of interest (i.e. region spanning the 515 to 806 region of the 16S rRNA) and alignments visualised on maximum parsimony trees using 1000 bootstrap using the Jukes-Cantor method.

4.4.6 Hydrological and hydrochemical metadata

In order to interpret changes in microbial community structure within the context of their subglacial sources of export and ecological niche transitions, we also include hydrological and hydrochemical data from LG runoff published elsewhere. Methods for determination of

suspended sediment concentrations (SSC) and discharge measurements can be found in Kohler et al. (2017), as well as Lamarche-Gagnon et al. (2019) (section 3.4.1); processed sensor data is also available in (Lamarche-Gagnon et al., 2019). ^{14}C-POC data was obtained from Kohler et al. (2017). Methods and data regarding monovalent and divalent cation concentrations can be found in Hatton et al. (2019). Broadly, we follow the same hydrochemical interpretation from Hatton et al. (2019) and Dubnick et al. (2017), whereas increases in divalent to monovalent cation ratios (D:M) are interpreted to reflect a larger contribution of carbonate over silicate mineral weathering reactions to the cation load, derived from subglacial waters of shorter to longer residence times, respectively.

D:M is defined as follow, with ion concentrations in μeq L^{-1}:

$$D{:}M = \frac{(Ca^{2+} + Mg^{2+})}{(Na^{+} + K^{+})}$$

4.5 Results

4.5.1 Hydrological and hydrochemical evolution of the LG drainage system

The hydrology and hydrochemistry of the LG catchment has been thoroughly studied over the last decade (see section 3.7.1.1; Lamarche-Gagnon et al. (2019)). Here, we summarise the relevant hydrochemical data from the 2015 field season, which has been described in details previously (see Lamarche-Gagnon et al. (2019), Kohler et al. (2017), Hatton et al. (2019)); we also underline a few additional "hydrological states" that characterised the 2015 melt-season at LG, to better constrain the sources of exported microbial assemblages (discussed further below).

The evolution of the subglacial drainage system at LG, and (its) connectivity to the proglacial river, can be inferred from changes and evolution in discharge, turbidity, and major ion chemistry, summarised on Fig. 1. Except for the early samples (L1s) that were collected from relatively stagnant waters beneath the river ice in early May (see methods), the hydrological state of the LG subglacial drainage system can be inferred at the time of sampling on Figure 1. L3 samples were collected following the appearance of a subglacial upwelling through river ice (~ June 01), which was accompanied by a switch in the relationship between major divalent and monovalent cations (D:M) (Fig. 1c). The emergence of the upwelling also resulted in a rise in dissolved methane concentrations at the sampling site, further indicative of proglacial

connectivity to the subglacial marginal zone from the opening of a marginal subglacial flow path driven by increased melt (section 3.7.2.2).

The series of four pulses in SSC between June 19 to July 15 reflect the rapid drainage of supraglacial lake waters to the base of the glacier (Bartholomew et al., 2011). This large input of supraglacial meltwaters mechanically disrupts the glacier's bed, flushing out isolated waters with longer rock:water contact and high sediment loads from a distributed hydrological system, via a series of subglacial outburst events (Nienow et al., 1998; Tranter et al., 2002). At LG, these outburst waters bear a stronger chemical weathering signal characterised by increased silicate mineral dissolution compared to carbonate mineral dissolution, illustrated by a decrease in the D:M ratio (Fig. 1b; Hatton et al. (2019)). The hydrochemical evolution from a trend of decreasing to increasing D:M ratios following the third outburst event (~ July 5th) may reflect a relative increased carbonate weathering signal from carbonation, hydrolysis and dissolution coupled to oxidation reactions on rock and till surfaces, either freshly exposed following the evacuation of long residence time, over-winter stored waters (and sediments), or "mechanically renewed" in an expanded drainage system experiencing longer contact with fully oxygenated, highly turbulent, surface meltwaters (Brown, 2002). The export of subglacial material from more remote sources can also be inferred by the export of suspended sediments bearing an older particulate organic carbon (POC) content during that period (Figure 1a; Kohler et al., 2017). Lastly, the hydrological period following the last outburst at LG (after July 15) is reflective of a fully expanded, efficient and channelized drainage system (Hatton et al., 2019).

Based on changes in runoff hydrochemistry, flow regime, and SSC, we can therefore separate the microbiological sampling schedule into five time periods (Fig. 1). We herein define these different stages as "pre-melt" (L1 samples); "upwelling" (L3 samples, June 1-18); "outburst", which we divide into two: "early outburst" spanning the first 3 SSC pulses (June 19 – July 3; L4 to L8), and "late outburst" (L9 to L11 samples); and "post-outburst", or channelized, (July 15th onward; L12-L13) periods (Fig. 1).

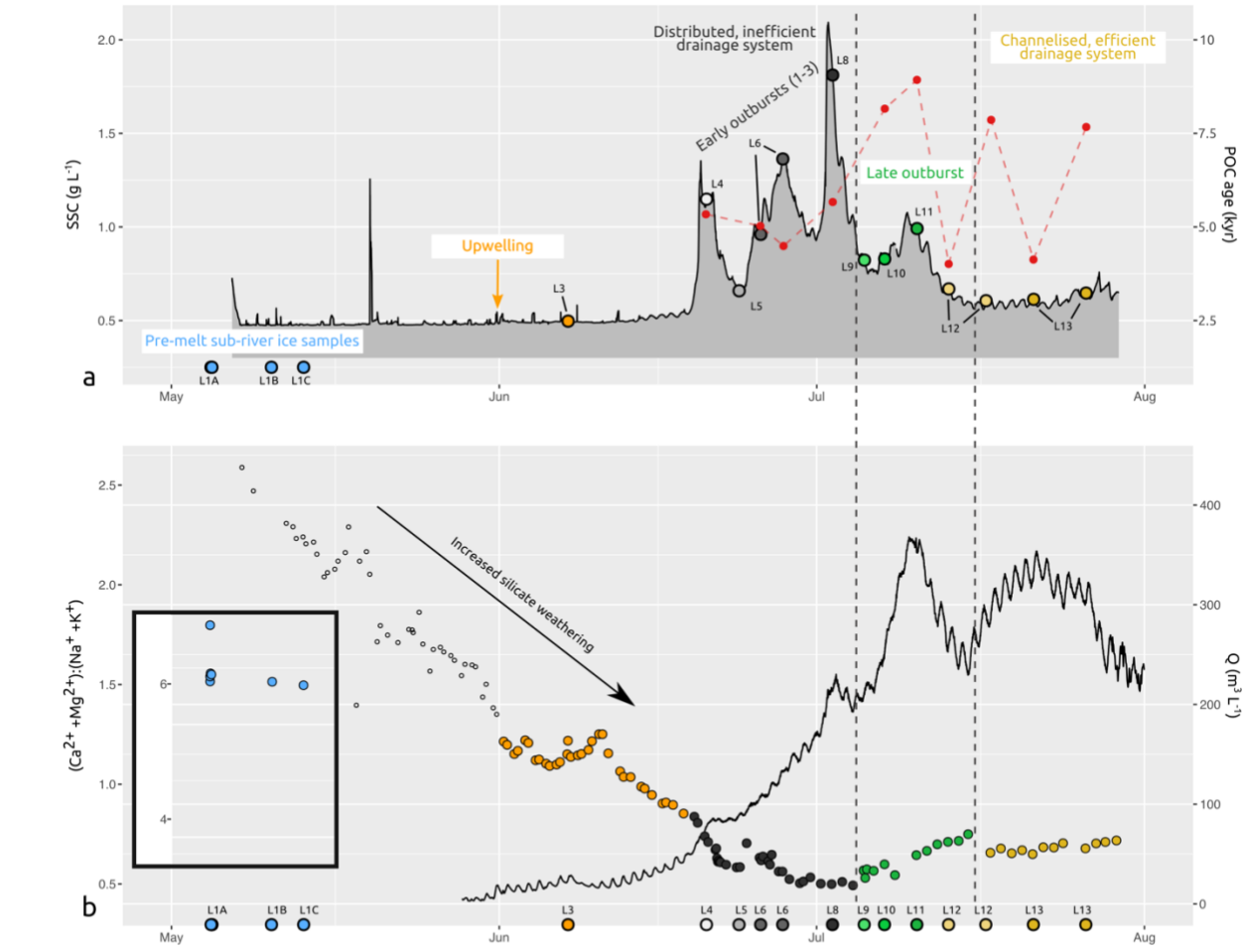
Distributed, inefficient drainage system
Channelised, efficient drainage system
Early outbursts (1-3)
Late outburst
Upwelling
Pre-melt sub-river ice samples
SSC (g L⁻¹)
POC age (kyr)
a
May
Jun
Jul
Aug
L1A
L1B
L1C
L3
L4
L5
L6
L8
L9
L10
L11
L12
L13
Increased silicate weathering
(Ca2+ +Mg2+):(Na+ +K+)
Q (m3 L-1)
b

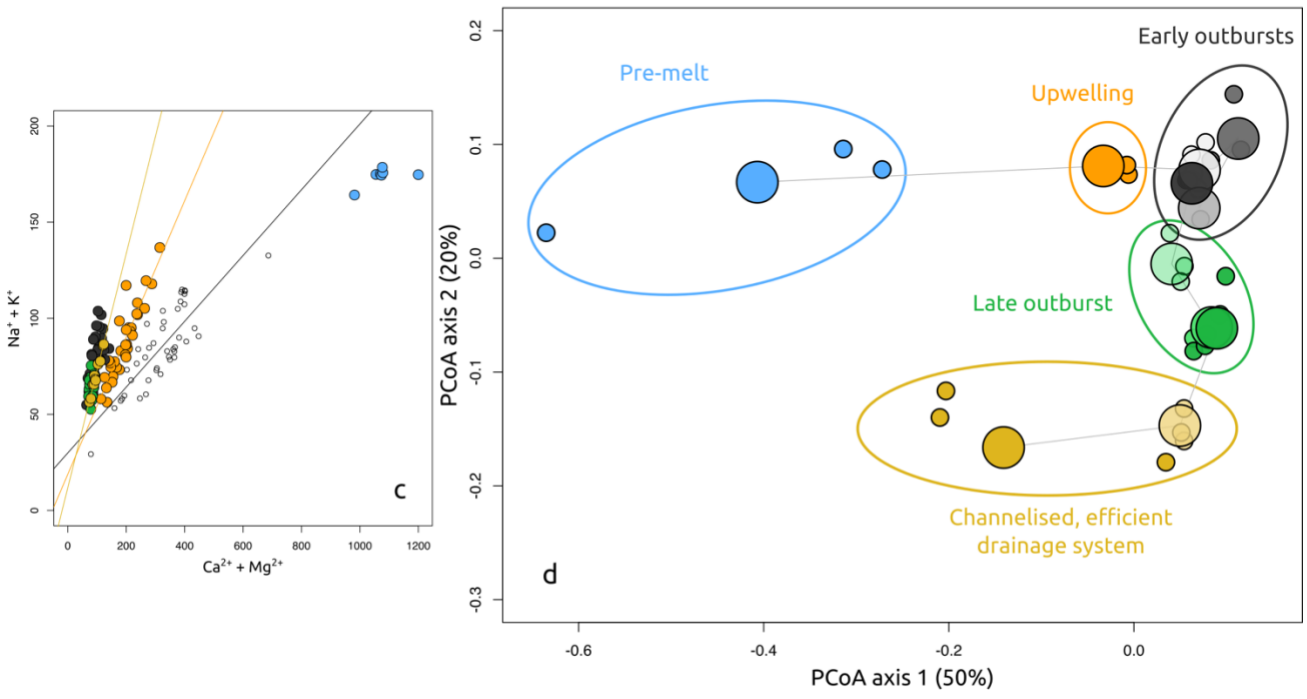
Na+ + K+
Ca2+ + Mg2+
c
Pre-melt
Upwelling
Early outbursts
Late outburst
Channelised, efficient drainage system
PCoA axis 2 (20%)
PCoA axis 1 (50%)
d

Figure 1. **Hydrogeochemical evolution of LG proglacial runoffs, sampling details, and principal component analyses – a**. Timeseries of suspended sediment concentration (SSC) (black) and inferred age of suspended-sediment-associated particulate organic carbon (POC) based on ^{14}C dating in red (data from Kohler et al., 2017). Bordered coloured points indicate sampling time of waters used for DNA extraction overlaid onto the SSC timeseries; L1 samples were collected beneath river ice and no SSC data is available for those samples (see methods). The four abrupt increases in SSC between June 19th and July 15th correspond to outburst events (see section 3.7.2.2; Kohler et al. (2017)). Approximative hydrological states of the LG drainage system are highlighted. **b**. Discharge timeseries (black line) and ratios of major divalent-monovalent cations (D:M; points) of LG runoff (Hatton et al., 2019). Colour of points reflect LG hydrological states; inset shows D:M of sub-river ice waters – note the difference in scale on the y-axis. Sampling time of waters used for DNA extraction are also highlighted as per **a** on the x-axis. **c**. Bi-plot of major divalent to monovalent cation concentrations; concentrations are in µeq L^{-1}. Samples and colour of points are the same as in **b**. Regression lines are for "pre-upwelling" (grey), upwelling (orange), and "late channelized" (tan) samples and highlight hydrochemical transition states of subglacial waters. **d**. Principal component analysis (PCoA) of DNA samples using Bray-Curtis distance matrix. Small dots represent replicate samples and large ones correspond to merged samples (see methods). Colours and groupings are the same as in **a** and **b**. Clusters represent communities grouped by "hydrological states" as per **a** and **b**, with clusters having significantly different centroids (amova, p-value < 0.01). Axes indicate explained level of variation for the merged samples; note the difference in scale between axis 1 and 2. Explained variations for replicate samples is 39% and 13% for axis 1 and 2, respectively. Grey line links clusters by sampling time.

4.5.2 Microbial diversity and evolution of communities' structure

Overall, changes in exported microbial community structure closely followed changes in hydrochemical states of exported waters (Fig. 1d). The most distinct microbial communities are observed for samples collected prior to the onset of the melt-season (L1s) and the very last set of samples from the channelised, efficient drainage period (L13), which clearly clustered separately from those exported during the upwelling and outburst periods (L3-L11) (Fig 1). Such changes are mostly illustrated by shifts along "axis 1" of the PCoA plot, which depicts the highest level of variation amongst communities. Although more subtle, a clear evolution in community structure can also be seen between samples collected following the onset of the melt-season (L3-L11), characterised by shifts along the axis 2 of Figure 1d. Individual outburst events did not appear to flush out distinctive communities. Instead, "outburst communities" appeared to group temporally, with samples flushed out during the first 3 outburst period (~ June 19 to July 5), forming a separate cluster to later ones (L9-L11; ~ July 5-13; Fig. 2). Interestingly, the "transition" in community structure observed between early and late outburst clusters coincided with an apparent change in hydrochemical regime, highlighted by a small change in major divalent to monovalent cation relationship and age transition of exported POC (Fig 2.b-c), likely reflective

of the flushing of subglacial sediments and waters with difference residence times. It should be noted that the L12 samples were homogenised from waters collected during two distinct hydrological stages; both L12 and L13 samples were also grouped from waters and sediments of different POC age, which may have resulted in dampening observed microbial changes that may have occurred during those time periods (Fig. 1a; see methods).

4.5.3 Alpha-diversity

Overall, species richness steadily decreased following the onset of the melt-season, up until the end of the outburst period on July 15 (Fig. 2a). This decrease in richness likely reflects dilution by an increasing volume of supraglacial melt waters reaching the glacier's bed from an expanding drainage area upglacier following snowline retreat on the ice sheet (Kohler et al., 2017). Supraglacial waters indeed contain orders of magnitude less cells than subglacial sources (Cameron et al., 2017). Taking into account OTU relative abundances, however, takes away some the of the dilution effect, and portrays a more nuanced biodiversity trend. Whilst individual outburst events did not appear to flush out distinct communities, they were accompanied by an apparent, localised, increase in biodiversity (Fig. 2b-c). Because of the small sample size (duplicates/triplicates) at each sampling points, this observation remains mostly qualitative. However, when grouping samples collected during outburst events compared to adjacent "in between" ones (e.g. L4-L6 compared to L5, as well as L11 compared to L10-L12), differences in means are statistically significant for both the Shannon and inverse Simpson indices (t-test, $p < 0.05$).

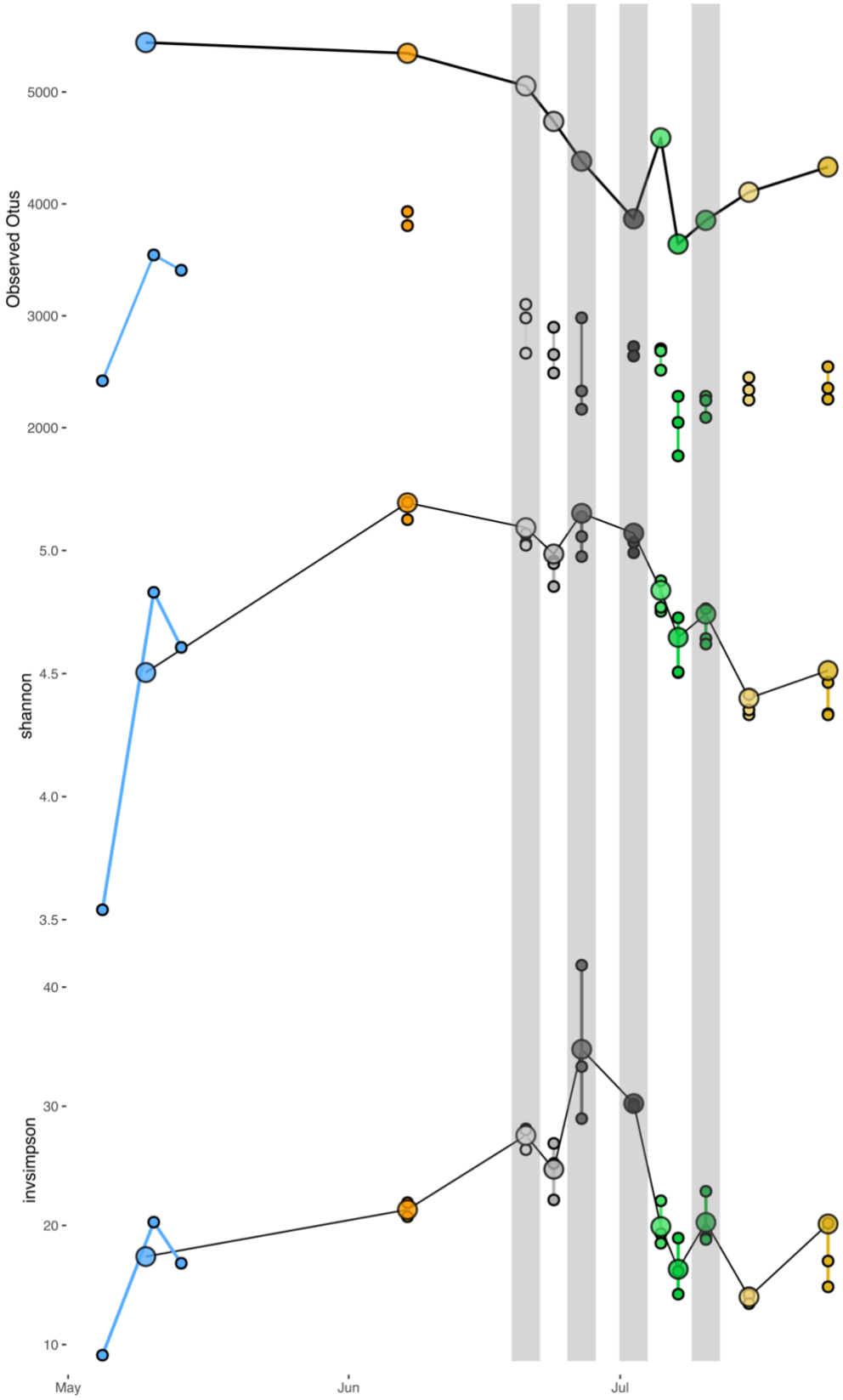
Observed Otus
5000
4000
3000
2000
shannon
5.0
4.5
4.0
3.5
invsimpson
40
30
20
10
May
Jun
Jul

Figure 2. Changes in alpha-diversity observed amongst exported LG microbial assemblages. Highlighted are samples collected during outburst events. Colour palette is the same as in Figure 1. Large points correspond to merged samples, and smaller points replicates. **a.** Changes in richness (observed OTUs per sample). The larger amount of OTUs observed in the merged samples is an artefact of the pooling process, likely reflective of OTUs unique to individual replicates (see methods). **b.** and **c.** respectively portray Shannon and inverse Simpson indices for each samples.

4.5.4 Community composition

Despite notable differences in community assemblages over the melt season (e.g. Fig. 1d), overall exported communities retained a more or less consistent microbial make-up. At a taxonomic level, for example, all samples were dominated by the order *Burkholderiales*, with a relatively stable composition of *Nitrosomonadales* and *Sphingobacteriales* (Fig. 3a). Differences are nonetheless observed, such as a relatively large proportion *Methylococcales*, and very low abundance of *Flavobacteriales*, present in pre-melt and late samples (i.e. L1s and L13s), the lack of *Xanthomnadales* amongst the most abundant sequences in L1s, and a larger proportion of *Anaerobineales* sequences detected during outbursts (L4s, L6s, L8s, L11s), and L5s (Fig. 3a).

The pattern observed at the taxonomic order level is mostly retained when focusing on major OTUs. The dominance of *Burkholderiales* is reflected by the most abundant OTU across all samples (OTU 1), and differences between pre-melt and late samples is also reflected with the relative abundance of specific OTUs. That is, a much larger relative abundance in OTU 2 (*Xanthomnadales*), 6 (*Flavobacteriales*), and 8 (*Anaerolineales*) is observed for samples collected during the outburst periods (L4s-L11s/12s), whereas OTU 3 (*Methylophilales*), 9 (*Methylococcales*), 11 (*Pseudomonales*), and 16 (*Methylophilales*) were most abundant in the pre-melt and very late (L1s, L13s; Fig. 3b, 4). OTU 7 (*Verruconirobiales*) is mostly present in the very late samples only (L12/13). The stark contrast between the relative abundance of these OTUs is perhaps more apparent when observed as a heatmap (Fig. 4).

Archaea only represented a minority of phylotypes, with the most abundant archaeal OTU (OTU 137) accounting for less than 0.1% of all sequences Lamarche-Gagnon et al. (2019). Isolating archaeal OTUs from the overall communities, however, still illustrates the mark difference between early and late samples with the ones collected during transition and outburst periods, most notably for the most abundant archaeal OTU 137 (Fig. 3c).

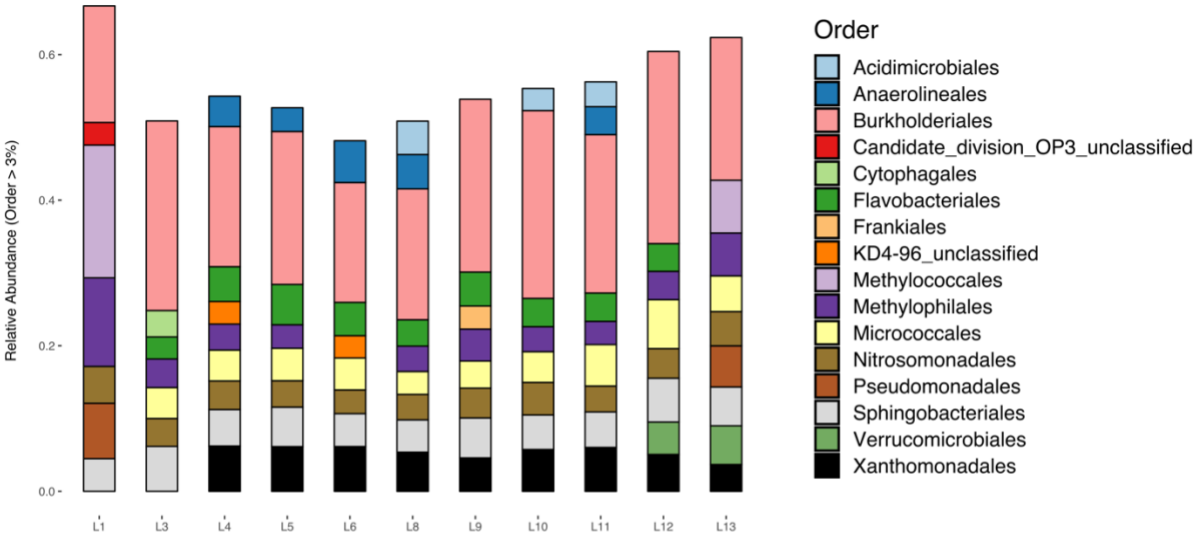
Relative Abundance (Order > 3%)
0.0
0.2
0.4
0.6
L1
L3
L4
L5
L6
L8
L9
L10
L11
L12
L13
Order
Acidimicrobiales
Anaerolineales
Burkholderiales
Candidate_division_OP3_unclassified
Cytophagales
Flavobacteriales
Frankiales
KD4-96_unclassified
Methylococcales
Methylophilales
Micrococcales
Nitrosomonadales
Pseudomonadales
Sphingobacteriales
Verrucomicrobiales
Xanthomonadales

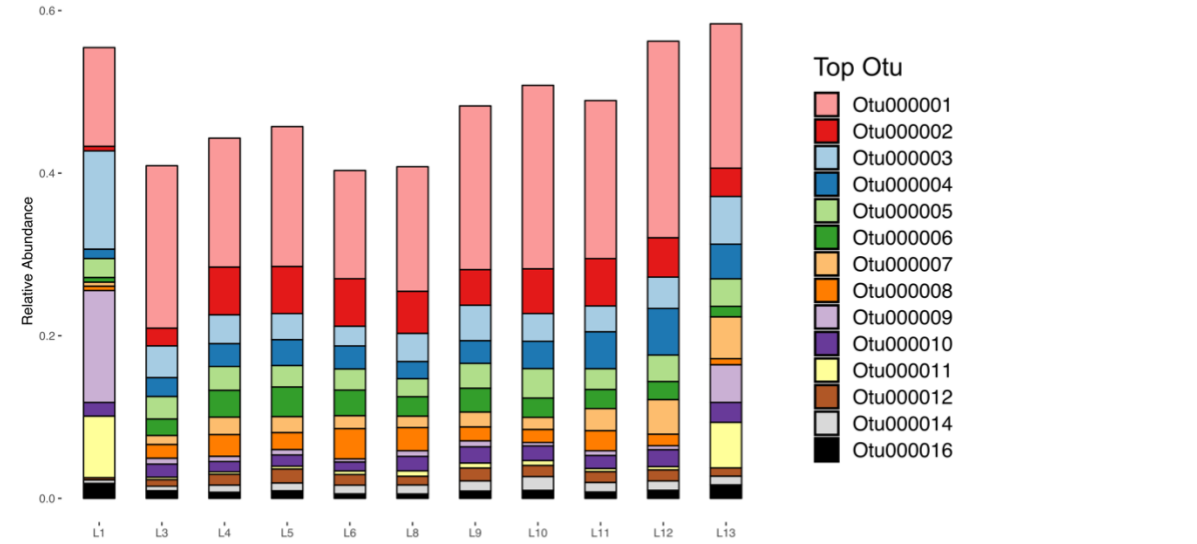
Relative Abundance
0.0
0.2
0.4
0.6
L1
L3
L4
L5
L6
L8
L9
L10
L11
L12
L13
Top Otu
Otu000001
Otu000002
Otu000003
Otu000004
Otu000005
Otu000006
Otu000007
Otu000008
Otu000009
Otu000010
Otu000011
Otu000012
Otu000014
Otu000016

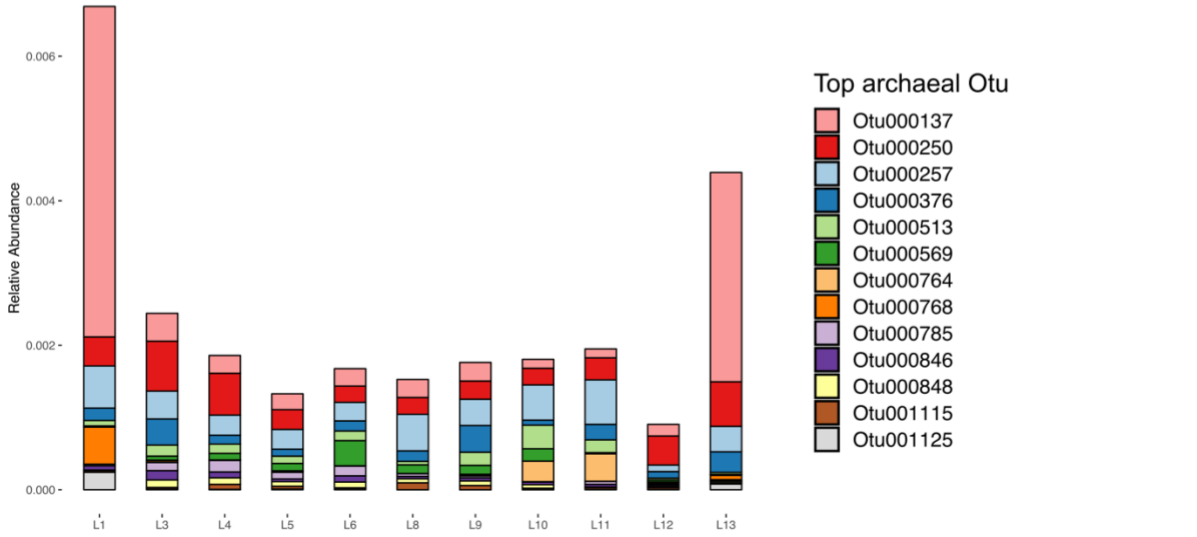
Relative Abundance
0.000
0.002
0.004
0.006
L1
L3
L4
L5
L6
L8
L9
L10
L11
L12
L13
Top archaeal Otu
Otu000137
Otu000250
Otu000257
Otu000376
Otu000513
Otu000569
Otu000764
Otu000768
Otu000785
Otu000846
Otu000848
Otu001115
Otu001125

Figure 3. Relative abundance of major taxa and OTUs of exported microbial assemblages in merged samples. **a.** Barplot of prokaryotic orders accounting for more than 3% of overall taxa across all OTUs. **b.** OTUs amounting for more than 1% relative abundance across all samples. **c.** Archaeal-specific OTUs amounting for more than 1% relative abundance across all archaeal OTUs; note that the overall archaea OTUs amounted for less than 1% of overall OTUs. A barplot of taxonomic and OTU abundance for all replicate samples is included as supplementary figure 1.

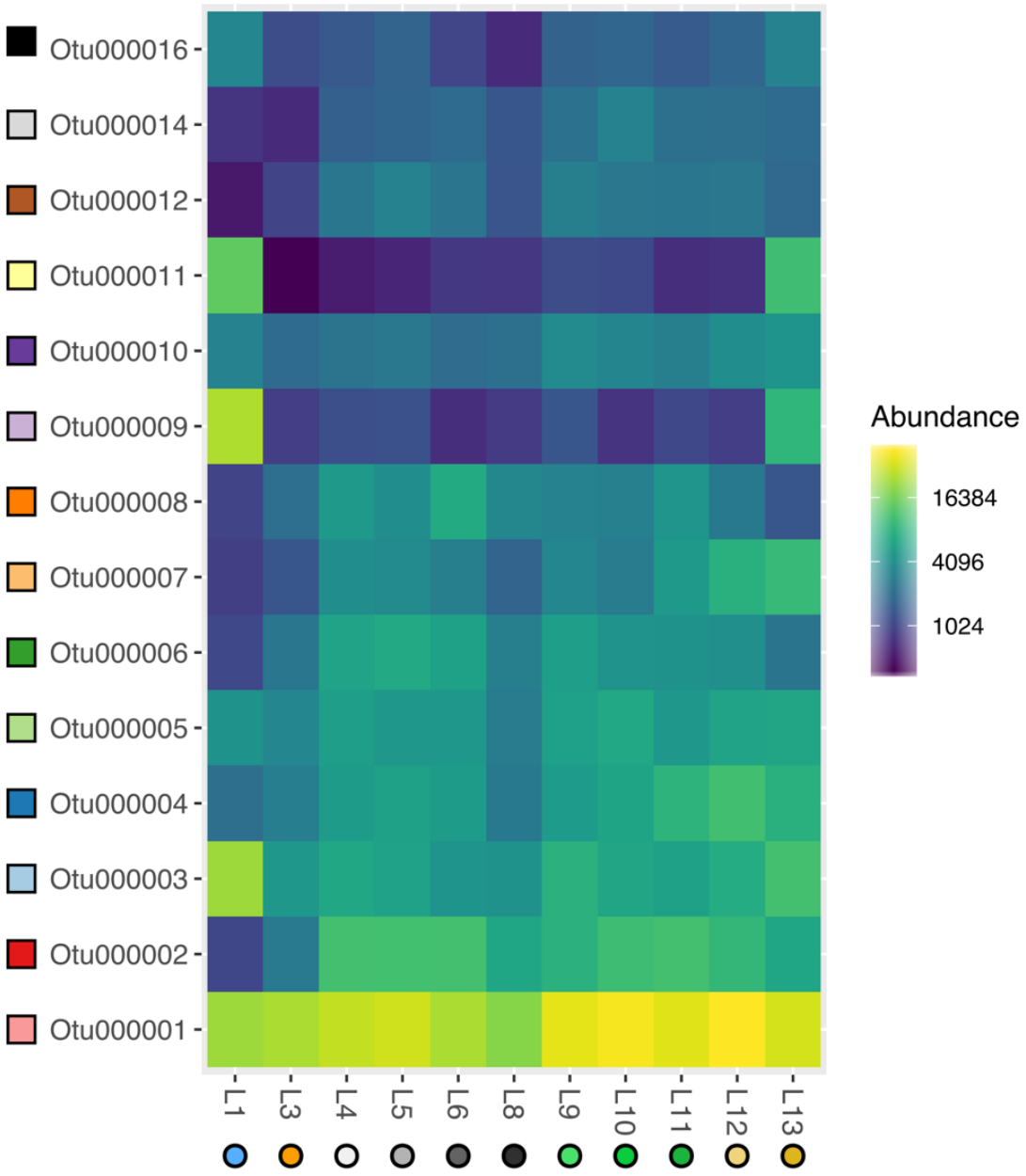

Figure 4. Heatmap of the major OTUs depicted in Fig. 3b. Colour palettes for OTUs and samples are the same as for Fig. 3b and Fig.1, respectively. Note the abundance scale is logarithmic base 2.

4.5.5 Inferred metabolic functions of exported microbial assemblages

Whilst impossible to unambiguously assign metabolic functions to specific phylotypes based on 16S rRNA sequence information alone, comparison against the public repository can still inform on the putative metabolism of some LG populations. The representative sequence of major LG OTUs most closely matched those isolated from other cold and/or glaciated environments, as well as those involved in methane and iron cycling (Table1). Of particular note is the presence of populations closely related to aerobic methanotrophic bacteria (OTU 9 and 16), as well as both iron reducers (OTU 5) and oxidizers (OTU 1) amongst the dominant phylotypes (Table 1, Fig. 5). Even if archaeal sequences only constituted a fraction of identified populations, it should also be underlined that the most abundant archaeal phylotype (137) was closely related to recently characterised anaerobic methane oxidisers of the clade ANME2-d coupling methane oxidation to iron reduction (Fig. 5c).

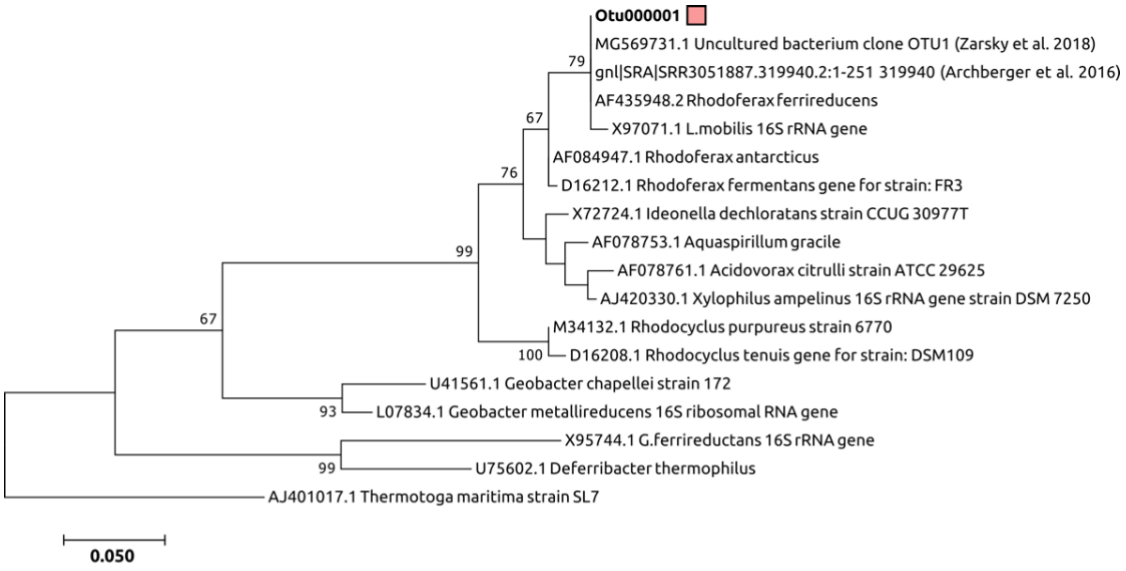
Otu000001
MG569731.1 Uncultured bacterium clone OTU1 (Zarsky et al. 2018)
gnl|SRA|SRR3051887.319940.2:1-251 319940 (Archberger et al. 2016)
AF435948.2 Rhodoferax ferrireducens
X97071.1 L.mobilis 16S rRNA gene
AF084947.1 Rhodoferax antarcticus
D16212.1 Rhodoferax fermentans gene for strain: FR3
X72724.1 Ideonella dechloratans strain CCUG 30977T
AF078753.1 Aquaspirillum gracile
AF078761.1 Acidovorax citrulli strain ATCC 29625
AJ420330.1 Xylophilus ampelinus 16S rRNA gene strain DSM 7250
M34132.1 Rhodocyclus purpureus strain 6770
D16208.1 Rhodocyclus tenuis gene for strain: DSM109
U41561.1 Geobacter chapellei strain 172
L07834.1 Geobacter metallireducens 16S ribosomal RNA gene
X95744.1 G.ferrireductans 16S rRNA gene
U75602.1 Deferribacter thermophilus
AJ401017.1 Thermotoga maritima strain SL7
79
67
76
99
67
100
93
99
0.050

a

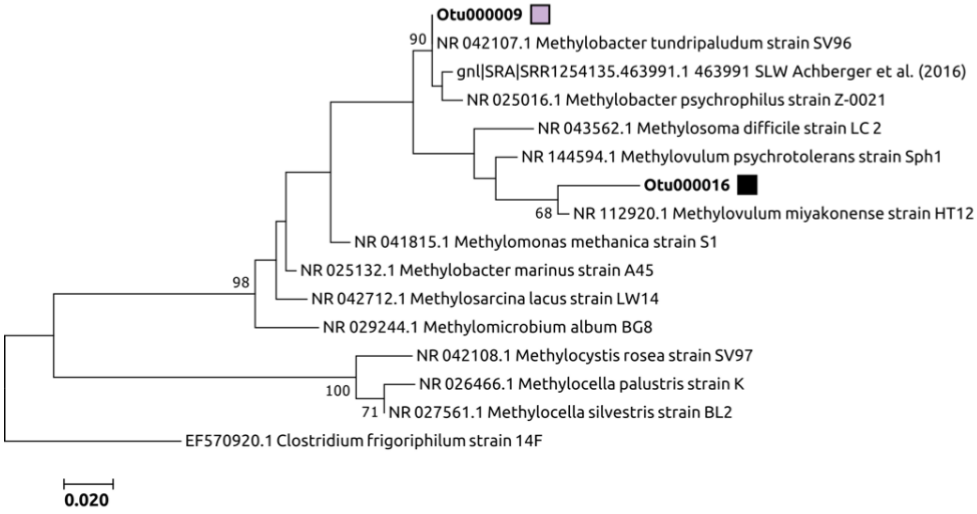
Otu000009
NR 042107.1 Methylobacter tundripaludum strain SV96
gnl|SRA|SRR1254135.463991.1 463991 SLW Achberger et al. (2016)
NR 025016.1 Methylobacter psychrophilus strain Z-0021
NR 043562.1 Methylosoma difficile strain LC 2
NR 144594.1 Methylovulum psychrotolerans strain Sph1
Otu000016
NR 112920.1 Methylovulum miyakonense strain HT12
NR 041815.1 Methylomonas methanica strain S1
NR 025132.1 Methylobacter marinus strain A45
NR 042712.1 Methylosarcina lacus strain LW14
NR 029244.1 Methylomicrobium album BG8
NR 042108.1 Methylocystis rosea strain SV97
NR 026466.1 Methylocella palustris strain K
NR 027561.1 Methylocella silvestris strain BL2
EF570920.1 Clostridium frigoriphilum strain 14F
90
98
68
100
71
0.020

b

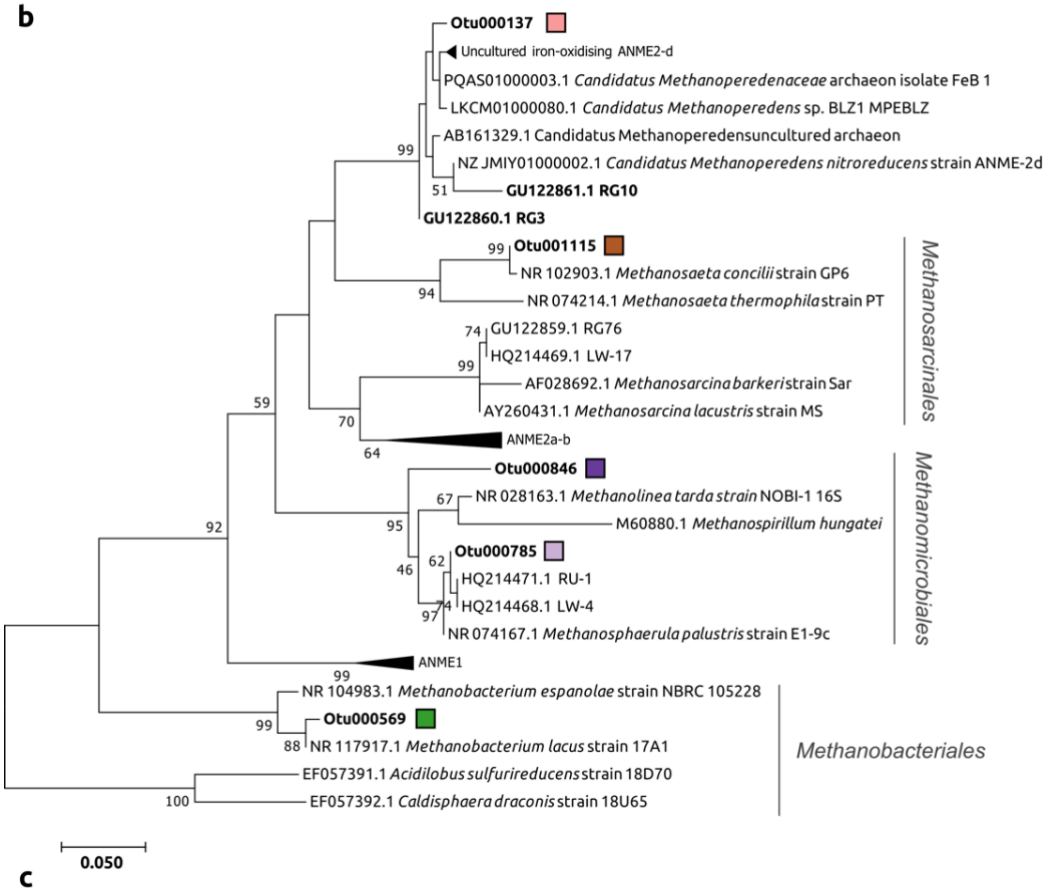
Otu000137
Uncultured iron-oxidising ANME2-d
PQAS01000003.1 Candidatus Methanoperedenaceae archaeon isolate FeB 1
LKCM01000080.1 Candidatus Methanoperedens sp. BLZ1 MPEBLZ
AB161329.1 Candidatus Methanoperedensuncultured archaeon
NZ JMIY01000002.1 Candidatus Methanoperedens nitroreducens strain ANME-2d
GU122861.1 RG10
GU122860.1 RG3
Otu001115
NR 102903.1 Methanosaeta concilii strain GP6
NR 074214.1 Methanosaeta thermophila strain PT
GU122859.1 RG76
HQ214469.1 LW-17
AF028692.1 Methanosarcina barkeri strain Sar
AY260431.1 Methanosarcina lacustris strain MS
ANME2a-b
Otu000846
NR 028163.1 Methanolinea tarda strain NOBI-1 16S
M60880.1 Methanospirillum hungatei
Otu000785
HQ214471.1 RU-1
HQ214468.1 LW-4
NR 074167.1 Methanosphaerula palustris strain E1-9c
ANME1
NR 104983.1 Methanobacterium espanolae strain NBRC 105228
Otu000569
NR 117917.1 Methanobacterium lacus strain 17A1
EF057391.1 Acidilobus sulfurireducens strain 18D70
EF057392.1 Caldisphaera draconis strain 18U65
Methanosarcinales
Methanomicrobiales
Methanobacteriales
99
51
94
99
74
99
70
64
67
95
92
62
46
97
74
99
99
88
100
0.050

c

Figure 5. Maximum likelihood trees of 16S rRNA gene sequences related to major LG OTUs. **a.** Sequences related to iron reducers; tree rooted with sequence of *Thermotoga maritima* **b.** Sequences related to methanotrophs; tree rooted with sequence of *Clostridium frigoriphilum.* **c.** Sequences related to methanogens and ANME clades; tree rooted with the sequences of *Acidibilus sulfurireducens* and *Caldisphaera draconis*. LG OTUs are highlighted in bold with coloured squares identical to those of Fig. 3.b and c for bacterial (**a**, **b**) and archaeal (**c**) sequences, respectively. In **c**, ANME2-d related sequences recovered from Roberston Glacier (Boyd et al., 2010) are also highlighted in bold. SLW refers to Subglacial Lake Whillans. Only bootstrap vales > 50% are shown on tree nodes.

Table 1. Taxonomic and inferred metabolic description of LG dominant OTU representative sequences

OTU #	Order-SILVA	Nearest taxonomic representative	Description of nearest isolate or sequences and inferred metabolism
1	*Burkholderiales*	*Rhodoferax ferrireducens* NR_074760.1 (100)	Fe(III) reducer; psychrotolerant; facultative anaerobe
2	*Xanthomonadales*	*Lysobacter concretionis* NR_114021.1 (95)	Putative anaerobe
3	*Methylophilales*	*Methylotenera versatilis* NR_074693.1 (99)	Related to isolates from glacier communities; aerobe; C1-compound oxidiser
4	*Micrococcales*	*Glaciibacter superstes* NR_041679.1 (99)	Closest isolate from permafrost ice wedge; closest Blast hit from subglacial Greenland runoff (Disko island)
5	*Nitrosomonadales*	*Sideroxydans lithotrophicus* NR_074731.1 (98)	Fe(II) oxidizer; chemolithoautotroph; prevalent at neutral to high pH (at anoxic-oxic transition layers)
6	*Flavobacteriales*	*Aureivirga marina* NR_109513.1 (96)	Related to sequences from groundwater/subsurface environments
7	*Verrucomicrobiales*	*Luteolibacter luojiensis* NR_109500.1 (99)	Related to tundra organism
8	*Anaerolineales*	*Leptolinea tardivitalis* NR_040971 (90)	Putative anaerobe
9	*Methylococcales*	*Methylobacter tundripaludum* NR_042107.1 (100)	Methanotroph isolated from high Arctic active layer
10	*Frankiales*	*Terrabacter aeriphilus* NR_116367 (92)	Closes Blast hit related to sequences from subglacial sediment community
11	*Pseudomonadales*	*Pseudomonas lini* NR_029042 (100)	Facultative anaerobe
12	*Flavobacteriales*	*Aureivirga marina* NR_109513.1 (95)	Closest Blast hits from subsurface systems promoting water-rock-microbe interaction
14	*Hydrogenophilales*	*Thiobacillus thioparus* NR_117864.1 (99)	Closest Blast hits from Antarctic microbial mat; putative chemolithoautotroph and sulphide oxidiser
16	*Methylococcales*	*Methylovulum miyakonense* NR_112920.1 (96)	Methanotroph

Listed orders from the SILVA database (Quast et al., 2012). Nearest taxonomic members are from Blastn searches; percentage identity to the OUT representative sequence is listed in parenthesis. Description and inferred metabolism is derived from NCBI entries of nearest taxonomic isolate or sequences.

4.6 Discussion

4.6.1 Hydrological forcing shapes the nature of exported communities at LG

The influence of hydrology and hydrochemistry on subglacial microbial assemblages flushed out by melt waters was previously well demonstrated by Dubnick et al. (2017) on a small southern Greenland glacier (i.e. the KS glacier). By tracking the evolution of the subglacial drainage system, they showed that changes in microbial community structured roughly followed changes in hydrochemistry throughout the melt season.

When compared to the LG system, forcing mechanisms (and associated community changes) described at KS are mostly analogous to the earlier LG season, prior to June 19, and that of the later part of the LG sampling periods where most of the LG catchment experienced efficient channelized flow (~ post July 15) (Hatton et al., 2019). The KS glacier did not undergo supraglacial lake drainage and associated flushing of the glacier bed. Dubnick et al. (2017) described the evolution of the KS drainage system as an ongoing dilution of the subglacial signal by supraglacial waters, with a microbiological signature of exported assemblages approaching that of supraglacial communities as the season progressed. Up until to ~ July 5th (3rd outburst), arguably the opposite effect can be seen at LG, with an increasingly strong subglacial signal, accentuated during outburst events, and also characterised by the release of older bed material indicated by ^{14}C-dating of POC during the last outburst (Fig. 1a).

We argue that the microbial assemblages exported during the outburst period at LG, therefore, are likely to be representative of biota present beneath larger inland ice sheet catchments, characterised by isolated, mostly anoxic distributed drainage systems (Nienow et al., 1998; Tranter et al., 2005). The increase in relative abundance of microbial clades typically composed of anaerobic members during outburst events, such as of the order *Anaerolineales* (Fig. 1a) is consistent with this view. Similarly, the decrease in relative abundance of likely aerobic clades (e.g. OTUs 9, 11, 16; Fig. 4; Table 1) during this period also follows the same logic. The flushing of phylotypes indigenous to distributed subglacial sediments during outburst events can also be inferred by the apparent rises in alpha diversity (Fig. 2). The sharp pulses in SSC characteristic of outburst events reflect the flushing of newly connected, but also heavily mechanically disturbed, sections of the bed by large volumes of supraglacial melt waters entering the subglacial system (Nienow et al., 1998; Bartholomew et al., 2011). Consequently, this mechanical

disruption of the bed during outbursts likely displaces deeper sediment layers encompassing a greater range of ecological niches (e.g. greater range of redox states between more oxidized surface sediments and deeper layers), that could explain the increases in diversity observed for samples collected during these events (Fig. 2).

Niche differentiation between a channelized and distributed system beneath the ice supports previously proposed conceptual models of subglacial habitats (Tranter et al., 2005; Hodson et al., 2008). Oxic meltwaters entering major drainage channels should maintain a more oxidized/aerated environment capable of sustaining (micro)aerobic populations, and create a gradient of increasingly reducing/anoxic conditions with distance from main channels to distributed regions of the bed, more favourable to communities relying on more reduced electron acceptors. As such, the observations of community changes at LG during times of distributed versus channelized flow, respectively characterised by the export of microbial clades related to more anaerobic and aerobic members (Table 1, Fig. 3a,b-4) appear to support those conceptual models of subglacial ecosystems.

4.6.2 Homogeneity of exported subglacial biota

Whilst it appears clear that concomitant changes in runoff hydrochemistry and microbial community structure observed at LG reflect the flushing by meltwaters of different habitats (hosting distinct communities) beneath the ice, the persistence of a core microbiota throughout the melt season (i.e. in every sampled communities) argues for some degree of homogenisation, either regarding the subglacial environment itself, or reflective of mixing processes during transport to the ice margin (or a combination of the two). The most abundant phylotypes detected over the sampling period (Fig. 1b) were present in all samples, with some (e.g. OTUs, 1, 5) exhibiting relatively small variations in relative abundance between sampling times. Such results could reflect some sort of blanket ecosystem dominated by more generalist populations, punctuated with more nuanced, patchily distributed communities in isolated sections of the bed. Alternatively, those stable populations could be mostly constrained to putative hyporheic sections of a hypothesised channel marginal zones (Tranter et al., 2005; Hodson et al., 2008), "ironing-out" signals from more remote sub-ice-sheet populations, resulting in a microbial profile biased towards marginal communities.

This incomplete view of the communities indigenous to a more distributed subglacial system is consistent with the very low abundance of methanogen phylotypes detected, even during outburst events, despite elevated concentrations of methane exported from the catchment (see Lamarche-Gagnon et al. (2019); Fig. 3c, 5c). The co-occurrence of phylotypes between the L1s and other samples also supports the view of a "marginal" signal retained throughout the ablation season, which is also indicated by an apparent reversal in community structure following the outburst period and establishment of a fully channelized drainage system, with later communities (L13s) more similar to those sampled beneath the river ice prior to the onset of the melt season (L1s) (Fig. 1, 3-4). The seasonal persistence of channel marginal microbial populations in runoff samples also implies that the reservoir of cells inhabiting the channel marginal zones (and their associated habitats – e.g. sediment) is large enough to be resilient to high erosion rates characteristic of subglacial environments, as well as the continuous flushing of the subglacial drainage channels by increasingly large volumes of meltwaters during the ablation season. A subglacial microbiome that is resilient to supraglacial inputs also aligns with observations of relatively constant cell concentrations reported for the LG and Watson river over the 2012 melt season (Cameron et al., 2017). The sustained export of core microbial populations throughout the Greenland melt season was also reported previously in small subglacial outflows of a neighbouring glacier to LG, the Russell glacier (RG), as well as at KS (Dieser et al., 2014; Dubnick et al., 2017). It should be emphasised that even if the bulk of the proglacial runoff at LG originates from the supraglacial system, supraglacial populations likely have a minimal impact on the observed communities making up proglacial assemblages. The low abundance of cells in supraglacial waters compared to subglacial ones (Cameron et al., 2017), as well as the very low abundance of cyanobacteria in the exported waters at LG (<0.1% of total sequences, data not shown), a typical bacterial maker of supraglacial environments, point towards a limiting impact of supraglacial populations on the observed communities here. This is consistent with similar findings from the 2012 season at LG (Cameron et al., 2017).

4.6.3 Metabolism of LG subglacial populations

The very high sequence identity (i.e. 99-100%) between several OTUs dominating LG microbial export and well characterised strains suggest that the cycling of iron, methane, and small organic molecules are centre to the metabolism of LG communities (Table 1, Fig. 5). The most abundant phylotype detected in all samples, OTU1, perfectly matched partial 16S rRNA sequences of *Rhodoferax ferrireducens*, a psychrotolerant facultative anaerobe that can reduce Fe(III) using a

range of simple organic compounds (Finneran et al., 2003). Sequences closely related to iron oxidizers (OTUs 5) were also amongst the dominant OTUs identified (Table 1). The presence of both iron reducers and oxidizers amongst the most abundant microbial populations detected here supports the idea that the large levels of nanoparticulate iron measured previously at LG is bioavailable, and by extension that exported iron species from ice-sheets can serve as fertilisers to the surrounding oceans (Hawkings et al., 2014).

High levels of microbially produced methane were detected throughout the sampling period at LG, suggesting the presence of relatively large methanogen populations beneath the ice, despite methanogens amounting for only a very small fraction of overall recovered sequences (Lamarche-Gagnon et al., 2019). LG methane is also considered to support methanotrophy during the melt season and Lamarche-Gagnon et al. (2019) focused on OTU9 as the main methanotrophic player at LG. Whilst OTU9 indeed is the most abundant methanotroph-related phylotype identified here, a deeper look at the recovered LG 16S rRNA sequences identified a larger diversity of OTUs related to known methanotrophic members (Fig. 3-5, Table 1). In addition to OTU9, for example, OTU 16 (amounting to ~ 1% of all sequences) also closely matched sequences of methanotrophic bacteria of the order *Methylococcales* (Table 1; Fig. 5b). Archaea only accounted for a minority of overall analysed sequences. Focusing on archaea alone, however, revealed that the most abundant archaeal phylotype belongs to the recently characterised clade of anaerobic methane oxidising archaea ANME2-d (Fig. 5). More precisely, sequences from the archaeal OTU137 most closely relate to ANME2-d members mediating anaerobic oxidation of methane (AOM) coupled to iron reduction, such as the uncultivated *Candidatus Methanoperedens ferrireducens* (Fig. 5c) (Cai et al., 2018).

Whilst aerobic methanotrophs have been identified previously in subglacial systems (Dieser et al., 2014; Lamarche-Gagnon et al., 2019), the identification of ANMEs at LG constitute, to the best of the authors' knowledge, the first report of anaerobic methane oxidizers in ice-sheet systems. The role of ANMEs has been considered in previous studies on subglacial methane hydrates (Wadham et al., 2008; Wadham et al., 2012), as well as identified in runoff of an alpine glacier (Fig. 5; Boyd et al., 2010). The presence of anaerobic methane oxidizers beneath ice sheets has significance, because they need to be taken into account when estimating their methane buffering capacities to subglacial methane accumulation beneath the ice and subsequent release to the atmosphere (Wadham et al., 2012). Whilst AOM has been estimated as a methane sinks beneath ice sheets, these biogeochemical models have been constrained to considering

sulphate as an electron sink (Wadham et al., 2012). The presence of sequences affiliated to organisms coupling AOM to iron reduction highlights the importance of considering a wider range of anaerobic methane sinks beneath the ice, and further illustrates the importance of oxidised iron as a terminal electron acceptor in subglacial habitats. It should be clarified, however, that the occurrence of AOM beneath the LG catchment should not affect the estimations of methane exports from Lamarche-Gagnon et al. (2019) (see section 3.4.5), given that the reported CH_4 exports were driven by fully oxygenated waters, and thus most microbial sink during exports should be limited to aerobic methanotrophy.

Interestingly, the three putative LG methanotroph phylotypes identified here (i.e. OTU9, 16, 137) exhibited a similar temporal distribution. All three were relatively overrepresented in samples collected in early May, in the high-methane concentration, stagnant waters beneath the river ice (L1s), as well as in the very last set of samples on July 21-26 (L13s), once the subglacial channelized drainage system was fully established after the outburst periods (Fig. 3-4). Because methane concentrations/fluxes remained relatively high throughout the monitoring period, this temporal distribution most likely does not reflect substrate (ie. CH_4) limitation (Lamarche-Gagnon et al., 2019). Instead, it suggests that conditions more favourable to methane oxidation, both aerobic and anaerobic, are likely more prevalent in subglacial channel marginal waters. Higher O_2 concentrations would indeed be expected to be restricted to those systems during and following the melt-season. Similarly, a larger source of oxidized iron may also be constrained to those more oxidized regions of the bed, explaining the similar distribution trend of ANME-related sequences.

4.6.4 Towards a more conserved, widespread, subglacial biota?

Comparing the overall microbial composition of Greenland runoff reported here with a 2012 survey of the LG and Watson rivers by Cameron et al. 2017 suggests a generally conserved export of microbes across seasons, supporting the view of well-established communities beneath the catchment. Different primer sets were used in both studies, preventing direct phylotype comparison, yet the most abundant orders of microorganisms detected in both years were highly similar (e.g. *Burkholderiales* accounted for the dominant order in both studies) (Fig. 3-4; Cameron et al., 2017). High similitudes in community compositions is also observed between the LG communities and the smaller subglacial outflows of the Russell glacier (RG) draining the same overall "Leverett-Russell catchment" (see Lamarche-Gagnon et al. (2019) Supplementary

Information for details; section 3.7.1.1). The use of the same primer pair at RG and here allows for closer comparison of phylotypes. OTU9 was already shown to be identical to the most abundant phylotype at RG, a member of the *Methylococcales* closely related to the arctic methanotroph *Methylobacter tundripaludum* (Wartiainen et al., 2006; Dieser et al., 2014; Lamarche-Gagnon et al., 2019). Interestingly, OTU1 (most closely related to *R. ferrireducens*), also shared 100% identity with the RG sequences (data not shown).

Resemblances in the dominant populations of sub-ice-sheet communities do not appear to be limited to proximal glacial catchments, and are seemingly found in geographically distant and diverse subglacial systems. For example, highly similar sequences to *M. tundripaludum* were detected in the micro-oxic waters and shallow sediments of the Antarctic Subglacial Lake Whillans (SLW), highlighting the versatility and adaptability of the phylotype in (micro)oxic subglacial systems with high methane concentrations (Fig. 5; Michaud et al., 2017). Perhaps surprisingly, we find that partial 16S rRNA sequences identical to those of LG OTUs 1 (Fig. 5a) and 5 (data not shown), respectively a putative iron reducer related to *R. ferrireducens* and oxidizer related to *S. lithotrophicus,* were also amongst the most abundant members identified in SLW sediment (Achberger et al., 2016). Highly abundant bacterial sequences closely related to *S. lithorophicus* were also reported in exported communities of the alpine Robertson Glacier (Boyd et al., 2014), and BLASTn (Mount, 2007) searches of the 16S rRNA gene sequence from *R. ferrireducens* (AF435948.2) against sequences from KS glacier in South Greenland (Dubnick et al., 2017) also returned highly related hits (identity ≥ 99%; data not shown). The most abundant phylotype recovered from suspended sediments of large glacial catchments on Disko Island, Greenland, was also identical to the *R. ferrireducens* related LG OTU1 (Fig. 5; Žárský et al., 2018).

All in all, the presence of these near identical phylotypes, amounting for a majority of the communities of subglacially disparate environments, underlines the similarities of ecological niches present in subglacial systems with highly different residence times, hydrodynamics, and lithologies. These putative key community members argue for a relatively conserved and widespread microbiome beneath ice masses, supporting the view of a basic chemolithotrophic role by core populations (Boetius et al., 2015), centred around iron and methane cycling. As mentioned above, however, such populations are likely constrained to channel marginal zones and/or surface sediment layers influenced by basal melt.

4.7 Conclusion

Our observations confirm that hydrological forcing shapes microbial communities exported from the LG. Similar forcing mechanisms observed in a smaller South Greenland glacier (Dubnick et al., 2017) therefore also seem to hold true for larger GrIS catchments exporting longer residence-time waters. A key difference here, however, was the ability to sample during large flushing events of subglacial sediments (i.e. outbursts), which allowed to capture more detailed information on putative populations indigenous to more isolated, distributed, sections of the ice-sheet bed. Still, an apparent strong buffering signal from channelized marginal zones appear to mask some of the diversity intrinsic to more remote and anoxic subglacial niches, which may ultimately only be sampled via direct access to the subsurface by drilling operations, or potentially via deeper sampling and sequencing efforts.

Even if microbial characterisations described here (and elsewhere) portrays an incomplete view of the different ecological niches present beneath ice masses, results of subglacial microbial diversity appear highly replicable across studies, years, and sampling locations. It appears clear that chemolithotrophy centred around iron and methane cycling plays a key role in driving and sustaining subglacial biota. By taking advantage of emerging, high throughput molecular datasets from different subglacial environments, it may be possible to draw a more holistic and streamlined view of a subglacial microbiome, validating (and updating) previous conceptual models. Of particular interest would be the better understanding of organic carbon cycling beneath ice masses. That is, the relative importance of autotrophic and heterotrophic processes, and the degree of reliance on relic, overburied, organic matter and how such microbial transformation of carbon may differ from other isolated systems, such as deep sea sediments. Validating the importance of rock comminution as an energy source also remains to be tested (Telling et al., 2015; Tranter, 2015).

4.8 Supplementary information

Supplementary Table 1. Sampling and grouping details of collected Sterivex filter samples

Group	Sampling Time	Sterivex code	Replicate label	Volume (mL)	Sampling Site
L1	2015-05-04 18:00	MP14	1A	6000	Portal/borehole
L1	2015-05-04 20:00	L2	1A	1800	Portal/borehole
L1	2015-05-10 11:00	MP16	1B	5000	Portal/chainsaw
L1	2015-05-13 12:00	MP13	1C	4500	Portal/chainsaw
L3	2015-06-07 12:00	L1	3A	400	Upwelling

L3	2015-06-07 12:00	T2	3B	400	Upwelling
L4	2015-06-20 14:00	M1	4A	600	Cliff
L4	2015-06-20 14:00	MP1	4B	600	Cliff
L4	2015-06-20 14:00	W1	4C	600	Cliff
L4	2015-06-20 14:00	L1*	4ABC	500	Cliff
L4	2015-06-20 14:00	W6	4ABC	1000	Cliff portal side
L5	2015-06-23 16:00	MP2	5A	600	Cliff
L5	2015-06-23 16:00	MP3	5B	600	Cliff
L5	2015-06-23 16:00	MP4	5C	540	Cliff
L6	2015-06-25 17:00	MP5	6A	600	Cliff
L6	2015-06-25 17:00	MP6	6B	600	Cliff
L6	2015-06-25 17:00	W2	6C	600	Cliff
L6	2015-06-25 17:00	L2*	6ABC	600	Cliff
L6	2015-06-27 19:00	MP7	6A	600	Cliff
L6	2015-06-27 19:00	MP8	6B	600	Cliff
L6	2015-06-27 19:00	MP9	6C	600	Cliff
L6	2015-06-27 19:00	W4	6ABC	700	Cliff
L8	2015-07-02 12:00	M2	8A	600	Cliff
L8	2015-07-02 12:00	M3	8B	600	Cliff
L8	2015-07-02 12:00	M4	8C	600	Cliff
L9	2015-07-05 12:00	M5	9A	600	Cliff
L9	2015-07-05 12:00	M6	9B	600	Cliff
L9	2015-07-05 12:00	M7	9C	600	Cliff
L9	2015-07-05 12:00	W3	9ABC	600	Cliff
L9	2015-07-05 12:00	W5	9ABC	600	Cliff
L10	2015-07-07 10:00	T3	10A	740	Cliff
L10	2015-07-07 10:00	T4	10B	750	Cliff
L10	2015-07-07 10:00	T5	10ABC	720	Cliff
L10	2015-07-07 10:00	T6	10C	750	Cliff
L11	2015-07-10 11:30	M8	11A	600	Cliff
L11	2015-07-10 11:30	M9	11B	600	Cliff
L11	2015-07-10 11:30	M10	11C	600	Cliff
L12	2015-07-13 11:30	MP10	12A	600	Cliff
L12	2015-07-13 11:30	MP11	12B	600	Cliff
L12	2015-07-13 11:30	MP12	12C	600	Cliff
L12	2015-07-17 00:00	M11	12A	600	Cliff
L12	2015-07-17 00:00	M12	12B	600	Cliff
L12	2015-07-17 00:00	M13	12C	600	Cliff
L13	2015-07-21 12:00	LA	13A	600	Cliff
L13	2015-07-21 12:00	LB	13B	600	Cliff

L13	2015-07-21 12:00	LC	13C	600	Cliff
L13	2015-07-26 11:00	M14	13A	600	Cliff
L13	2015-07-26 11:00	M15	13B	600	Cliff
L13	2015-07-26 11:00	M16	13C	600	Cliff

"Sterivex code" refers to individual Sterivex samples prior to pooling into replicates; codes reflect "in-house" archiving.

Volume refers to the approximate volume of filtrate.

The portal borehole, chainsaw, and upwelling sites are described in Lamarche-Gagnon et al. (2019).

The "cliff" site is the same as described in the supplementary material of Kohler et al. (2017).

4.8.1 mothur commands; batch file

The mothur was run in "batch mode" on a remote server. The complete mothur "logfile" is included as supplementary information.

Initial steps deviated from the mothur MiSeq standard operation procedure (Kozich et al., 2013). Paired sequences from the sequencing centre contained both "forward" and "reverse" reads in both supplied "R1" and "R2" fastq files, preventing the generation of a ".files" or ".oligos" file in mothur; instead, the command "trim.seqs" with an ".oligos" file was used after converting raw reads into contigs. The batch file used to run initial mothur commands for quality checks and OTU generation contained the following commands:

make.contigs(ffastq=45_88_R1.fastq, rfastq=45_88_R2.fastq, processors=31)
trim.seqs(fasta=45_88_R1.trim.contigs.fasta, oligos=Lev_noL2snoBlank.oligos, checkorient=T, processors=31)
summary.seqs(fasta=current)
screen.seqs(fasta=current, group=current, maxambig=0, maxlength=320)
unique.seqs(fasta=current)
summary.seqs(fasta=current)
count.seqs(name=current, group=current)
summary.seqs(count=current)
align.seqs(fasta=current, reference=silva.v4.fasta, flip=T)
screen.seqs(fasta=current, count=current, start=8, end=9582, maxhomop=8)

filter.seqs(fasta=current, vertical=T, trump=.)

unique.seqs(fasta=current, count=current)

summary.seqs(fasta=current, count=current)

pre.cluster(fasta=current, count=current, diffs=2)

chimera.uchime(fasta=current, count=current, dereplicate=t)

remove.seqs(fasta=current, accnos=current)

summary.seqs(fasta=current, count=current)

classify.seqs(fasta=current, count=current, reference=silva.nr_v123.align, taxonomy=silva.nr_v123.tax, cutoff=80)

remove.lineage(fasta=current, count=current, taxonomy=current, taxon=Chloroplast-Mitochondria-unknown-Eukaryota)

summary.seqs(fasta=current, count=current)

cluster.split(fasta=current, count=current, taxonomy=current, splitmethod=classify, taxlevel=4, cutoff=0.15)

make.shared(list=current, count=current, label=unique-0.01-0.03)

classify.otu(list=current, count=current, taxonomy=current, label=unique-0.01-0.03)

Supplementary Table S2 summarises the number of reads in each samples following the "trim.seqs" (initial stage) and "remove.lineage" (final stage) commands.

Supplementary Table 2

SampleID	Initial	Final
L10A	90955	78855
L10B	100653	87914
L10C	78594	69407
L11A	97354	85803
L11B	102383	89316
L11C	120466	105580
L12A	127498	110751
L12B	103948	90591
L12C	112485	98392
L13A	96380	83611
L13B	98034	82311
L13C	109065	89166
L1A	93389	69540
L1B	129635	102590

L1C	128344	99971
L3A	134685	112431
L3B	122893	103475
L4A	111038	95471
L4B	102506	87982
L4C	90831	78985
L5A	114118	98126
L5B	79782	69311
L5C	104764	90167
L6A	109858	94172
L6B	70815	62718
L6C	88473	78229
L7A	**41647**	**36859**
L7B	**30828**	**28083**
L7C	**45686**	**41114**
L8A	**37069**	**33253**
L8B	95257	81292
L8C	99085	85050
L9A	118410	100998
L9B	121614	105199
L9C	108365	92715
Total (unique)	-	271165
Total	3416907	2919428

Highlighted in bold are samples with a lower number of reads, that were excluded from downstream analyses as a result of subsampling (see above).

"Total (unique)" refers to the total number of reads that did not share 100% sequence identity; i.e. were "unique".

4.8.2 mothur commands; local machine

The following commands were performed in mothur (v.1.37.5) on a local machine to remove doubletons (ie. OTUs containing 2 sequences or less amongst all samples), subsample groups to the same level of sequences, calculate a Bray-Curtis (dis)similarity matrix, and generate PCoA coordinates, respectively:

remove.rare(shared=noBlankL2.shared, nseqs=2, label=0.03)

sub.sample(shared=current, size=62242) ## eliminates samples L7s and L8A.

dist.shared(shared=current, calc=braycurtis, label=0.03)

pcoa(phylicp=current)

The same commands were also used on merged samples. Note that samples were first merged from previously subsampled (to 62242 sequences) samples:

merge.groups(shared=noBlankL2.0.03.pick.0.03.subsample.shared,
design=mergeGroups.design)

dist.shared(shared=current, method=braycurtis, subsample=124484)

pcoa(phylip=current)

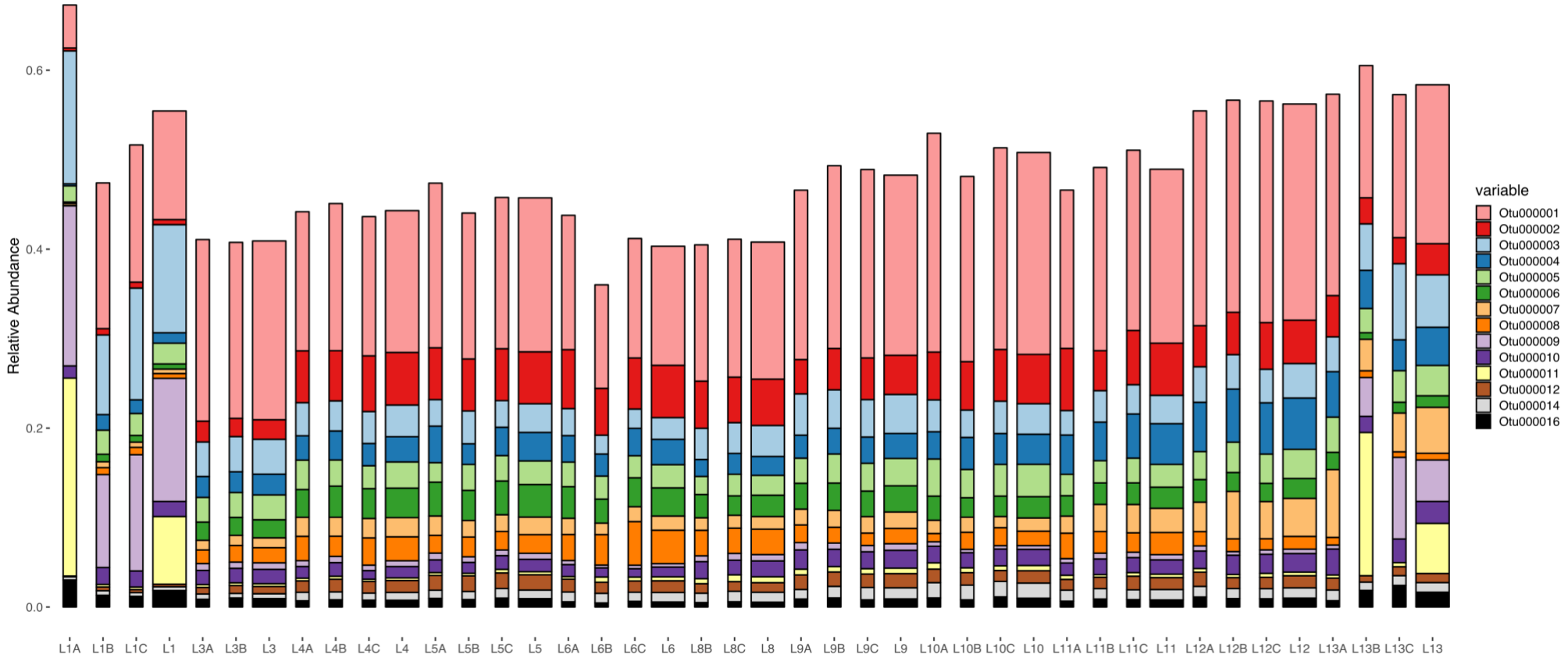

Supplementary figure 1. Relative abundance of major (>1%) OTUs of both replicate (thin bars) and merged (larger bars) samples. The merged samples are the same as depicted on Figure 1.b.

5. Glacial flour as a microbial fuel beneath ice-sheets

Guillaume Lamarche-Gagnon[1], Jemma L. Wadham[1], Jon Telling[2], Jon R. Hawkings[1,3,4], Jade E. Hatton[1,5], Beatriz G. Olivas[1]

[1]School of Geographical Sciences, University of Bristol, Bristol BS8 1SS, UK
[2]School of Natural and Environmental Sciences, Newcastle University, Newcastle NE1 7RU, UK
[3]National High Magnetic Field Lab and Earth, Ocean and Atmospheric Sciences, Florida State University, Tallahassee, FL, USA.
[4]German Research Centre for Geosciences GFZ, Potsdam, Germany
[5]School of Earth Sciences, University of Bristol, Bristol BS8 1SS, UK

5.1 Preface

The present section is intended for publication but has yet to be sent for review.

Author contribution:

G.L.G. and J.T. designed the experiment. J.E.H. performed measurements of dissolved silica. Major ion measurements for time points 1-3 were performed by J.R.H.; measurements for time 4 was performed by B.G.O. (measurements for time point 5 were performed by G.L.G.). Writing, experimental procedures, analyses and interpretations were performed by G. L. G., with significant contribution from J.T. and J.R.H.

Contribution from other researchers:

Grain size measurements were performed by Moya L. Macdonald. Matthew Marshall assisted in the pre-crushing (rock splitter and jaw crusher) of some of the rock material.

5.2 Introduction

Subglacial habitats can remain isolated from external environments for extensive periods of time (thousands of years), with the exception of main drainage channels of glaciers and margins of larger ice masses (e.g. GrIS), which can be partly replenished during the melt season where surface meltwaters have access to the bed (e.g. section 3.7.2.2). For the most part, subglacial communities must therefore rely on carbon and energy sources overlaid during the onset of glaciation for sustenance. As such, the amount of bioavailable substrate beneath the ice dictates the proliferation and activity of subglacial microorganisms.

A "traditional" view of subglacial habitats tightly links the bioavailability of subglacial energy sources (e.g. subglacial organic carbon; SOC) to the age of the overlying ice (i.e. residence time),

with an overall decrease in the quantities of bioavailable material with increasing residence time (e.g. Wadham et al. 2008). A possible consequence in more isolated, remote sections of ice-sheet beds is therefore slower microbial growth and activity, relying on the slow fermentation of decreasingly labile organic matter, chemolithotrophy from decreasingly energetic substrates (Wadham et al., 2008; Boetius et al., 2015), and perhaps necrolytic lifestyle akin to sustain low-energy communities in deep-sea sediments over geological time-scales (Bradley et al., 2018).

Earlier work, however, overlooked potentially bioavailable energy sources generated during rock comminution. Regions of glacier and ice-sheet beds experiencing high physical erosion rates may in fact serve as energetic hotspots in sustaining subglacial life, even providing "renewable" forms of energy over glaciation timescales. Grinding and comminution of subglacial bedrock and tills by overlaying ice flow generates fine-grain particles (flour); this mechanical weathering process is considered to liberate large levels of both macronutrients (e.g. nitrogen and phosphorus) and micronutrients (e.g. iron) (Hawkings et al., 2014; Hawkings et al., 2016; Wadham et al., 2016), but also organic carbon from bedrock and overridden paleosols (Bhatia et al., 2013; Lawson et al., 2014). Incubation experiments using glacial meltwaters of Norwegian glaciers indicated that nitrate (NO_3^-) and small organics (acetate and formate) released from crushed bedrock material are being utilised by indigenous subglacial microbial communities (Kivimaki, 2005).

Telling et al. (2015) further highlighted the potential of (bed)rock comminution as a microbial fuel to subglacial ecosystems. The authors showed that wetting of freshly ground (bed)rock material generates significant amounts of hydrogen gas (H_2) at ~ 0°C, most likely as a result of rock-water reactions with freshly exposed free radicals from crushed silicate minerals. Recent work from dry crushing experiments on different glacial bedrock material also indicated that the crushing process itself releases potentially bioavailable gases (e.g. H_2, CH_4, CO_2, and CO), further highlighting the biological relevance of bed comminution through ice motion (Macdonald et al., 2018). Lastly, it is hypothesised that ice grinding of subglacial sediments, and concomitant geochemical reactions resulting from the grinding process (e.g. H_2O_2 generation), may also "reactivate" refractive organic matter into a more labile component, increasing the bioavailability of older SOC beneath the ice (Tranter, 2015).

Here, we attempt at empirically testing whether concomitant releases of nutrients and energy (e.g. H_2) by rock comminution can be metabolized by, and promote the activity of, microbial communities indigenous to the bed of the Greenland Ice Sheet. In turn, we also investigate

whether a potential increase in (or prolonged) microbial activity will directly impact on the degree of biogeochemical weathering (directly or indirectly) resulting from energy supplied during primary mechanochemical weathering. Previous incubation studies have indeed demonstrated the impact of microbial activity in promoting subglacial weathering (e.g. dissolution) reactions, but did not constrain the influence of glacial flour on these weathering processes (Kivimaki, 2005; Montross et al., 2013b). Similar to previous incubation studies, experiments here were carried out under anoxic conditions believed to be more analogous to remote and isolated sections of ice-sheet beds, and under oxic conditions, conditions found when oxygenated supraglacial waters come into contact with the bed during seasonal growth of subglacial drainage systems and efficient flow, and at the sediment-ice interface, where basal melt can deliver oxygen to the underlying sediments.

5.3 Methods

5.3.1 Sample site and sampling description

Samples consisted of basal ice, meltwaters, and proglacial rock debris from the Leverett Glacier (LG) in Southwest Greenland. See section 3.7.1.1 for site description. Basal ice was collected by chainsaw in August 2009 inside a shallow ice cave on the eastern side of the LG, and kept frozen (< -20°C) until processing; sample collection is described in Lawson et al. (2014) and Nixon et al. (2016).

Most of the rocks used in the comminution experiment were collected on the banks of the LG proglacial river in October 2015. A small number of rocks recovered during melting of basal ice samples (Fig. 1) was also used. The same batch of unprocessed (pre-crushed) rocks were also used and described by Macdonald et al. (2018), and mostly consisted of Precambrian orthogneiss and granite, with quartz, feldspar, and pyroxene accessory minerals - see Table 1 in Macdonald et al. (2018).

5.3.2 Melting of basal Leverett basal ice

Unless stated otherwise, all instrument and containers were sterilised by autoclaving prior to manipulation. All blue chloro-butyl septum stoppers (Bellco, USA) used were previously boiled for 1 hour in 0.1 M NaOH in order to remove any trace volatile contaminants prior to cleaning and autoclaving (Kiene et al., 1986).

LG basal ice was first subsampled using sterile chisel and hammer inside a laminar flow hood. Approximately 1 cm of the outer surface of basal ice sub-samples was melted using autoclaved deionised 18.2 MΩ cm^{-1} (MQ) water in order to remove any potential contaminants. The remainder of the ice block was transferred into a sterile beaker and thawed at room temperature inside an anaerobic chamber containing a N_2 gas atmosphere.

Melted basal waters (~ 2 L) were subsequently transferred into pre-autoclaved Duran bottles and capped with specially-designed, custom made, gas-tight plugs (see Fig. 1). Thawed basal sediments were transferred into a sterile Whirl-Pak bag (Nasco) and stored inside an anaerobic jar without the addition of an anaerobic catalyst. Both water and sediment samples were stored at ~ 0.1°C until the start of the incubation (~ 8 months).

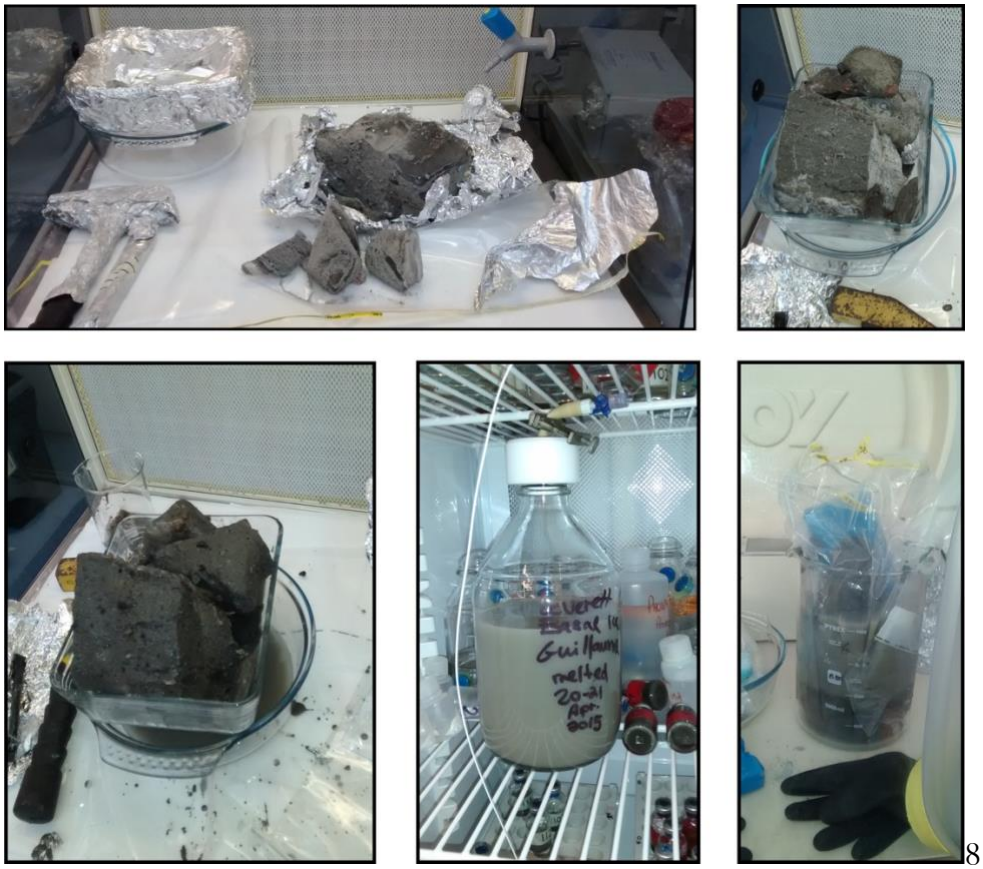

Figure 5.1 Processing of LG basal ice. Shown are basal ice blocks prior, during and after the thawing process inside the laminar flow hood and anaerobic chamber. Also shown is the thawed basal ice inside a Duran bottle capped with specially-designed air-tight plug.

5.3.3 Rock crushing

Prior to milling, rock samples were first reduced in size using a rock splitter, hammer, and subsequently a mechanical "jaw crusher", all pre-cleaned with 100% ethanol. Crushed material was subsequently sieved and pebbles sized between 0.25 – 2 mm were used for milling. In order to remove organic contaminants from surfaces, rocks were then immersed in 30% H_2O_2 for 30 minutes, thoroughly rinsed for 30 minutes with MQ water, soaked overnight and subsequently rinsed again in MQ water. Washed rocks were then autoclaved, and finally dried at 105°C for 2 days.

Pre-treated rocks were ground in a gas-tight zirconium bowl using a Fritsch Planetary Mono Mill Pulverisette 6 at 500 rpm for 30 minutes. The zirconium bowl and balls were sterilised by autoclaving; the rubber seal and grinding lid were sterilised using 70% ethanol in order to prevent potential structural damage from autoclaving. 30 grams of rock material was used during each grinding sessions; the grinding bowl was first flushed with argon gas (grade 5.0) for at least 5 minutes prior to grinding. Post grinding, the zirconium bowl was opened inside an anaerobic chamber containing a N_2 atmosphere and crushed minerals were transferred into sterile serum vials covered with aluminium foil, and capped with 2 cm-thick blue butyl septa. The headspace of the serum vials was then flushed with argon gas (grade 5.0) for at least 2 minutes. Crushed rocks (flour) were stored at room temperature inside serum vials until incubation set-up (~ 2 months).

The flour grain size distribution was measured using a Malvern Mastersizer 3000 as per Macdonald et al. (2018) (Figure 5.2).

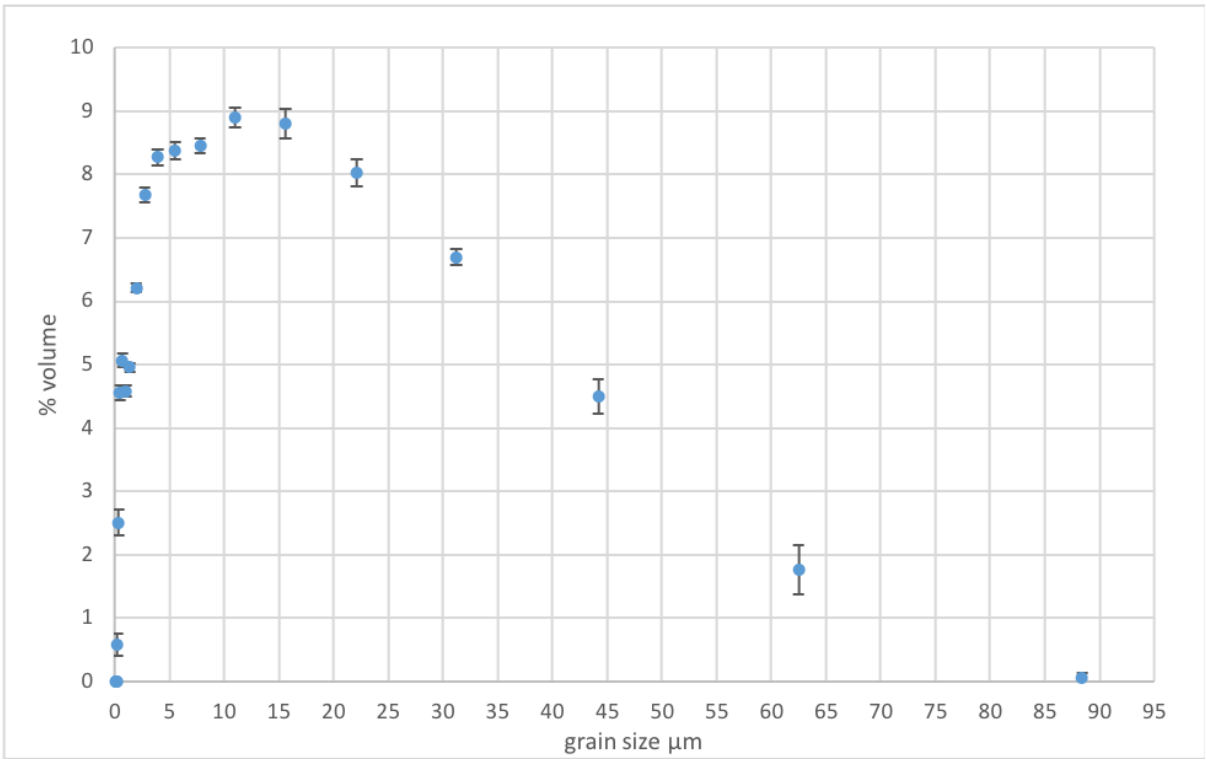

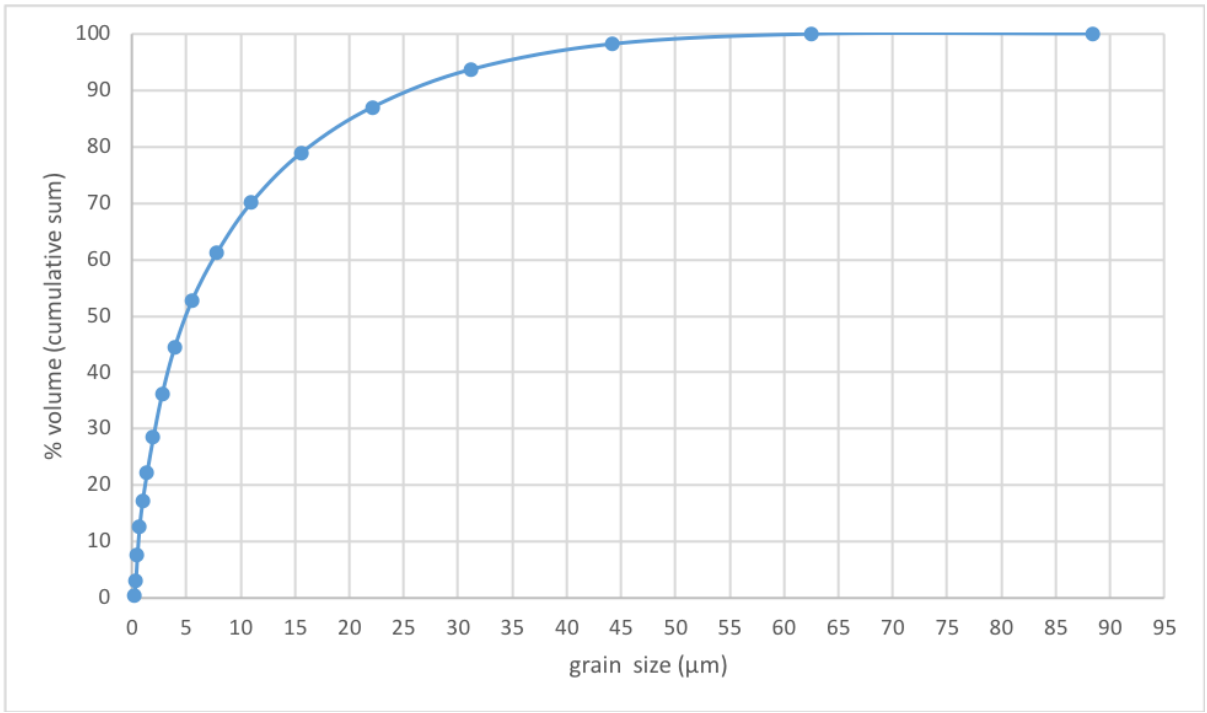

Figure 5.2 Mean grain size distribution of LG rock flour after milling. Top – mean size distribution. Error bars correspond to the standard deviation of triplicate measurements. Bottom – Cumulative mean size distribution.

5.3.4 Set-up of incubation vials

Unless stated otherwise, all glassware used in the incubation experiment was acid washed, thoroughly rinsed (at least 24 hour MQ soak followed by 6 x rinse) and furnaced.

Incubations consisted of basal sediment in slurries incubated with or without crushed rocks (flour), as well as rock flour incubated in MQ water only. Slurries consisted in a mixture of melted LG basal ice (~ 2L; Fig. 1) combined with LG proglacial runoff (~ 1L) aseptically collected on July 01 2015 (see section 5.3.1) and subsequently stored at 4°C (~7.5 months); suspended sediment concentration of LG runoff approximated 1 g L^{-1} (see Fig. 3.1). Incubations were set-up inside 30 mL serum vials (total volume ~ 37.5 mL) capped with 2 cm thick blue butyl stoppers.

Vials were either incubated under oxic (air headspace) or anoxic (N_2 headspace) conditions. Killed controls consisted of autoclaved samples; abiotic controls consisting of only rock flour and MQ water were also set-up. Each vial was amended with 15 mL of slurry or MQ waters, basal sediment (7.2 g ± 1.2 g mean and standard deviation amongst all sample, wet weight) and/or rock flour (4.7 g ± 0.4 g mean standard deviation, dry weight). All treatments were set-up in triplicates with enough vials for five "sacrifice" sampling points (i.e. 15 vials per treatment).

Vials incubated under oxic conditions were set-up inside a pre-sterilised laminar flow hood and anoxic samples were set-up inside an anaerobic chamber. Two days prior to incubation set-up, the anaerobic chamber was sterilised using 3% H_2O_2 and wiped dry; extra moisture was removed using silica desiccant. The chamber was flushed and evacuated four times using nitrogen gas (grade 4.8) following sterilisation and an additional evacuation N_2-flushing cycle was performed on the day of setting-up anaerobic incubations.

Prior to set-up incubation vials inside the anaerobic chamber, LG runoff water was first bubbled with N_2 gas (grade 4.8) at 0°C for 2.5 hours, then transported inside the anaerobic chamber, and LG runoff and basal melt waters were pooled inside a pre-autoclaved 5 L glass flask, and kept cool using freezer packs. The slurry was continuously mixed inside the anaerobic chamber using a magnetic stir rod. Serum vials containing previously crushed rock material (see previous "Rock-crushing" section) to be used in incubation were opened inside the anaerobic chamber, and first

homogenised inside a single Whirl-Pak (Nasco) bag prior to introduction to the incubation serum vials.

Wet melted basal sediments were transferred to 30 mL serum vials to be used for incubation, kept cool with freezer packs. 15 mL of LG slurry was then added to the inoculated vials using a sterile 60 mL plastic syringe. Vials consisting of killed controls were then capped with grey butyl rubber stoppers and autoclaved for 30 minutes with caps on. Following autoclaving, killed control vials were cooled to 4°C and returned to the anaerobic chamber. Abiotic controls consisted in vials containing only rock flour (4.7 g ± 0.4 g mean standard deviation, dry weight) and 15 mL of autoclaved MQ water previously bubbled with N_2 gas and set-up inside the anaerobic chamber. The same amount of rock flour was also added to a set of both live and killed basal sediment slurries. Following the addition of crushed rocks to both sediment slurry and MQ-only samples, vials were quickly capped with 2 cm-thick blue rubber stoppers; the vials' internal pressure was equilibrated to ambient pressure by quickly piercing the blue septa with a needle inside the anaerobic chamber. Vials subjected to oxic incubations were set-up as per inside the anaerobic chamber, but inside a laminar flow hood.

All vials were incubated at ~ 0.1°C. During the first month of incubation, vials were continuously shaken on a rotary shaker in order to homogenise slurries and increase availability of poorly soluble species (e.g. H_2) to microbial populations. Subsequently, vials were kept stationary and manually shaken for approximately 1 minute twice a week during the following 4 months, and once a month for the remaining of the incubation period.

N.B. No reducing agent were employed to avoid the introduction of external agents. However, some levels of oxygen remained in samples incubated under a nitrogen atmosphere (see Fig. 5.3, 5.8, 5.13); despite the trace levels of oxygen present in vials incubated under a nitrogen atmosphere, the term "anoxic" is still employed throughout the text when describing such incubation sets, for simplicity.

5.3.4 Sampling procedure:

5.3.4.1 Gas chromatography and calculation of gas concentrations

Sampling for gas and water chemistry analyses were performed sequentially. Vials were first shaken for at least 30 seconds to equilibrate headspace and dissolved gas concentrations.

Headspace samples were collected using a 5 mL gastight glass syringe (pre-flushed with argon gas) by first injecting 5 mL (at room temperature and pressure) of argon gas to the vial headspace in order to avoid creating negative pressure during sampling. Headspace gas composition was analysed on an Agilent 7980A gas chromatograph equipped with a 1 mL valve-injection loop, fitted with a Porapak Q 80-100 mesh, 2.5 m X 2.0 mm SS column, methanizer (at 395°C) and flame ionization detector (at 300°C) for CO_2 and CH_4, as well as a Haysep D 80–100 mesh, 2m X 1/8-inch SS column and a thermal conductivity detector (at 250°C) for H_2 and O_2. Limits of detection for H_2, CO_2, and CH_4, respectively were 2.0, 0.3, and 0.2 ppmv (of headspace), as reported in Macdonald et al. (2018).

Headspace concentrations in ppmv for CH_4 and H_2 were converted to molar concentrations using the ideal gas law:

$$n = \frac{pV}{RT}$$

Where n is the amount of gas in nmol, p the partial pressure of the gas in ppmv, V the headspace volume of the vial in mL, R the ideal gas constant (0.0821 L atm K^{-1} mol^{-1}) and T the temperature of gas in Kelvin during injection.

Dissolved gas concentrations were calculated using Bunsen coefficients (β) calculated using equation 1 and Table 1 from Wiesenburg and Guinasso Jr (1979), converted to modified Henry's law constants (H') using the ideal gas law above; a salinity of "0" (i.e. freshwater) was assumed when calculating Bunsen coefficients:

$$\beta = e^{A_1 + A_2\left(\frac{100}{T}\right) + A_3 \ln\left(\frac{T}{100}\right)}$$

Where β is defined as the volume of gas (mL) dissolved in 1 mL of water at 0°C and 1 atm. $A_{1\text{-}3}$ refer to constants in table 1 of Wiesenburg and Guinasso Jr (1979) and T the injection temperature in Kelvin.

$$H' = \frac{\beta}{RT} \times 1000$$

Where H' is the modified Henry's constant in nmol L^{-1} μatm^{-1}, β is the Bunsen coefficient calculated above, R the ideal gas constant above, and T is 0°C in Kelvin (i.e. 273.15). Dissolved gas concentrations (nM) were then calculated from the product of gas headspace concentrations in ppmv and H'.

Reported molar amounts for CH_4 and H_2 correspond to the total amount of gases per vial (i.e. dissolved plus headspace phases); CO_2 and O_2 concentrations correspond to headspace concentrations only, in volume fraction (ppmv or %v).

5.3.4.2 Sampling and analyses of liquid phase

Following sampling of vials' headspace, vials were again shaken to homogenise the sediment-flour slurry, septa removed, and the slurry quickly transferred into a clean (sterile and new) 50 mL polypropylene centrifuge tube (Fisherbrand™). Tubes were centrifuged at 4500 x g for 3 minutes and the supernatant decanted into a new 50 mL centrifuge tube. The supernatant was subsequently filtered using a sterile10 mL syringe equipped with a 0.22 µm polyethersulfone (PES) filter (Millex-GP) and sequentially dispensed into acid-washed polyethylene bottles, for silica analyses, and clean (sterile and new) 2 mL polypropylene tubes (Simport™ Scientific) for major ion and small organic acid analyses. Samples for small organic acid (acetate and formate) analysis were frozen and those intended for silica and major ion analyses were refrigerated until analyses.

Due to high solute concentrations, samples were diluted 10 fold before analysis. Dissolved silica concentrations were measured spectrophotometrically using Flow Injection Analysis (FIA) on a LaChat8500 series (QuikChem Method 31-114-27-1-D) as per Hatton et al. (2019). Major ions (Na^+, K^+, Ca^{2+}, Mg^{2+}, NH_4^+, Fl^-, Cl^-, NO_3^-, SO_4^{2-}, and PO_4^{3-}) were measured using a ThermThermo Scientific™ Dionex™ capillary ICS-5000, fitted with anion and cation columns, as per Hawkings et al. (2015). Acetate ($C_2H_3O_2^-$), formate (HCO_2^-), and butyrate ($C_4H_7O_2^-$) were measured on the same machine. Butyrate levels were below detection limit in all analysed samples and therefore are not further reported. Alkalinity (as HCO_3^-) was estimated by charge deficit, as per Hawkings et al. (2015).

5.4 Results

5.4.1 Incubations with crushed rocks only

5.4.1.1 Gas release and consumption from rock flour

The levels of hydrogen gas (H_2) generated by rock crushing (~ 8-10 nmol g^{-1}) under anoxic conditions were comparable to those previously observed by Telling et al. (2015) for the same rock type (i.e. Leverett gneiss) (Fig. 5.3). Oxic incubations also led to the generation of H_2 from crushed rocks, although at a slower release rate and to a lower total level (up to ~ 6.25 nmol g^{-1} after ~ 365 days of incubation; Fig. 5.3). In addition to H_2, small levels of CH_4 were also released from crushed mineral throughout the incubation period (~ up to 0.25 nmol g^{-1}). Rock flour acted as a sink of both O_2 and CO_2. Rates and levels of abiotic CO_2 consumption, likely caused by carbonation reactions on freshly exposed mineral surfaces, were highly similar in both oxic and anoxic sets of incubations (Fig. 5.3). Similarly, decreases in O_2 levels likely resulted from the oxidation of free radicals (consistent with the lower levels of H_2 generated in oxic samples) on freshly exposed reactive mineral surfaces generated during the crushing process, as well as from sulphide oxidation (see below). It should be noted that some levels of O_2 was detectable through the first 100 days of incubations in the "anoxic" set of incubations, and therefore that reducing conditions were likely not prevailing in the flour slurry for most of the incubation period, except potentially as microenvironments (Fig. 5.3).

5.4.1.2 Nutrients, dissolved silica and small organic acids

Rock flour liberated both inorganic nutrients (nitrogen, phosphorus, and sulphur) as well as small organic molecules. Detected nitrogen species consisted of nitrate (NO_3^-; up to ~ 0.04 µmol g^{-1}), as well as trace amounts of ammonium (NH_4^+; < 0.002 µmol g^{-1}) (Fig. 5.4). Phosphate (PO_4^{3-}) was also liberated in flour incubations under both oxic and anoxic conditions, but mostly only after >100 days of incubation, with higher concentrations in oxic samples (Fig. 5.4). Crushing also liberated moderate amounts of dissolved silica (Si; up to ~ 0.6 µmol g^{-1}) (Fig. 5.4). In addition to inorganic nutrients, crushing of rock material liberated appreciable amounts of acetate (up to ~ 0.45 µmol g^{-1}) and formate (up to ~ 0.25 µmol g^{-1}) (Fig. 5.5). The levels of nutrient released observed here are consistent with a previous short-term wetting experiment on crushed LG mineral which also detected similar concentrations of NO_3^-, but no PO_4^{3-} after one week of incubation (Tian, 2014). However, no acetate was detected during this previous crushing

experiment but relatively large levels of dissolved organic carbon (DOC) were reported (up to 600 µM in 10 g of crushed rock per 50 mL of MQ water slurries). The absence of detectable acetate levels in this previous experiment may be explained by the coarser flour used compared to here (mean flour size of ~ 25 µm compared to ~ 11 µm here).

5.4.1.3 Major ions

Sodium (Na^+), potassium (K^+), magnesium (Mg^{2+}), and calcium (Ca^{2+}) were the dominant cations released from crushed rocks in decreasing order, with monovalent cations (Na^+, K^+) concentrations over an order of magnitude greater than divalent (Ca^{2+}, Mg^{2+}) cations (Fig. 5.6). Major anions measured in flour incubations included chloride (Cl^-; up to ~ 1.75 µmol g^{-1}) and fluoride (up to ~ 0.75 µmol g^{-1}); but bicarbonate (HCO_3^-) accounted for the most abundant anion produced by at least an order of magnitude (up to ~ 850 umol g^{-1}) (Fig. 5.7). Sulphate release (likely resulting from abiotic sulphide – e.g. pyrite – oxidation; (Tranter et al., 2002; Wynn et al., 2006)) occurred mostly in oxic samples with continuous release throughout the incubation period (up to ~ 1.4 µmol g^{-1} at the end of the incubation period). A more modest, delayed release of sulphate (up to 0.2 µmol g^{-1} within 335 days) was observed in anoxic samples (Fig. 5.7).

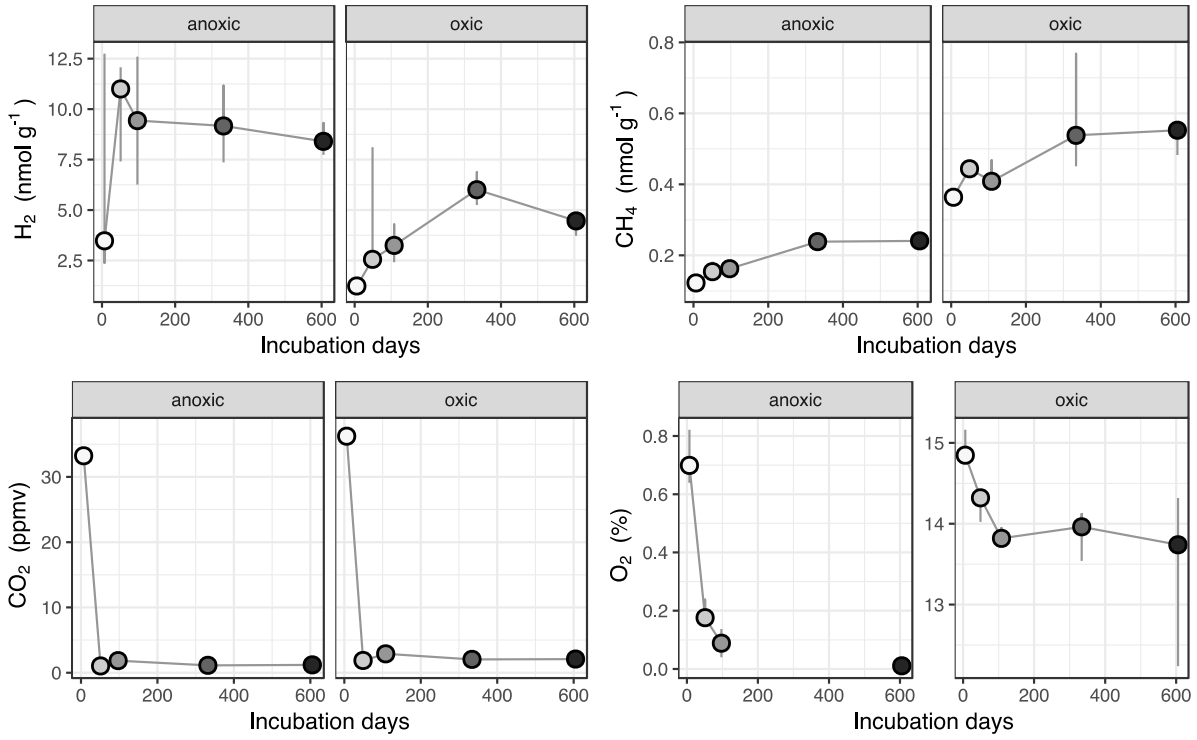

Fig. 5.3 Gases released or consumed from mineral flour incubated in MQ water. The offset in methane levels for the first time point between oxic and anoxic incubations reflects initial air concentrations of methane. H_2 and CH_4 are reported as nmol of gases released per gram of dry flour; CO_2 and O_2 are reported as headspace concentrations (volume:volume). Note the difference in scales of y axes for the O_2 concentrations between the oxic and anoxic incubations. **In all figures, error bars denote minimum and maximum values from triplicates, with dots corresponding to median.**

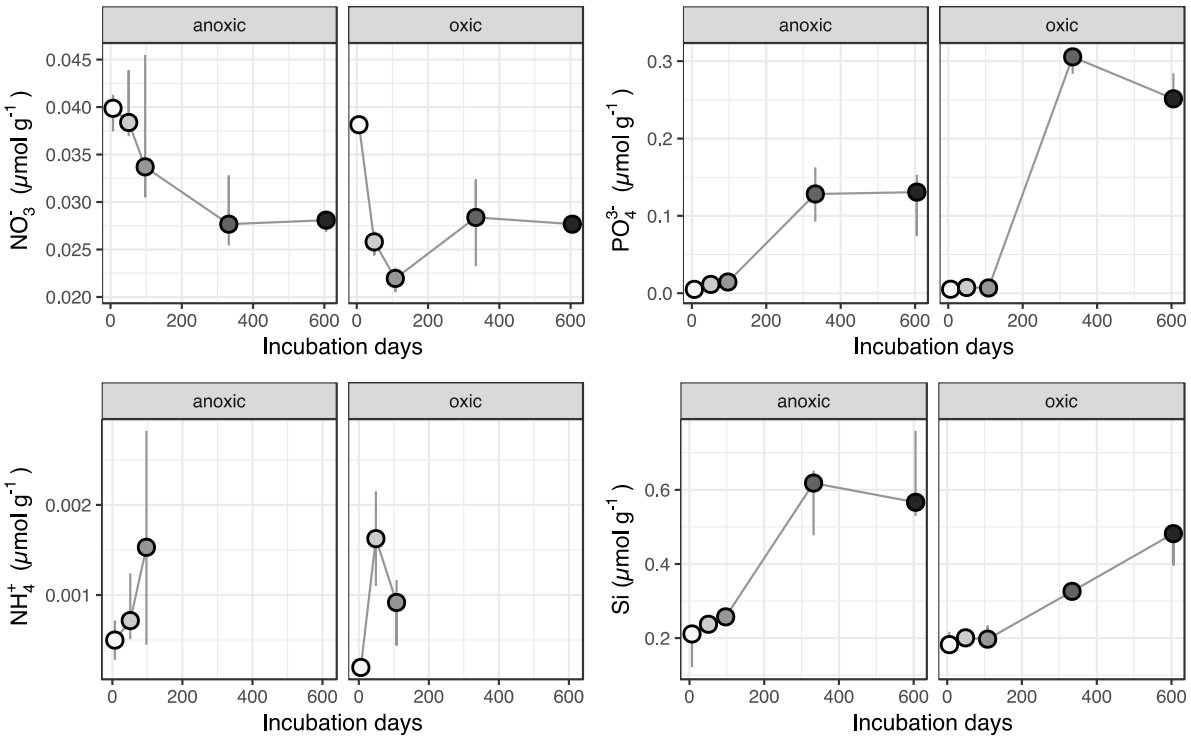

Figure 5.4 Inorganic nutrients and dissolved silica released from crushed rocks incubated in MQ water. NH_4^+ concentrations were only measured for the first 3 time points; analyte levels are reported in µmol per gram of dry flour.

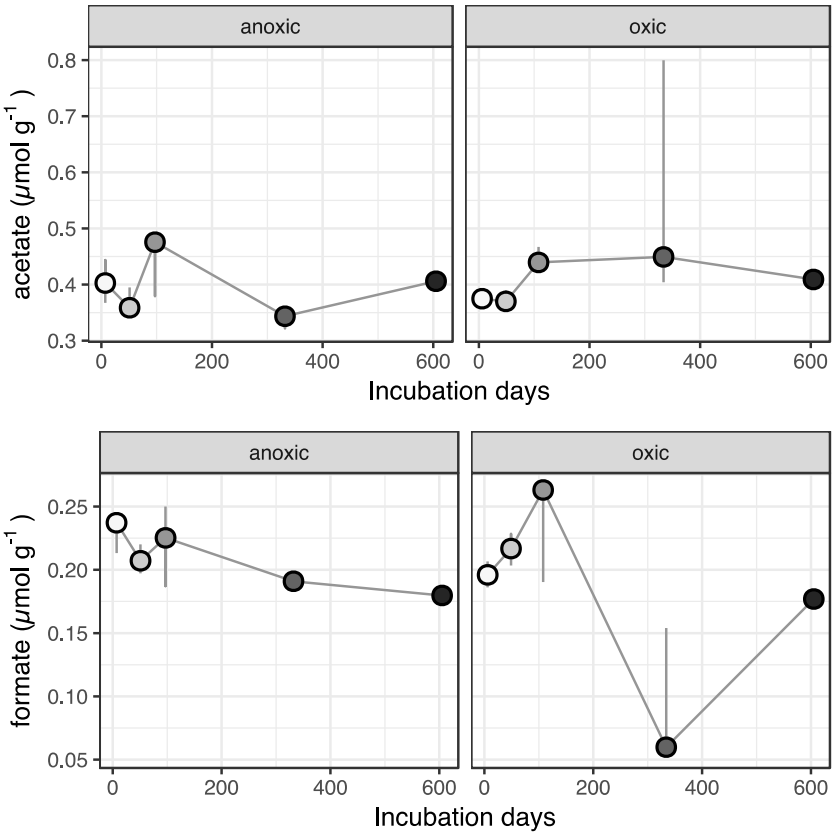

Figure 5.5 Acetate and formate released from crushed rocks incubated in MQ water. Analyte levels are reported in µmol per gram of dry flour.

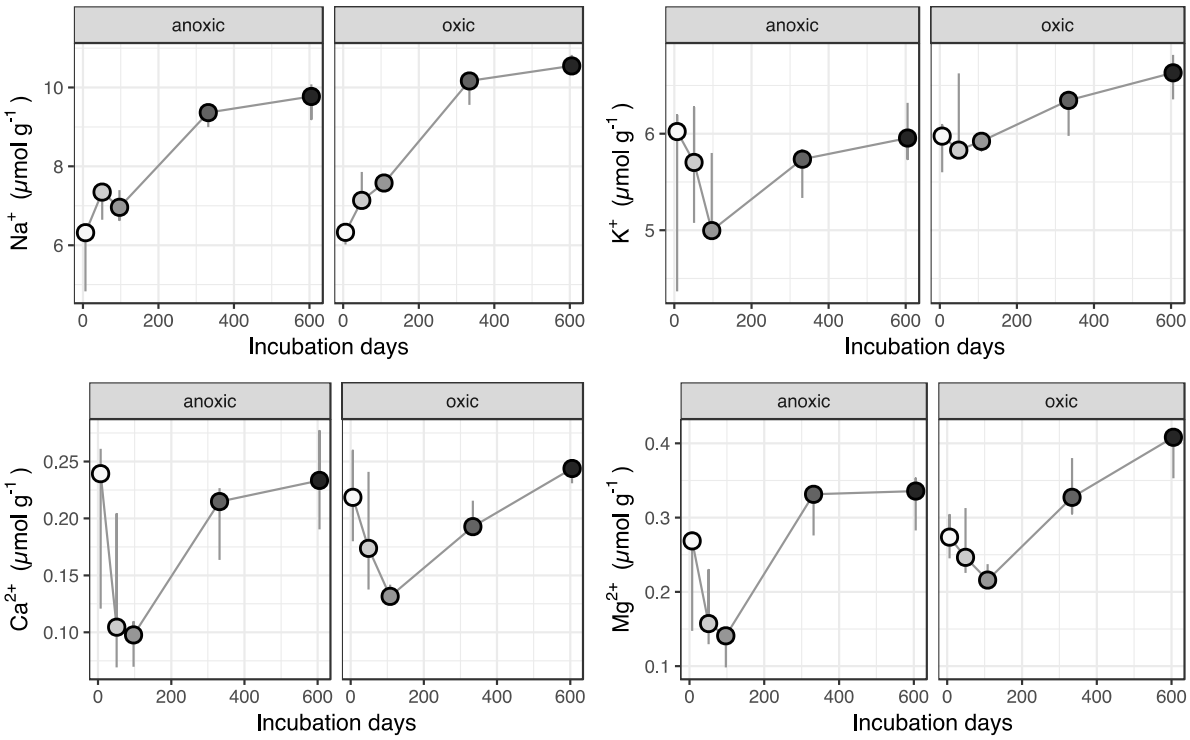

Figure 5.66. Major cations released from crushed rocks incubated in MQ water. Analyte levels are reported in µmol per gram of dry flour.

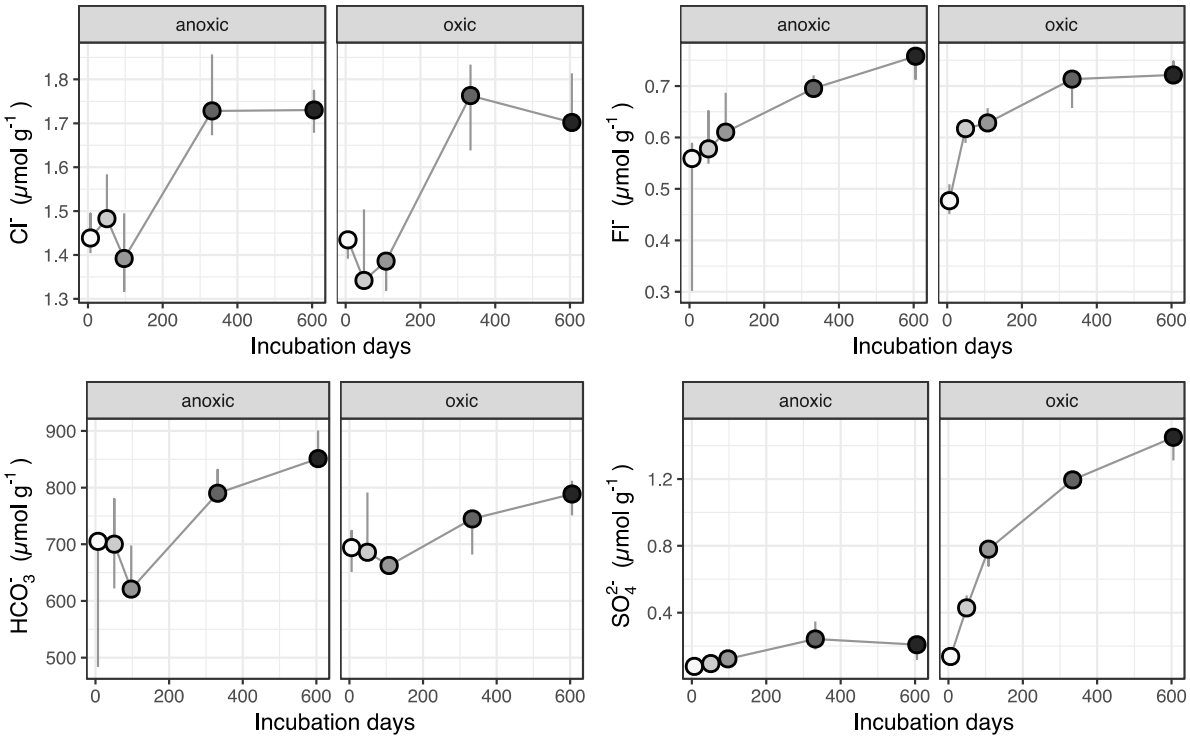

Figure 5.7 Major anions released from crushed rocks. Analyte levels are reported in µmol per gram of dry flour.

5.4.2 Indication of microbial activity (basal sediments only, no flour addition)

Microbial activity was evidenced in basal sediments throughout the incubation period by marked differences between autoclaved and non-autoclaved slurries.

5.4.2.1 Gas release and consumption

Consistent decreases in O_2 concentrations in both air and nitrogen incubated live samples suggests microbial respiration. O_2 concentrations decreased to below detection levels in "anoxic" samples after 100 days of incubation, and down to ~13% of headspace in oxic ones, compared to ~ 0.5% and ~ 16% of headspace for the autoclaved samples incubated under a N_2 and air atmosphere, respectively (Fig. 5.8). As for the incubation containing only crushed rocks (Fig. 5.3), low levels of oxygen remained in samples incubated under a N_2 headspace for most of the incubation period. Oppositely to O_2, relatively large increases in CO_2 concentrations during the second time point (~ 50 days), and elevated CO_2 relative to controls during the rest of the incubation period in live sediment slurries, are indicative of respiration (Fig. 5.8).

Autoclaving resulted in abiotic release of hydrogen, and to a lesser extent methane, and killed controls therefore do not serve as reliable reference points for background concentrations (Fig. 8, red lines). However, apparent H_2 production and consumption throughout the incubation period in live samples do suggest microbial activity (Fig. 5.8). The increase in methane concentrations in live samples observed during the last time point (> 600 days) may also result from microbial activity; however, such marked increase was only observed in vials incubated under oxic conditions (Fig. 5.8).

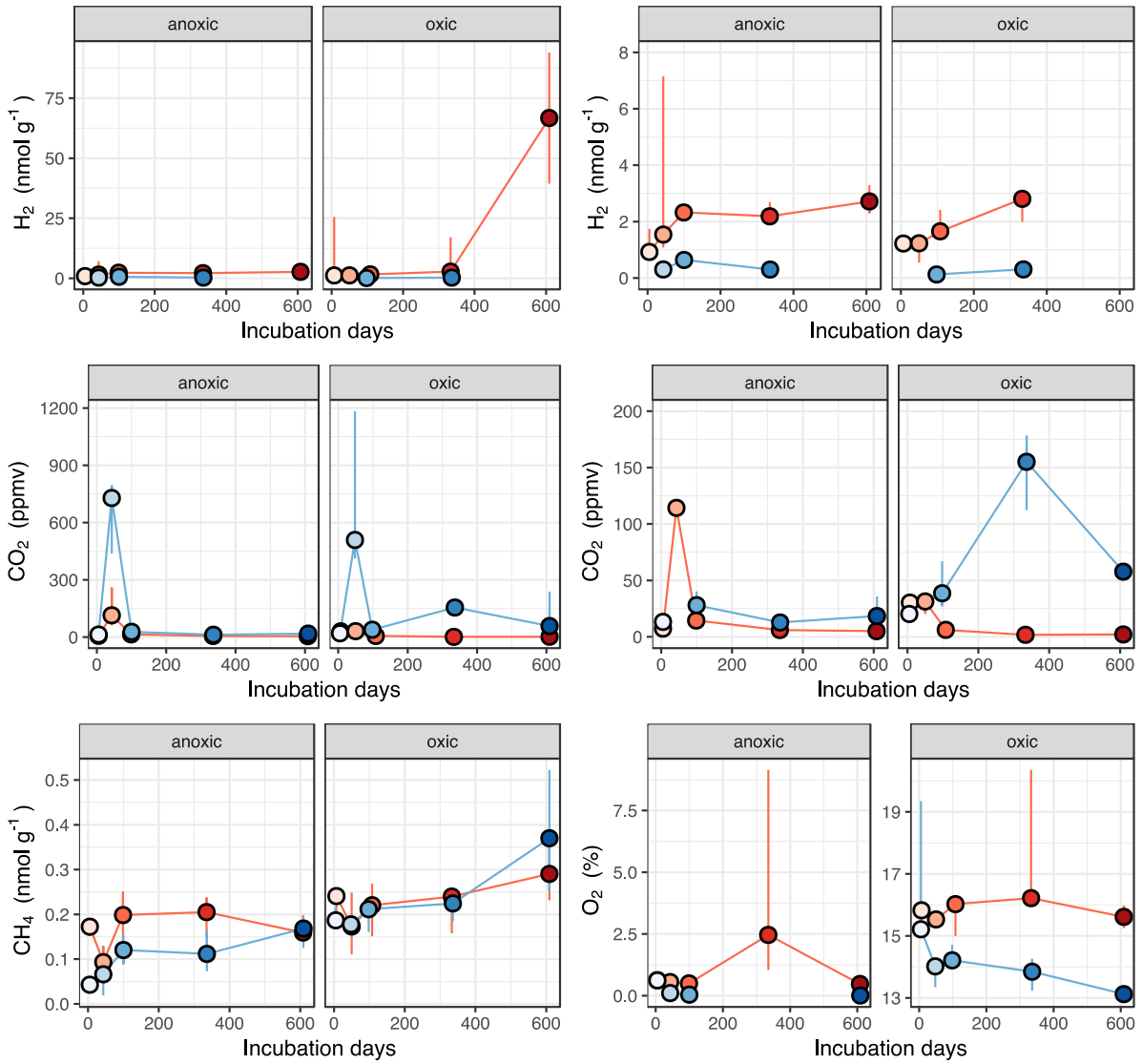

Figure 5.8. Gases released and consumed in basal-sediment slurries incubated without flour. Red and blue series denote autoclaved (kill) and non-autoclaved (live) slurries, respectively. H_2 and CO_2 panels on the right hand side are zoomed in of their corresponding left-hand side panels (the second CO_2 time points for live samples and last H_2 time points for oxic killed samples fall outside of the zoomed panels). Missing points in live H_2 and O_2 correspond to time points when the gases were below detection levels. Note the difference in y axes for the O_2 concentrations between the oxic and anoxic incubations. H_2 and CH_4 levels are reported in nmol of gas present in the vial (dissolved plus gaseous phases) normalised to the mass of wet sediments. CO_2 and O_2 are reported as headspace concentrations (volume:volume). Points denote median, with error bars corresponding to minimum and maximum values of triplicates.

5.4.2.2 Nutrients, dissolved silica and small organic acids

Inorganic nutrients and short organic acids were less abundant in sediment than those released from wetted flours (Fig. 5.4 and 5.9). Increased levels of nitrate in autoclaved sediments relative

to live samples after one week of incubation (first time point) may indicate some abiotic release of nitrates during autoclaving (Fig. 5.9). Autoclaving may also have resulted in release of ammonium, but only under oxic conditions where ammonium levels in autoclaved controls remained ~ 1 order of magnitude higher than live slurries (Fig. 5.9). A nitrate decrease (e.g. denitrification) during the first 100 days of incubation, followed by concentration increases during the end of the incubation period may reflect microbial cycling of N-compounds, or influence thereof (Fig. 5.9). No notable difference in phosphate levels between live and autoclaved slurries was observed throughout the incubation period. Acetate and formate were present in small concentrations (up to < 10 and 25 µM, respectively), with no clear difference in release/consumption levels between kill and live slurries, except for formate consumption in live samples under oxic conditions (Fig. 5.10). Autoclaving likely increased silicate dissolution, and, therefore, autoclaved controls do not serve as reliable background reference points. Dissolved silica concentrations in live samples reached the same levels as controls by the end of the incubation period (Fig. 5.9).

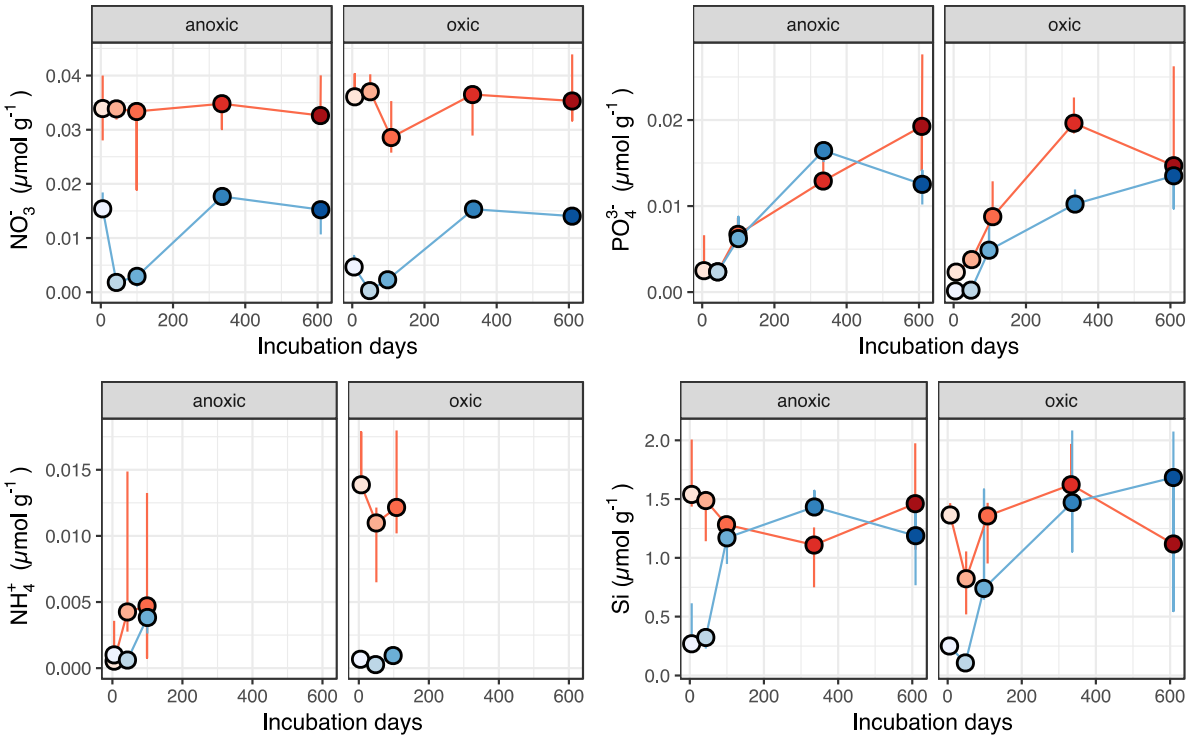

Figure 5.9. Inorganic nutrients and dissolved silica released from basal-sediment slurries incubated without flour. Red and blue series denote autoclaved (kill) and non-autoclaved (live) slurries, respectively. NH_4^+ concentrations were only measured for the first 3 time points; analyte levels are reported in µmol per gram of wet sediment.

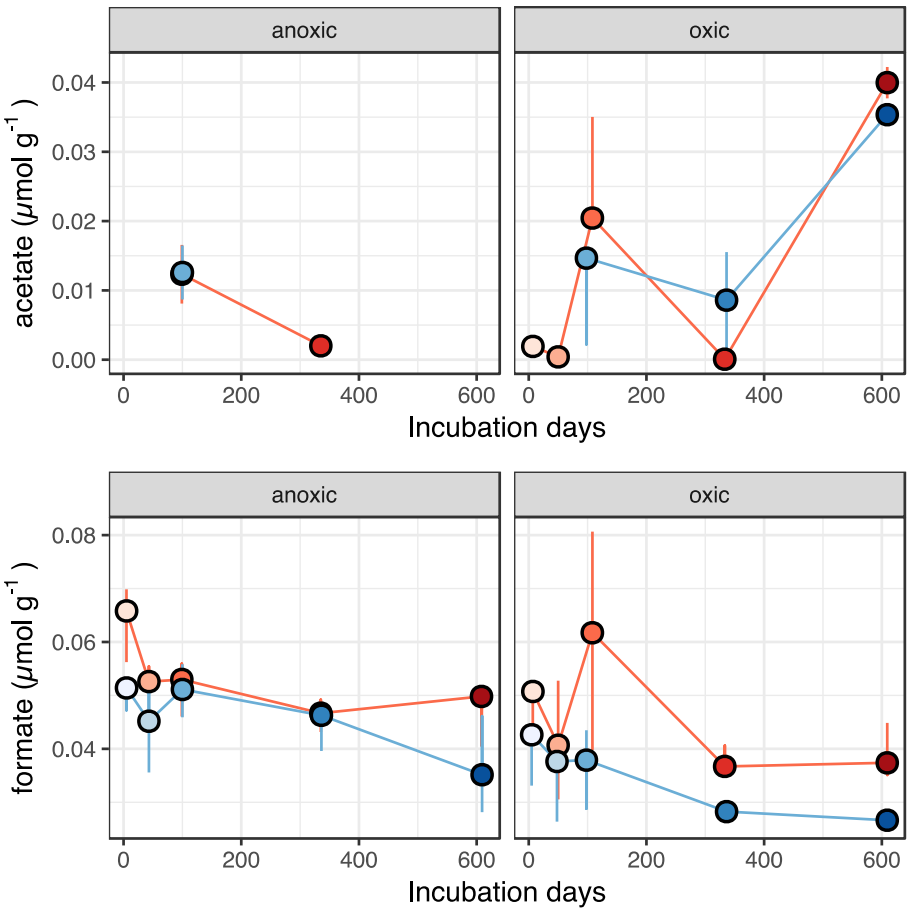

Figure 5.10 Acetate and formate levels in basal-sediment slurries incubated without flour. Red and blue series denote autoclaved (kill) and non-autoclaved (live) slurries, respectively. Analyte levels are reported in µmol per gram of wet sediment.

5.4.2.3 Major ions

Increased mineral dissolution was observed in all live incubations, when compared to autoclaved samples, but only under oxic conditions (Fig. 11-12). Sulphate release (e.g. from pyrite oxidation) was greatly enhanced in the live samples under oxic conditions (Fig. 5.12), indicating microbially catalysed sulphide oxidation was occurring (Tranter et al., 2002; Montross et al., 2013b).

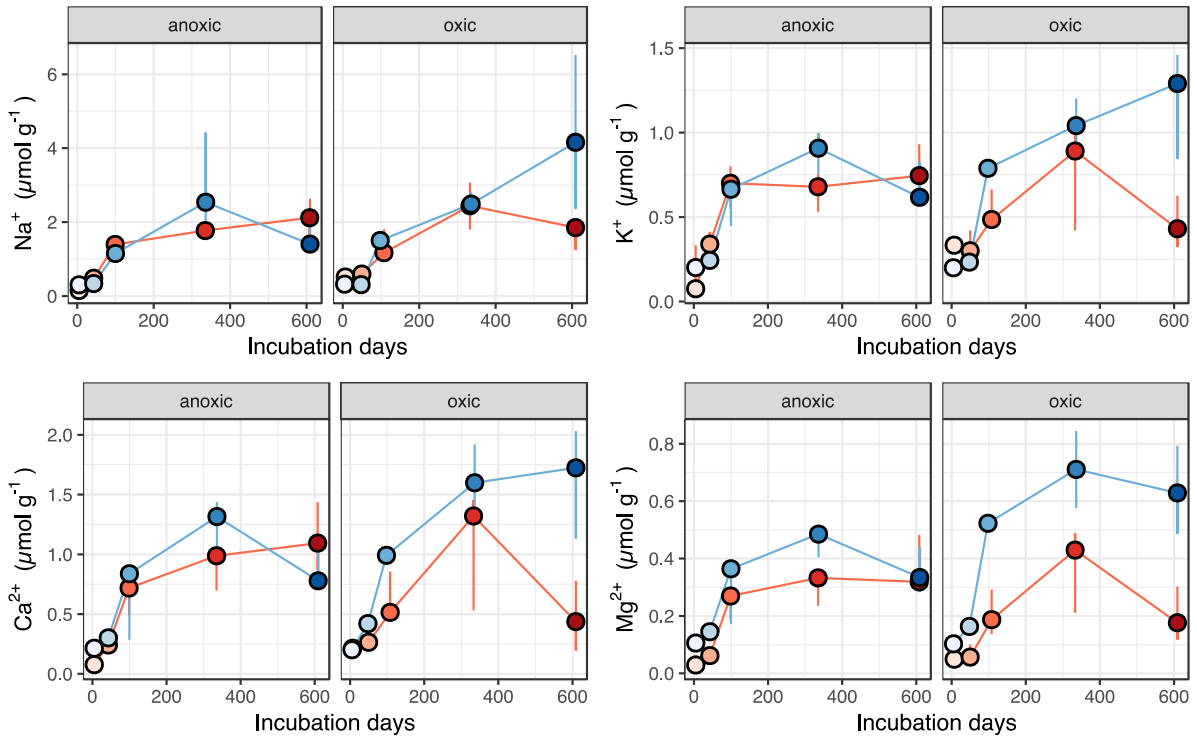

Figure 5.11 Major cations released from basal sediments incubated without flour. Red and blue series denote autoclaved (kill) and non-autoclaved (live) slurries, respectively. Analyte levels are reported in µmol per gram of wet sediment.

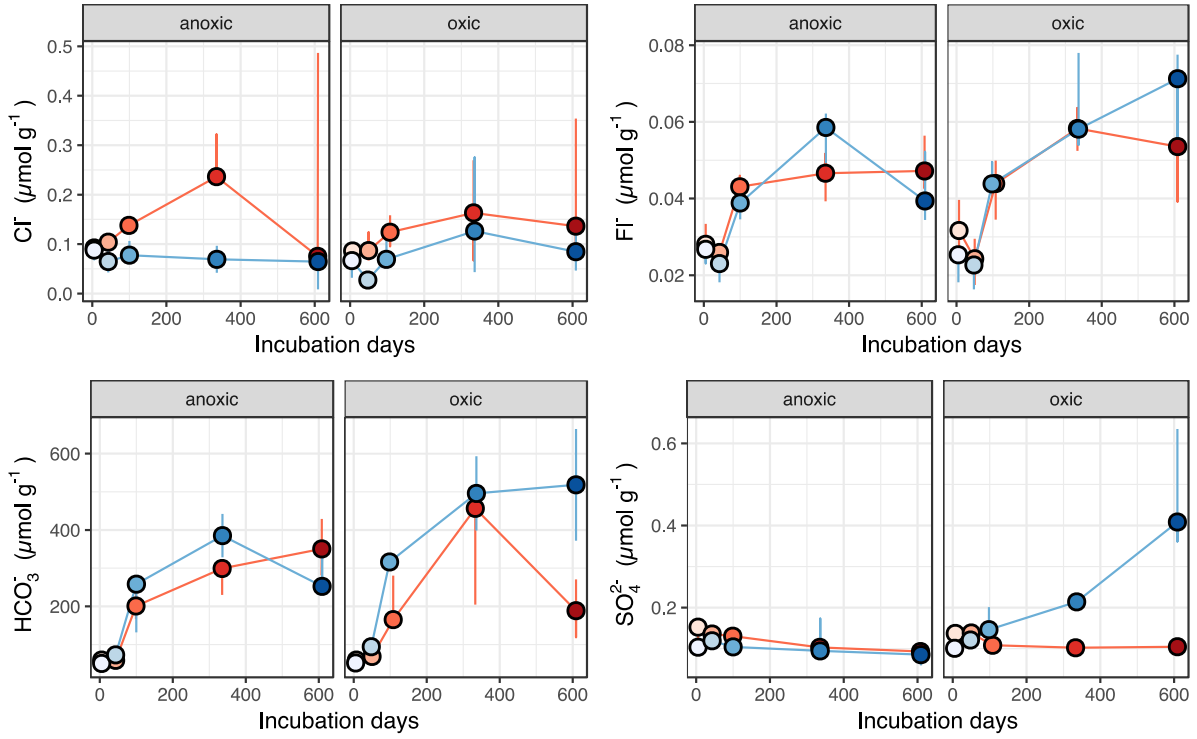

Figure 5.12 Major anions released from basal sediments without flour. Red and blue series denote autoclaved (kill) and non-autoclaved (live) slurries, respectively. Analyte levels are reported in µmol per gram of wet sediment.

5.4.3 Basal-ice incubations amended with rock flour

5.4.3.1 Microbial utilisation of crushed-rock solutes and gases

Levels of H_2 gas detected in live samples incubated with rock flour followed a similar trend than that observed for samples incubated without it; that is, initial release of H_2 during the first 100 days of incubation followed by consumption during the remainder of the incubation period (Fig. 5.13). Interestingly, initial H_2 generation under anoxic conditions by live samples with flour greatly surpassed that from controls (even when accounting for hydrogen released from sediments alone; Fig. 5.13 dashed-grey curve). H_2 concentrations in oxic incubations remained lower than controls for the duration of the incubation, with hydrogen reaching levels below detection at the end of the incubation period, indicative of microbial consumption (Fig. 5.13).

No apparent differences between controls and live slurries were observed regarding methane concentrations. Unlike in unamended basal sediments (Fig. 5.8), no CO_2 spike was observed in flour-amended live slurries at 50 days of incubation; however, a slower decrease in CO_2 concentrations under anoxic conditions during the first 50 days of incubation, as well as elevated (compared to control) CO_2 concentrations under oxic condition after 50 days of incubation did characterise the non-autoclaved (live) sediment slurries amended with rock flour (Fig. 5.13). Similar to incubations without the addition of flour, live slurries containing crushed rocks consumed O_2 at a faster rate, and to a lower level, than autoclaved controls under oxic conditions (Fig. 5.13).

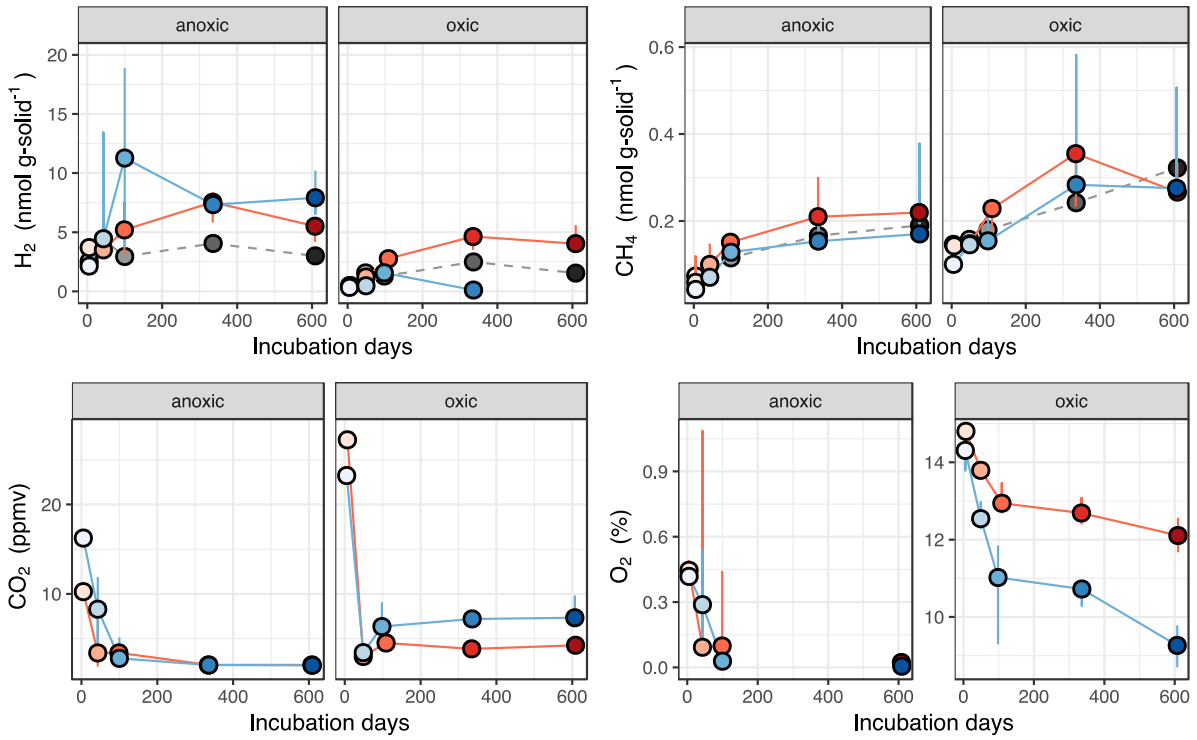

Figure 5.13 Gases released and consumed in basal-sediment slurries incubated with the addition of rock flour. Red and blue series denote autoclaved (kill) and non-autoclaved (live) slurries, respectively. Grey series connected by a dashed line correspond to theoretical "control" levels calculated by adding the mean values obtained for flour-only and live-sediment-only incubations (i.e. mean from fig. 3 and live series of fig. 8). Such theoretical control was only calculated for H_2 and CH_4. Gram of solid corresponds to the added gram of dry rock flour plus wet basal sediments added to each vial. Missing points for H_2 and O_2 correspond to time points when the gases were below detection levels. Note the difference in y axes for the O_2 concentrations between the oxic and anoxic incubations. CO_2 and O_2 are reported as headspace concentrations (volume:volume). Again, points denote median, with error bars corresponding to minimum and maximum values of triplicates (except for the grey points, which only represent theoretical mean values).

5.4.3.2 Nutrients, dissolved silica and small organics

Nitrate liberated from crushed material was quickly consumed in both oxic and anoxic live samples when compared to controls (Fig. 5.14). Unlike for samples incubated without flour, nitrate levels in live incubations with flour exhibited a continuous decrease in concentrations during the first 335 days of incubation (Fig. 5.14). Acetate from rock flour was also quickly consumed during the first 50 days of incubation in both anoxic and oxic samples, followed by some degree of release (Fig. 5.15). As opposed to acetate, formate consumption was mostly apparent in live samples under oxic conditions (Fig. 5.15). Oxic samples also exhibited slower "release" of flour-derived phosphate than controls, likely reflecting microbial consumption; lower levels of phosphates in anoxic treatments with flour and sediments were also detected

relative to abiotic controls but with no apparent difference between live and autoclaved controls (Fig. 5.14). Ammonium levels in live incubations also remained at the same level or lower than controls (Fig. 5.14). A punctual increase in dissolved silica was observed in oxic live incubations with flour but only during the second sampling point (~ 50 days), with silica levels dropping back to control levels during later time points (Fig. 5.14). Note that dissolved silica levels in samples containing flour also never reached concentrations as high as found in samples incubated without flour (Fig. 5.9, 5.14).

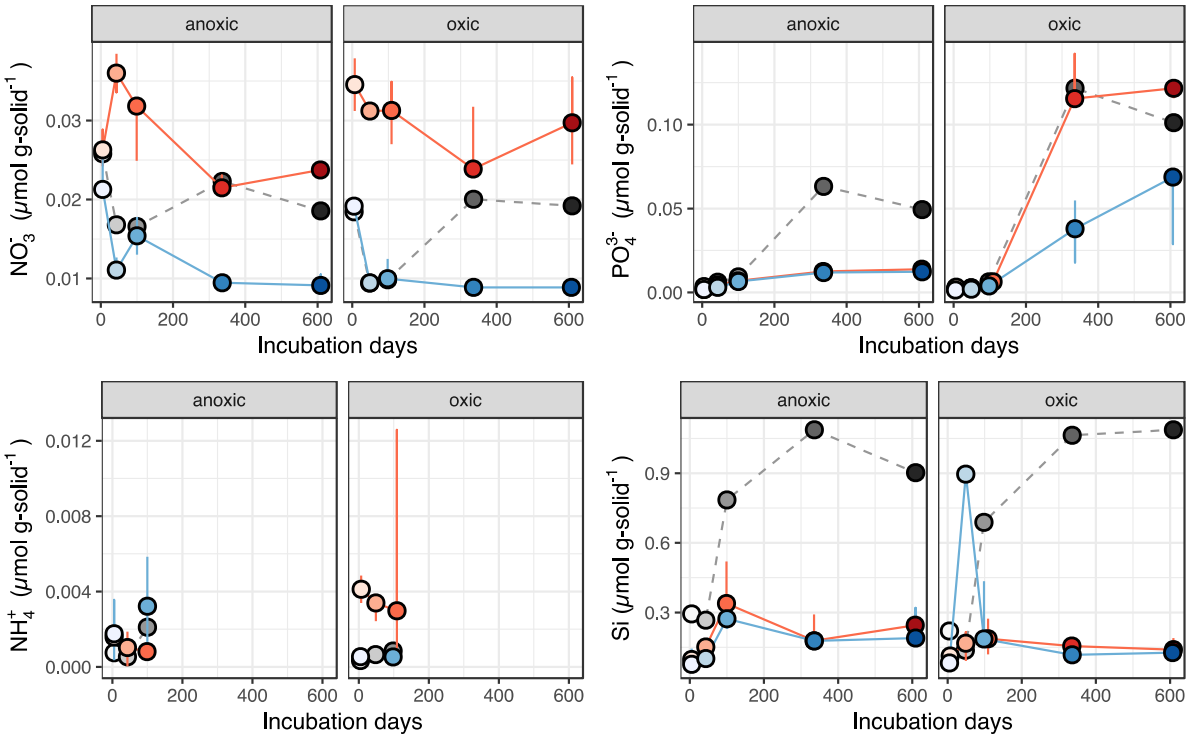

Figure 5.14 Inorganic nutrients and dissolved silica released from basal-sediment slurries incubated with rock flour. Red and blue series denote autoclaved (kill) and non-autoclaved (live) slurries, respectively. Grey series connected by a dashed line correspond to theoretical "control" levels calculated by adding the mean values obtained for flour-only and live-sediment-only incubations. Gram of solid corresponds to the added gram of dry rock flour plus wet basal sediments added to each vial. NH_4^+ concentrations were only measured for the first 3 time points.

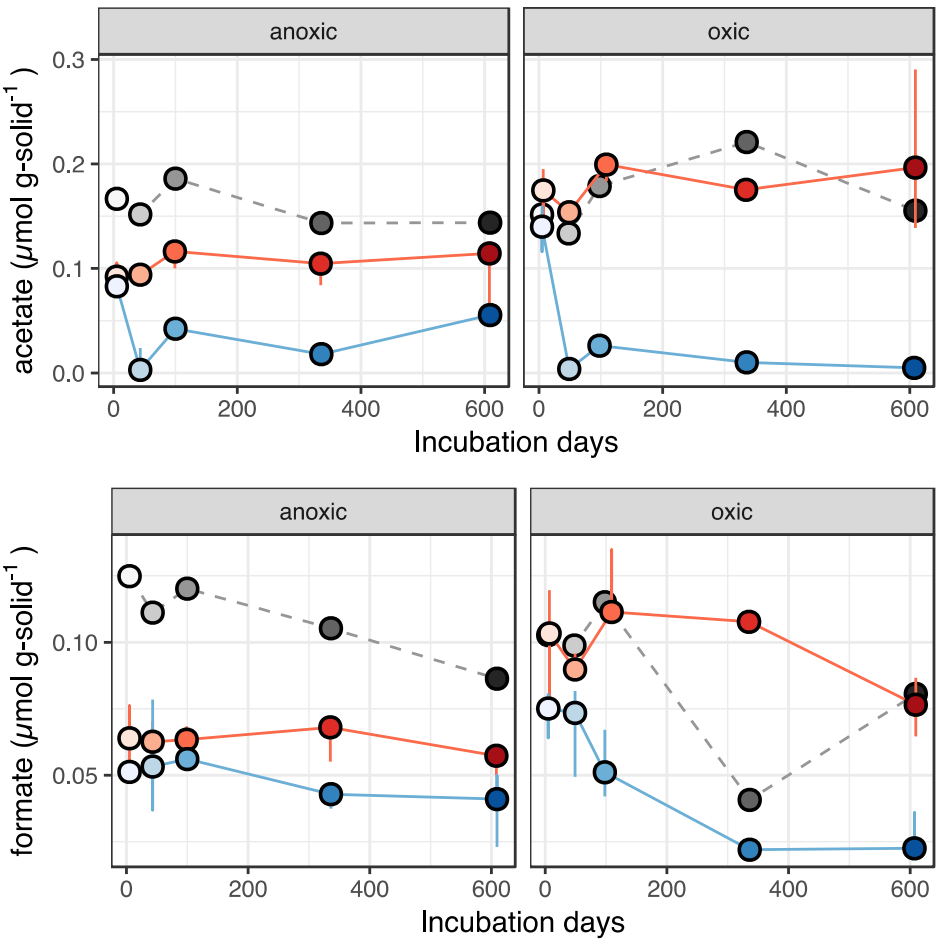

Figure 5.15 Acetate and formate levels in basal-sediment slurries incubated with rock flour. Red and blue series denote autoclaved (kill) and non-autoclaved (live) slurries, respectively. Grey series connected by a dashed line correspond to theoretical "control" levels calculated by adding the mean values obtained for flour-only and live-sediment-only incubations. Gram of solid corresponds to the added gram of dry rock flour plus wet basal sediments added to each vial.

5.4.3.3 Major ions

Unlike for nutrients, organic carbon, and hydrogen, a microbial (biological) imprint on dissolved weathering products was not consistently and clearly apparent for most analytes, with often very little differences between controls and live incubations. Rates of cation dissolution for basal sediments incubated without flour was increased in live samples, mostly in oxic incubations and towards the end (> 300 days) of the incubation period (Fig. 5.11). Rates of cation release during the first 100 days of incubation were also faster in live sediments containing flour, most notably for Na^{+} and Ca^{2+} ions (Fig. 5.16). However, cation levels at the end of the incubation period did not differ amongst treatments, and levels of divalent cations liberated in flour samples remained orders of magnitude less than in those containing only basal sediments (Fig. 5.11, 5.16). Unlike

observed for sulphate release in incubations without flour, no clear microbial effect on sulphate release from incubations with flour was observed.

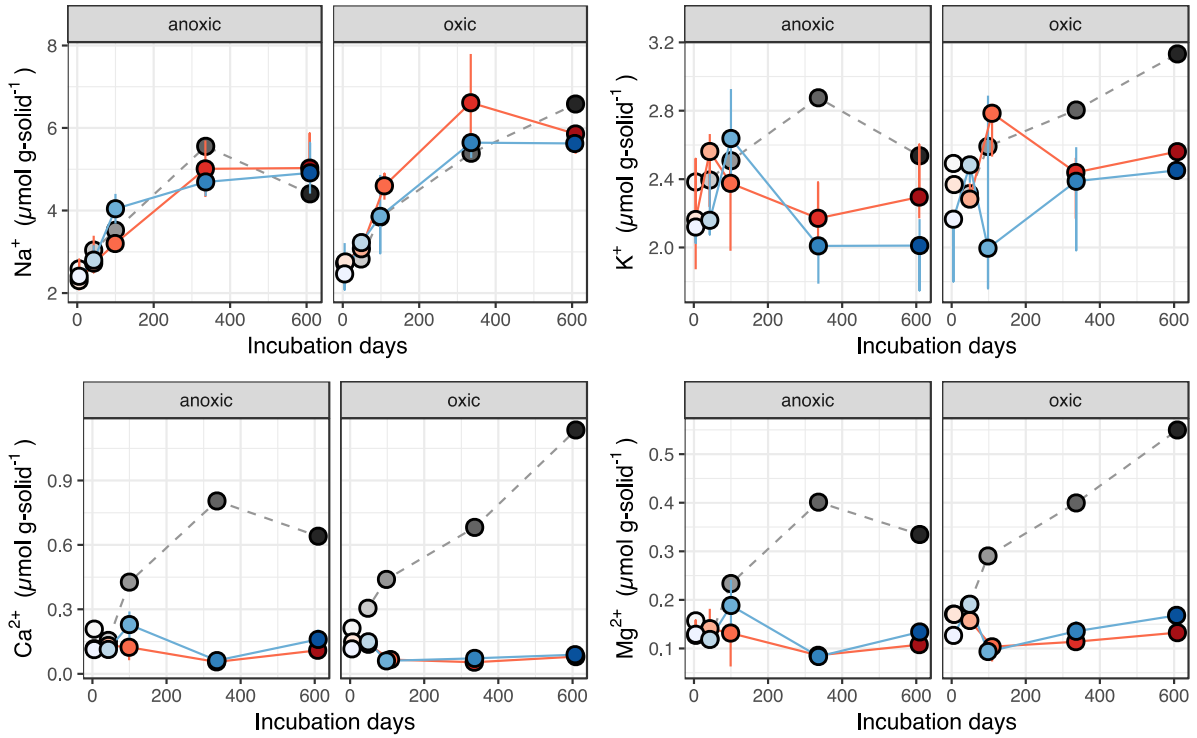

Figure 5.16 Major cations released in basal-sediment slurries incubated with rock flour. Red and blue series denote autoclaved (kill) and non-autoclaved (live) slurries, respectively. Grey series connected by a dashed line correspond to theoretical "control" levels calculated by adding the mean values obtained for flour-only and live-sediment-only incubations. Gram of solid corresponds to the added gram of dry rock flour plus wet basal sediments added to each vial.

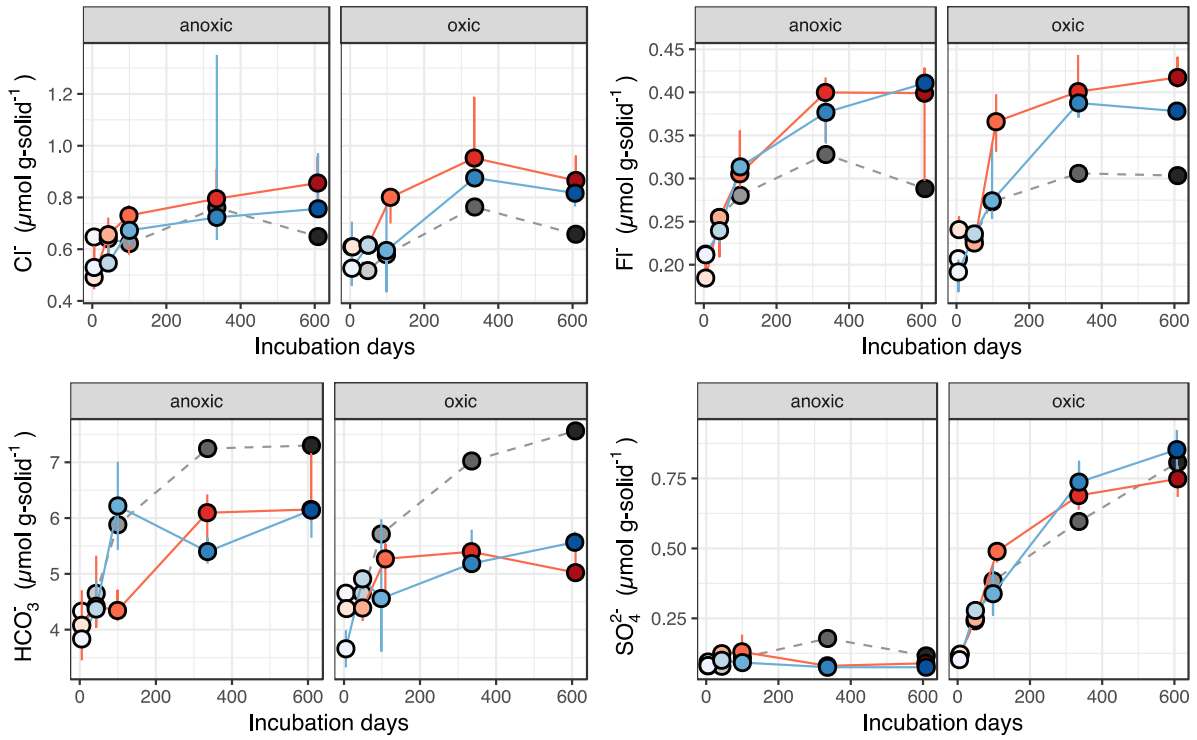

Figure 5.17 Major anions released in basal-sediment slurries incubated with rock flour. Red and blue series denote autoclaved (kill) and non-autoclaved (live) slurries, respectively. Grey series connected by a dashed line correspond to theoretical "control" levels calculated by adding the mean values obtained for flour-only and live-sediment-only incubations. Gram of solid corresponds to the added gram of dry rock flour plus wet basal sediments added to each vial.

5.4.3.4 Weathering profile of slurries

The difference in the kinetics of solute acquisition between flour and basal-sediment slurries is further demonstrated by looking at the associations between major ions released throughout the incubation period. The ratio of monovalent to divalent cations can loosely indicate the dominance of silicate over carbonate dissolution in subglacial systems, with monovalent cations mostly derived from silicate dissolution and divalent indicative of carbonate dissolution (Tranter et al., 2002; Wadham et al., 2010a). Results here therefore suggest that whereas both silicate and carbonate dissolution reactions characterised basal sediment incubations, samples containing flour were dominated by silicate weathering throughout the incubation period. This is first exemplified with the relationship between monovalent and divalent cations, which showed an almost 1:1 (0.93) relationship in terms of equivalent in anoxic and 3:4 (0.74) in oxic sediments incubated without flour, but little changes in divalent cation release (and therefore no monovalent-divalent cation correlation) for flour incubations (Fig. 5.18; Table 5.1). Given that

bicarbonates constitute the main anion released from both sediments and flour, a very similar trend between bicarbonate and major cation release is observed, with a ~ 1:2 association between both monovalent and divalent cations and bicarbonates in basal-sediment incubations lacking flour, and a clear monovalent to HCO_3^- (~ 1 to 1.6), but no divalent HCO_3^-, association for flour incubations (Fig. 5.18, Table 5.1). However, no clear differences in relationships (gradients) between autoclaved, live, and abiotic treatments on the weathering relationships between major cations (and major cations and HCO_3^-) was observed (Fig. 5.18). However, it should be underlined that cation exchange following carbonate hydrolysis likely dominated dissolution reactions during initial wetting of rock flour.

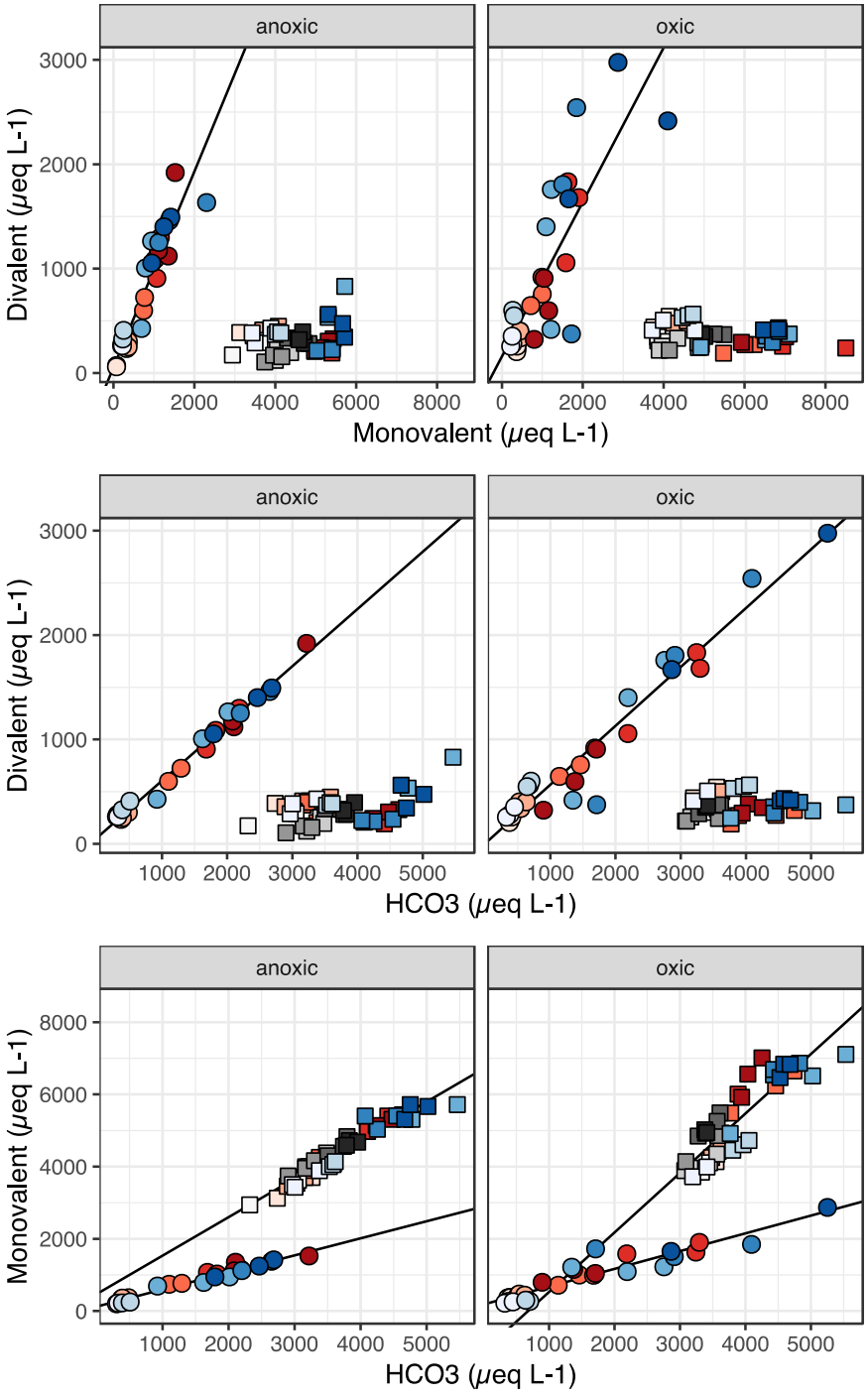

Figure 5.18 Association between divalent (Ca^{2+} + Mg^{2+}), monovalent (Na^{+} + K^{+}) and bicarbonate (HCO_3^{-}) ions in all incubation samples. Circles denote incubations with basal-sediments without the addition of flour; squares correspond to samples containing flour. Red and blue series denote autoclaved (kill) and non-autoclaved (live) slurries, respectively; grey squares correspond to crushed rock samples incubated in MQ water. Lighter and darker colours correspond to earlier and later samples, respectively (the same colour scheme used here is used in the previous time-series figures). The gradient, coefficient of determination (R^2), and significance of the linear regressions present on the figures are summarised in Table 1.

Sulphide oxidation (as inferred from sulphate release) was only apparent under oxic conditions, and only showed weak relationships with divalent cation releases in unamended live basal sediments (R^2 ~ 0.5; p-value ~ 0.004) (Fig. 5.19; Table 5.1). Focusing on Ca^{2+}:Mg^{2+} ratios can inform on the degree of calcite over dolomite dissolution (assuming congruent dissolution), with lower ratios reflecting increased dolomite contribution (Sharp et al., 2002; Wadham et al., 2010a; Boyd et al., 2014). Following the same assumptions, pyrite oxidation appears to be coupled preferentially to calcite dissolution in live basal sediments without flour (Fig. 5.19). Note that the preferential release of Ca^{2+} (higher Ca^{2+}:Mg^{2+}) in early killed controls may represent another artefact of autoclaving. In incubations containing crushed rocks, a small, yet consistent decrease in Ca^{2+}:Mg^{2+} do suggest increased dolomite (over calcite) dissolution over time (Fig. 5.19), which is consistent with previous studies that indicated similar trends in the weathering of older subglacial sediments (Sharp et al., 2002; Wadham et al., 2010a; Boyd et al., 2014). The acquisition of sulphate in slurries was more strongly correlated with monovalent cation releases in both flour amended and unamended incubations (Fig. 5.19, Table 1).

Overall, the relatively weak relationship between divalent cation and sulphate release, as well as the high difference in equivalents between major cation and sulphate released in live basal-sediment slurries without flour suggest a limiting contribution of pyrite oxidation (from microbial activity) to carbonate and silicate dissolution in the present incubation experiment in the absence of rock flour (Fig. 5.19, Table 1). Would both dissolution processes be solely driven by protons generated from the oxidation of sulphide, associations between divalent cations and sulphate and monovalent cations and sulphate would be of 2:1 and 1:1 respectively in terms of equivalent (Tranter et al., 2002). However, associations between sulphate and monovalent or divalent cations both have gradients exceeding 2 (~ 7 and 4 for monovalent and divalent cations versus sulphate, respectively; Table 5.1), indicating that additional reactions to sulphide oxidation must be responsible for the observed dissolution reactions. The increased dissolution of cations between live and killed incubations in basal sediments without flour at the end of the incubation period is roughly of 1000 μeq L^{-1}, compared to about 200 μeq L^{-1} for sulphate (Fig. 5.19). If all of the protons released from sulphide oxidation contributed to dissolution, then about only 10% and 20% of the increase between live and killed monovalent and divalent cation release could be attributed to the microbially driven oxidation of sulphides, respectively (~ 100 μeq L^{-1} of SO_4^{2-} for each monovalent (1:1) and divalent (2:1) cations). This suggests that other microbial reactions

were responsible for the majority of the observed increased weathering in live basal sediments (e.g. carbonation reactions due to microbial respiration).

In the presence of flour, however, (abiotic) sulphide oxidation appears to account for a larger fraction of monovalent ions released than for incubations without flour. The gradient between monovalent and sulphate release in that case was about 2.5 (Fig. 5.19; Table 5.1), also suggesting that all protons derived from sulphide oxidation would contribute to the release of monovalent cations (i.e. silicate dissolution). Considering that about 1000 μeq L^{-1} of sulphate and 3000 μel L^{-1} of monovalent cations were released over the incubation period (Fig. 5.19), then sulphide oxidation contributed to up to 33% of silicate dissolution from rock flour over the incubation period under oxic conditions.

Bicarbonate and sulphate release also showed relatively strong correlations (Fig. 5.19; Table 5.1). Such association is normally used to infer carbonate dissolution derived from sulphide oxidation (Tranter et al., 2002; Wadham et al., 2010a). Given the very small level divalent cations released from the rock flour, however, concurrent release of sulphate and bicarbonate in this case may reflect separate processes (e.g. silicate dissolution from carbonation and sulphide oxidation). However, some degree of cation exchange following carbonate dissolution coupled to sulphide oxidation cannot be excluded.

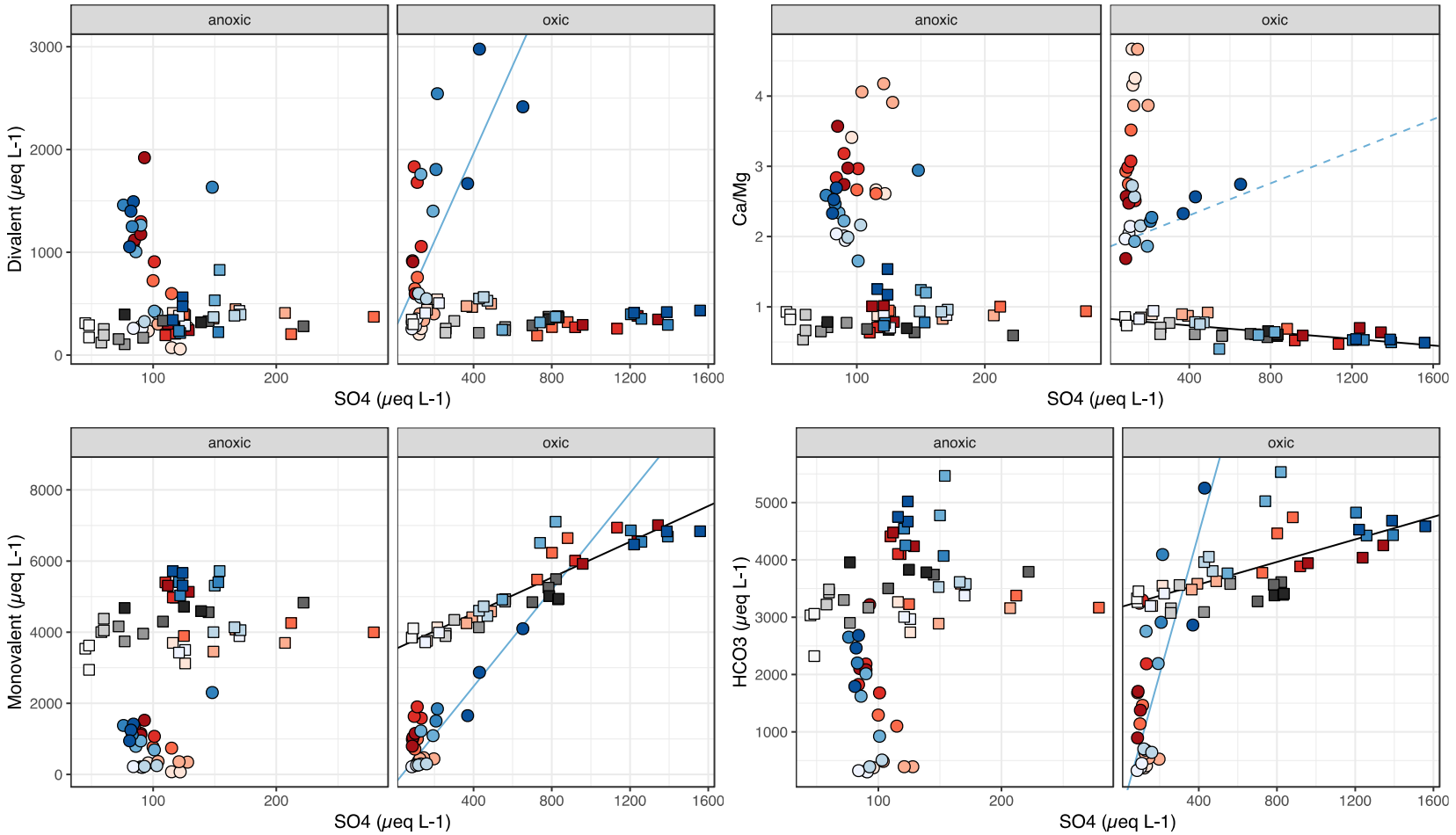

Figure 5.19 Association between divalent (Ca^{2+} + Mg^{2+}), monovalent (Na^{+} + K^{+}) and bicarbonate (HCO_3^-) with sulphate (SO_4^{2-}) in all incubation samples. Circles denote incubations with basal-sediments without the addition of flour; squares correspond to samples containing flour. Red and blue series denote autoclaved (kill) and non-autoclaved (live) slurries, respectively; grey squares correspond to crushed rock samples incubated in MQ water. Lighter and darker colours correspond to earlier and later samples, respectively (the same colour scheme used here is used in the previous time-series figures). The gradient, coefficient of determination (R^2), and significance of the linear regressions present on the figures are summarised in Table 1. Black gradients were calculated using all samples (i.e. live and controls) within a treatment; blue gradients only include live samples. The dashed blue gradient reflects a relatively small correlation (R^2 = 0.32, p-value = 0.05).

Table 5.1 Summary of gradients, intercepts, coefficients of determination (R^2) and significances (p-value) from figures 18 and 19.

Ion association	Anoxic				Oxic			
	Gradient	Intercept	R^2	p-value	Gradient	Intercept	R^2	p-value
Divalent vs monovalent - basal sediment (Fig. 18)	0.94	55.38	0.88	< 0.001	0.74	158	0.68	< 0.001
Divalent vs HCO_3^- - basal sediment (Fig. 18)	0.55	56.42	0.99	< 0.001	0.56	2.15	0.94	< 0.001
Monovalent vs HCO_3^- - basal sediment (Fig. 18)	0.47	122.89	0.96	< 0.001	0.49	182	0.89	< 0.001
Monovalent vs HCO_3^- - flour + sediment (Fig. 18)	1.07	466.21	0.93	< 0.001	1.65	-1119	0.78	< 0.001
Divalent vs SO_4^{2+} - basal sediment live only (Fig. 19)	-	-	-	-	4.27	255	0.49	0.004
Ca^{2+}/Mg^{2+} vs SO_4^{2+} - flour (Fig. 19)	-	-	-	-	-0.00023	0.83	0.50	< 0.001
Ca^{2+}/Mg^{2+} vs SO_4^{2+} - basal sediment live only (Fig. 19)	-	-	-	-	0.0010	2.04	0.32	0.05
Monovalent vs SO_4^{2+} - flour (Fig. 19)	-	-	-	-	2.51	3524	0.84	< 0.001
Monovalent vs SO_4^{2+} - basal sediment live only (Fig. 19)	-	-	-	-	6.80	-246	0.88	< 0.001
HCO3 vs SO_4^{2+} - flour (Fig. 19)	-	-	-	-	0.98	3177	0.46	< 0.001
HCO3 vs SO_4^{2+} - basal sediment live only (Fig. 19)	-	-	-	-	12.28	-455	0.65	< 0.001

5.4.3.5 "Quenching" effect of rock flour

Solute acquisition (resulting from weathering reactions) in the basal sediments incubated with rock-flour exhibited different kinetics than what was observed in either the incubations of rock flour in MQ water, or those solely comprised of basal sediments. That is, solutes measured in sediment-flour slurries often did not correspond to the sum of their parts measured in flour and sediment-only samples, separately. The dashed grey lines in Fig. 13-17 correspond to such theoretical "additive concentration levels" of solutes released from basal sediments and rock flour incubated independently (i.e. added average values from Fig. 3-7 and from the live series of Fig. 8-12). An apparent "quenching" effect on dissolution was therefore observed in incubations containing both flour and sediments. This was mostly apparent for divalent cations (Ca^{2+} + Mg^{2+}) and dissolved silica, which all reached levels much lower than in their basal-sediment-only counterparts (Fig. 11-12 versus 16-17). The high reactivity of flour, therefore, may have masked some of the biological weathering effects that were apparent in incubations without flour.

5.5 Discussion

5.5.1 Utilisation of released nutrients and energy sources by rock flour

An increase in H_2 formation compared to controls in anoxic live samples containing flour during the first 100 days of incubation is consistent with previous findings on the impact of microorganisms on H_2 formation in the presence of freshly crushed mineral at higher temperatures (Parkes et al., 2011). Parkes et al. (2011) indicated that the presence of prokaryotic cells (in estuary sediment slurries) stimulated the formation of H_2 gas from comminuted mineral. The exact mechanism(s) responsible for such H_2 production were not identified but authors alluded to increased surface weathering and/or prevention of surface passivation. During a similar experiment Parkes et al. (2018) further showed that mechanochemically produced H_2 (e.g. from rock milling) could fuel methanogenesis (at ~ 67°C), and that H_2 removal (e.g. via microbial oxidation) could potentially sustain and/or enhance H_2 generation by "refreshing" mineral surfaces and preventing feedback inhibition processes that arise from H_2 accumulation.

Alternatively, or concomitantly, to indirect H_2 generation from microbial activity, initial increases in H_2 formation by an active biota could reflect utilisation of nutrient and/or energy sources

released during the crushing process. For example, fermentation (e.g. of acetate or formate) can lead to H_2 formation in prokaryotes (Kim et al., 2010). Even though no clear relationships was observed between acetate or formate consumption and hydrogen formation in the current experiment, the order of magnitude differences between both analytes (μM versus nM for acetate and formate, and hydrogen, respectively) prevents from drawing direct correlations (Fig. 5.13 and 5.15).

All sets of live incubations showed some degree of H_2 consumption, suggestive of hydrogen oxidation by microorganisms (Fig. 5.8 and 5.13). Hydrogen generated by the comminution of bedrock by moving ice masses has been postulated to act as a previously unaccounted energy source for subglacial biota (Telling et al., 2015), and results here provide additional evidence to support this. Such mechanochemically generated hydrogen beneath ice masses has been hypothesised to fuel subglacial methanogenesis (Telling et al., 2015; Macdonald et al., 2018; Lamarche-Gagnon et al., 2019). In the current set of incubations, the addition of rock flour (and concomitant hydrogen release) was not accompanied with methane production that was significantly different from controls in live samples (Fig. 5.13). Somewhat surprisingly, only the oxic set of incubation, without the addition of flour, showed signs of methane production towards the end of the incubation period (Fig. 5.8). The absence of observed methanogenesis in flour-amended incubations may be explained by the oxidation state of the incubation slurries. Though in relatively low concentrations (<1%), molecular oxygen was still detectable in "anoxic" samples during the first 100 days of incubations (Fig. 5.8, 5.13); the redox state of the incubations may therefore not have been sufficiently reducing to favour methanogenesis. Additionally, oxidants (such as hydrogen peroxide) are believed to be generated during mineral crushing (as a result of water splitting) (Balk et al., 2009; Parkes et al., 2011; Tranter, 2015), which may further inhibit highly reducing biochemical reactions such as methanogenesis.

In their initial attempts at demonstrating methanogenesis sustained by mechanochemically derived H_2, Parkes et al. (2018) failed to sustain pure cultures of methanogens, despite the presence of elevated hydrogen levels and anoxic conditions. The authors attributed this inability to the generation of oxidants during the milling process, and resorted to the use of methanogenic enrichment cultures tolerant to low levels of oxygen in order to demonstrate hydrogenotrophic methanogenesis fuelled by H_2 derived from crushed rocks. It is therefore possible that oxidants generated during the crushing process would have affected putative methanogenic populations present in the current set of incubations, and perhaps more time would have been required to

observe methanogenesis in the basal sediments amended with rock flour (i.e. enough time for the community to further reduce environmental conditions). However, the observation of methane production in oxic incubations without flour (Fig. 5.8) would suggest that if such methane was derived from "traditional' methanogenesis, that the LG basal-ice communities may be adapted to cope with relatively high oxidising conditions. Deeper sediment layers in vials without flour may have contained reducing microenvironments favourable to methanogens (because oxidation would only have come from upper sediment layers in contact with the oxic slurry) unlike in incubations containing crushed rocks (where putative oxidants would have been distributed throughout the sediment-flour column). Alternatively, the apparent biogenic methane production recorded in oxic samples without flour may have resulted from "non-traditional" methanogenesis. Aerobic methane production has indeed been documented in bacteria as a result of orgnanophosphorus (i.e. methylphosphonates) metabolism (Karl et al., 2008; Repeta et al., 2016). Organophosphorus levels were not measured in the present experiment but the measured concentrations of organic phosphorous compounds in subglacial meltwaters have been reported as exceeding low (Hawkings et al., 2016); however, phosphonates have been reported in hypersaline Antarctic lakes (Williams et al., 2014). Interestingly, the rate of methane generated between the last two time points in the oxic live sediments was very similar to that measured by Stibal et al. (2012b) in incubation experiments on basal ice from Russell glacier (a neighbouring glacier from LG – see section 3.7.1.1) amended with hydrogen gas (i.e. ~ 0.2-0.3 pmol g^{-1} d^{-1}).

In addition to hydrogen, both acetate, and, to a lesser extent formate, liberated from mineral crushing were metabolised by live microbial populations, with most of the liberated acetate consumed during the first 50 days of incubations (Fig. 5.15). Mechanisms of release of small organics were not directly tested but acetate and formate likely originated from fluid inclusions within the rocks. The subsequent (>50 days) rise in acetate levels in anoxic live flour slurries may have reflected, at least partly, acetogenesis fuelled by mineral H_2 (Fig. 5.13, 5.15). Acetogenesis has been documented in anoxic basal sediments incubated at 2°C (Montross et al., 2013b). The addition of crushed basalt and quartz mineral to live sediment slurries have also been shown to trigger acetate production at relatively high temperatures (>50°C) (Parkes et al., 2011), and both acetate and formate have been shown to be released from crushed glacial rock debris, and subsequently microbially consumed, in incubation experiments (~ 300 days; ~ 2°C) with Norwegian glacier meltwaters (Kivimaki, 2005). Acetate has also recently been estimated to serve as the main methanogenic substrate beneath LG (Lamarche-Gagnon et al., 2019). Similar to what

was postulated regarding hydrogen derived from rock crushing, acetate derived from bedrock comminution by moving ice may also serve as an unaccounted methanogenic (or more generally microbial) substrate, either directly liberated during the grinding process, or indirectly by promoting microbial acetogenesis. Again, however, the lack of detected methanogenesis in the present set of incubations may suggest a delayed methanogenic response.

The relatively quick reduction in nitrate released from crushed rocks in live incubations (i.e. denitrification) is also consistent with previous experiments by Kivimaki (2005) using crushed rocks from Norwegian glaciers (Fig. 5.15). Moreover, denitrification (as inferred from decreases in nitrate concentrations in live incubations) has been shown in basal sediments of the alpine Haut Glacier d'Arolla glacier under both oxic and anoxic conditions (Montross et al., 2013b). Microbial utilisation of phosphate derived from comminuted minerals had not been demonstrated experimentally under glacially relevant conditions. Slower releases of phosphate (relative to controls) in live flour-sediment slurries further suggests microbial utilisation of flour-derived phosphate (Fig. 5.14). The putative bio-assimilation of this phosphate supports the idea that bedrock erosion beneath ice masses releases bioavailable phosphorus; the apparent "excess" of phosphate in live sediment-flour slurries at the end of the incubation period (Fig. 5.14) further supports findings from Leverett Glacier of exports of bioavailable phosphorus from the bed of the Greenland Ice sheet to surrounding oceans (Hawkings et al., 2016). It is unclear, however, why such phosphate release was only observed under oxic conditions (Fig. 5.14).

5.5.2 Microbial weathering effect

In the absence of rock flour, the lack of microbial impact on dissolution of major ions under anoxic conditions is consistent with previous experiments on subglacial sediment incubations. Similar findings were reported by Montross et al. (2013b), where microbial activity was attributed to increase the dissolution of both monovalent (Na^{+}, K^{+}) and divalent (Ca^{2+}, Mg^{2+}) cation-bearing minerals in cold incubations of Norwegian glacial basal sediments, and divalent cations from Swiss basal sediments, but exclusively under oxic conditions. Interestingly, a somewhat opposite trend was observed for incubations containing rock flour here, with increased dissolution rates of major ions in live samples only apparent under anoxic conditions, yet only during the first 100 days of incubation (Fig. 5.16). Dissolution rates and maximum concentrations of divalent cations, however, were lower in mixed flour-sediment slurries than in incubations without rock flour (Fig. 11, 16).

These results on weathering of rock flour contrasts with those of Kivimaki (2005). The author observed increased dissolution of major ions in both anoxic and oxic conditions in glacial meltwaters incubated with crushed rocks, as a result of microbial activity. The differences in the apparent microbial imprint on weathering of rock flour may result from the chemical reactivity of the rock flours used in each incubation. Crushed rocks here had much smaller grain sizes when compared to that used by Kivimaki (2005) (d_{50} values of ~5 μm (LG flour here; Fig. 5.2) and 66 μm (Bøldalsbreen flour in Kivimaki (2005))). Previous experiments have demonstrated that chemical reactivity in flour generally increases with decreasing grain size (Telling et al., 2015; Macdonald et al., 2018); putatively more reactive rock flour here may have, at least partly, masked biological weathering effects. The decreased levels of dissolved silica in flour incubations here suggest increased incongruent silicate dissolution, with most silica preserved in the amorphous form on freshly exposed mineral surfaces; a predominance of amorphous over dissolved silica is consistent with field study at LG, with amorphous Si constituting the main form (> 95%) of exported "reactive" silica from the LG catchment (Hawkings et al., 2017). Lastly, the mixing of both basal sediments and crushed rocks in a ~1:1 ratio here likely further affected dissolution kinetics. Chemical "complexation" reactions between older sediments and freshly comminuted rock likely affected the dissolution of some analytes in slurries containing both sediments and flour (see section 5.4.3.5), potentially further masking some of the biological imprint on mineral weathering in the present incubations that would not be detectable solely from measurements of dissolved species.

5.6 Conclusion

The present set of incubations provides experimental evidence that bedrock comminution by moving ice can provide (and replenish) energy (e.g. H_2), nutrient (e.g. NO_3^-, PO_4^{3-}), and simple organic carbon (e.g. acetate and formate) utilisable by subglacial microbial communities. However, results here highlight that extrapolations from simple wetting experiments may not always accurately depict putatively bioavailable geochemical species in subglacial systems. For example, increased hydrogen generation as a result of microbial activity reported here suggests that previous estimates of minerally produced H_2 beneath ice masses may have been underestimated (Telling et al., 2015). Microbial oxidation of H_2 confirms the bioavailability of H_2 released from rock crushing, yet the lack of detected methanogenesis, expected from H_2 (and acetate) released from rock comminution, hints at a more complex biological turnover following crushing events beneath the ice than simple utilisation of released energy from existing microbial

consortia, potentially providing alternate habitats (e.g. geochemical gradients) away from localised "grinding zone". The imprint of subglacial microorganisms on weathering reactions in the presence of rock flour was not obvious and may suggest a delayed response in environments with newly acquired flour (e.g. due to the generation of strong oxidants during the grinding process). However, results here were not exhaustive and likely missed an important component of weathering products, such as amorphous or solid-phase components, which may bear a stronger microbial signal than could be observed solely from dissolved ions and silica. Combining further geochemical (e.g. solid phase speciation) and molecular analyses, should provide additional insight on both the responsible biological actors in subglacial weathering reactions, as well as potential community composition transitions following crushing events.

6. Synthesis, limitations, and future work

The full extent and impact of a widespread, active biota beneath ice masses obviously will not be known for decades to come. Yet it is becoming increasingly clear that like they do elsewhere on Earth, microorganisms inhabiting subglacial habitats impact on geochemical processes *in situ*, and probably globally. The present thesis aimed at assessing the metabolic strategies employed by, as well as the impact of, microbial communities indigenous to subglacial ecosystems, and to study the hydrological, geochemical, and mechanical processes that shape and sustain such communities beneath the ice.

Results here arguably provided the strongest empirical evidence to date that large sectors of ice-sheet beds should be considered methanogenic wetlands, and by the same occasion, microbial "hotspots", supporting previous assumptions (Wadham et al., 2008; Wadham et al., 2012). Our findings also put the GrIS as a net source of atmospheric methane, highlighting the potential influence of a subglacial biota on a planetary scale. However, subglacial methane budgets described here only serve as a first-step assessment on the contribution of ice sheets to present day methane budgets, and more work is required to better capture the atmospheric footprint of current ice masses, as well as their potential roles in affecting future climate (e.g. see section 3.3, 3.8). Molecular surveys from bulk subglacial runoff also supported previous conceptual models of subglacial habitats in actively draining subglacial catchments (Tranter et al., 2005), and laboratory incubations the view that the mechanochemical erosion of glacial bedrock can act as an energy source and sustain microbial populations beneath the ice (Telling et al., 2015). All in all, therefore, the present thesis provided answers regarding what makes up, and what fuels subglacial habitats, supportive of previously depicted portrays of subglacial ecosystems (Tranter et al., 2005; Hodson et al., 2008; Wadham et al., 2008; Wadham et al., 2010b; Boetius et al., 2015; Telling et al., 2015).

It should be underlined, however, that results presented here were derived from a single location: i.e. the subglacial catchment of the Leverett Glacier in Southwest Greenland, and that more work is needed to apply findings to other, perhaps more isolated, subglacial environments. Furthermore, findings here were often incomplete, nuanced. For example, the large and continuous release of subglacial microbial methane measured *in situ* alluded to the presence of large methanogenic populations beneath the surveyed catchment, but methanogenic DNA sequences were under-represented in molecular surveys, only amounting to a very small fraction

of overall communities. Instead, 16S rRNA results suggested a strong role for methane oxidation beneath the ice, both aerobically and anaerobically. Incubation experiments indicated that subglacial erosion likely fuels subglacial communities, but that it may also potentially be detrimental, at least temporarily, to some microbial populations, and failed to link glacial erosion to methanogenesis (Telling et al., 2015). Microbial incubations and (molecular) field surveys were also not fully complementary, with the latter alluding to a strong role for iron (and methane) cycling beneath the ice that could not be tested experimentally here.

Of special interest would be to investigate the effect of high pressures on both geochemical and microbial processes beneath the ice. For example how high pressure differential impact on methane export to the atmosphere as discussed in section 3.8, but also on biogeochemical processes – e.g. by affecting (increasing) the solubility of bioavailable gases and potentially promote diffusion of bioavailable substrates through cell membranes, consequently enhancing biogeochemical reactions.

7. List of publications

7.1 Published

Lamarche-Gagnon, G., Wadham, J.L., Sherwood Lollar, B., Arndt, S., Fietzek, P., Beaton, A.D., Tedstone, A.J., Telling, J., Bagshaw, E.A., Hawkings, J.R., Kohler, T.J., Zarsky, J.D., Mowlem, M.C., Anesio, A.M., and Stibal, M. (2019). Greenland melt drives continuous export of methane from the ice-sheet bed. *Nature* 565, 73-77.

Hawkings, J.R., Hatton, J.E., Hendry, K.R., De Souza, G.F., Wadham, J.L., Ivanovic, R., Kohler, T.J., Stibal, M., Beaton, A., **Lamarche-Gagnon, G.**, Tedstone, A., Hain, M.P., Bagshaw, E., Pike, J., and Tranter, M. (2018). The silicon cycle impacted by past ice sheets. *Nature Communications* 9, 3210.

Žárský, J.D., Kohler, T.J., Yde, J.C., Falteisek, L., **Lamarche-Gagnon, G.**, Hawkings, J.R., Hatton, J.E., and Stibal, M. (2018). Prokaryotic assemblages in suspended and subglacial sediments within a glacierized catchment on Qeqertarsuaq (Disko Island), west Greenland. *FEMS Microbiology Ecology* 94, fiy100-fiy100.

Beaton, A.D., Wadham, J.L., Hawkings, J., Bagshaw, E.A., **Lamarche-Gagnon, G.**, Mowlem, M.C., and Tranter, M. (2017). High-Resolution in Situ Measurement of Nitrate in Runoff from the Greenland Ice Sheet. *Environmental Science & Technology* 51, 12518-12527.

Kohler, T.J., Žárský, J.D., Yde, J.C., **Lamarche-Gagnon, G.**, Hawkings, J.R., Tedstone, A.J., Wadham, J.L., Box, J.E., Beaton, A.D., and Stibal, M. (2017). Carbon dating reveals a seasonal progression in the source of particulate organic carbon exported from the Greenland Ice Sheet. *Geophysical Research Letters*, 6209-6217.

Telling, J., Boyd, E.S., Bone, N., Jones, E.L., Tranter, M., Macfarlane, J.W., Martin, P.G., Wadham, J.L., **Lamarche-Gagnon, G.**, Skidmore, M.L., Hamilton, T.L., Hill, E., Jackson, M., and Hodgson, D.A. (2015). Rock comminution as a source of hydrogen for subglacial ecosystems. *Nature Geosci* 8, 851-855.

7.2 In preparation

Lamarche-Gagnon, G., Wadham, J.L., Telling, J., Anesio, A.M., Žárský, J.D., Kohler, T.J., and Stibal, M. (*In preparation*). A microbial window into subglacial Greenland: molecular and biogeochemical interpretation of exported microbial assemblages from a subglacial Greenland catchment.

Lamarche-Gagnon, G., Wadham, J.L., Telling, J., Hawkings, J.R., Hatton, J.E., and Olivas, B.G. (*In preparation*). Glacial flour as a microbial fuel beneath ice-sheets.

8. References

Achberger, A.M., Christner, B.C., Michaud, A.B., Priscu, J.C., Skidmore, M.L., Vick-Majors, T.J., , T.W.S.T., Adkins, W., Anandakrishnan, S., Barbante, C., Barcheck, G., Beem, L., Behar, A., Beitch, M., Bolsey, R., Branecky, C., Carter, S., Christianson, K., Edwards, R., Fisher, A., Fricker, H., Foley, N., Guthrie, B., Hodson, T., Jacobel, R., Kelley, S., Mankoff, K., Mcbryan, E., Mikucki, J., Mitchell, A., Powell, R., Purcell, A., Sampson, D., Scherer, R., Sherve, J., Siegfried, M., and Tulaczyk, S. (2016). Microbial Community Structure of Subglacial Lake Whillans, West Antarctica. *Frontiers in Microbiology* 7.

Anesio, A.M., and Laybourn-Parry, J. (2012). Glaciers and ice sheets as a biome. *Trends Ecol Evol* 27, 219-225.

Atamanchuk, D., Tengberg, A., Aleynik, D., Fietzek, P., Shitashima, K., Lichtschlag, A., Hall, P.O.J., and Stahl, H. (2015). Detection of CO2 leakage from a simulated sub-seabed storage site using three different types of pCO2 sensors. *International Journal of Greenhouse Gas Control* 38, 121-134.

Balk, M., Bose, M., Ertem, G., Rogoff, D.A., Rothschild, L.J., and Freund, F.T. (2009). Oxidation of water to hydrogen peroxide at the rock–water interface due to stress-activated electric currents in rocks. *Earth and Planetary Science Letters* 283, 87-92.

Barbosa, P.M., Melack, J.M., Farjalla, V.F., Amaral, J.H.F., Scofield, V., and Forsberg, B.R. (2016). Diffusive methane fluxes from Negro, Solimões and Madeira rivers and fringing lakes in the Amazon basin. *Limnology and Oceanography*, n/a-n/a.

Bartholomew, I., Nienow, P., Mair, D., Hubbard, A., King, M.A., and Sole, A. (2010). Seasonal evolution of subglacial drainage and acceleration in a Greenland outlet glacier. *Nature Geosci* 3, 408-411.

Bartholomew, I., Nienow, P., Sole, A., Mair, D., Cowton, T., Palmer, S., and Wadham, J. (2011). Supraglacial forcing of subglacial drainage in the ablation zone of the Greenland ice sheet. *Geophysical Research Letters* 38, n/a-n/a.

Bates, S.T., Berg-Lyons, D., Caporaso, J.G., Walters, W.A., Knight, R., and Fierer, N. (2010). Examining the global distribution of dominant archaeal populations in soil. *The Isme Journal* 5, 908.

Beal, E.J., House, C.H., and Orphan, V.J. (2009). Manganese- and Iron-Dependent Marine Methane Oxidation. *Science* 325, 184-187.

Beaton, A.D., Wadham, J.L., Hawkings, J., Bagshaw, E.A., Lamarche-Gagnon, G., Mowlem, M.C., and Tranter, M. (2017). High-Resolution in Situ Measurement of Nitrate in Runoff from the Greenland Ice Sheet. *Environmental Science & Technology* 51, 12518-12527.

Bhatia, M.P., Das, S.B., Xu, L., Charette, M.A., Wadham, J.L., and Kujawinski, E.B. (2013). Organic carbon export from the Greenland ice sheet. *Geochimica et Cosmochimica Acta* 109, 329-344.

Boetius, A., Anesio, A.M., Deming, J.W., Mikucki, J.A., and Rapp, J.Z. (2015). Microbial ecology of the cryosphere: sea ice and glacial habitats. *Nature Reviews Microbiology*.

Borges, A.V., Abril, G., Darchambeau, F., Teodoru, C.R., Deborde, J., Vidal, L.O., Lambert, T., and Bouillon, S. (2015a). Divergent biophysical controls of aquatic CO2 and CH4 in the World's two largest rivers. *Scientific Reports* 5, 15614.

Borges, A.V., Darchambeau, F., Teodoru, C.R., Marwick, T.R., Tamooh, F., Geeraert, N., Omengo, F.O., Guerin, F., Lambert, T., Morana, C., Okuku, E., and Bouillon, S. (2015b). Globally significant greenhouse-gas emissions from African inland waters. *Nature Geosci* 8, 637-642.

Bottrell, S.H., and Tranter, M. (2002). Sulphide oxidation under partially anoxic conditions at the bed of the Haut Glacier d'Arolla, Switzerland. *Hydrological Processes* 16, 2363-2368.

Boyd, E.S., Hamilton, T.L., Havig, J.R., Skidmore, M.L., and Shock, E.L. (2014). Chemolithotrophic Primary Production in a Subglacial Ecosystem. *Applied and Environmental Microbiology* 80, 6146-6153.

Boyd, E.S., Lange, R.K., Mitchell, A.C., Havig, J.R., Hamilton, T.L., Lafrenière, M.J., Shock, E.L., Peters, J.W., and Skidmore, M. (2011). Diversity, Abundance, and Potential Activity of Nitrifying and Nitrate-Reducing Microbial Assemblages in a Subglacial Ecosystem. *Applied and Environmental Microbiology* 77, 4778-4787.

Boyd, E.S., Skidmore, M., Mitchell, A.C., Bakermans, C., and Peters, J.W. (2010). Methanogenesis in subglacial sediments. *Environ Microbiol Rep* 2, 685-692.

Bradley, J.A., Amend, J.P., and Larowe, D.E. (2018). Necromass as a Limited Source of Energy for Microorganisms in Marine Sediments. *Journal of Geophysical Research: Biogeosciences* 123, 577-590.

Brown, G.H. (2002). Glacier meltwater hydrochemistry. *Applied Geochemistry* 17, 855-883.

Burns, R., Wynn, P.M., Barker, P., Mcnamara, N., Oakley, S., Ostle, N., Stott, A.W., Tuffen, H., Zhou, Z., Tweed, F.S., Chesler, A., and Stuart, M. (2018). Direct isotopic evidence of biogenic methane production and efflux from beneath a temperate glacier. *Scientific Reports* 8, 17118.

Bussmann, I. (2013). Distribution of methane in the Lena Delta and Buor-Khaya Bay, Russia. *Biogeosciences* 10, 4641-4652.

Cai, C., Leu, A.O., Xie, G.-J., Guo, J., Feng, Y., Zhao, J.-X., Tyson, G.W., Yuan, Z., and Hu, S. (2018). A methanotrophic archaeon couples anaerobic oxidation of methane to Fe(III) reduction. *The ISME Journal* 12, 1929-1939.

Cameron, K.A., Stibal, M., Hawkings, J.R., Mikkelsen, A.B., Telling, J., Kohler, T.J., Gözdereliler, E., Zarsky, J.D., Wadham, J.L., and Jacobsen, C.S. (2017). Meltwater

export of prokaryotic cells from the Greenland ice sheet. *Environmental Microbiology* 19, 524-534.

Chandler, D.M., Wadham, J.L., Lis, G.P., Cowton, T., Sole, A., Bartholomew, I., Telling, J., Nienow, P., Bagshaw, E.B., Mair, D., Vinen, S., and Hubbard, A. (2013). Evolution of the subglacial drainage system beneath the Greenland Ice Sheet revealed by tracers. *Nature Geoscience* 6, 195-198.

Christensen, T.R., Arora, V.K., Gauss, M., Höglund-Isaksson, L., and Parmentier, F.-J.W. (2019). Tracing the climate signal: mitigation of anthropogenic methane emissions can outweigh a large Arctic natural emission increase. *Scientific Reports* 9, 1146.

Christiansen, J.R., and Jørgensen, C.J. (2018). First observation of direct methane emission to the atmosphere from the subglacial domain of the Greenland Ice Sheet. *Scientific Reports* 8, 16623.

Christner, B.C., Montross, G.G., and Priscu, J.C. (2012). Dissolved gases in frozen basal water from the NGRIP borehole: implications for biogeochemical processes beneath the Greenland Ice Sheet. *Polar Biology* 35, 1735-1741.

Christner, B.C., Priscu, J.C., Achberger, A.M., Barbante, C., Carter, S.P., Christianson, K., Michaud, A.B., Mikucki, J.A., Mitchell, A.C., Skidmore, M.L., Vick-Majors, T.J., and The, W.S.T. (2014). A microbial ecosystem beneath the West Antarctic ice sheet. *Nature* 512, 310-313.

Christoffersen, P., Bougamont, M., Hubbard, A., Doyle, S.H., Grigsby, S., and Pettersson, R. (2018). Cascading lake drainage on the Greenland Ice Sheet triggered by tensile shock and fracture. *Nature Communications* 9, 1064.

Chu, V.W. (2014). Greenland ice sheet hydrology: A review. *Progress in Physical Geography* 38, 19-54.

Conrad, R., and Wetter, B. (1990). Influence of temperature on energetics of hydrogen metabolism in homoacetogenic, methanogenic, and other anaerobic bacteria. *Archives of Microbiology* 155, 94-98.

Cowton, T., Nienow, P., Bartholomew, I., Sole, A., and Mair, D. (2012). Rapid erosion beneath the Greenland ice sheet. *Geology* 40, 343-346.

Das, S.B., Joughin, I., Behn, M.D., Howat, I.M., King, M.A., Lizarralde, D., and Bhatia, M.P. (2008). Fracture Propagation to the Base of the Greenland Ice Sheet During Supraglacial Lake Drainage. *Science* 320, 778.

Davie, M.K., and Buffett, B.A. (2001). A numerical model for the formation of gas hydrate below the seafloor. *Journal of Geophysical Research: Solid Earth* 106, 497-514.

Dawes, P.R. (2009). The bedrock geology under the Inland Ice: the next major challenge for Greenland mapping. *Geological Survey of Denmark and Greenland Bulletin* 17, 57-60.

Dieser, M., Broemsen, E.L., Cameron, K.A., King, G.M., Achberger, A., Choquette, K., Hagedorn, B., Sletten, R., Junge, K., and Christner, B.C. (2014). Molecular and biogeochemical evidence for methane cycling beneath the western margin of the Greenland Ice Sheet. *ISME J* 8, 2305-2316.

Dow, C.F., Hubbard, A., Booth, A.D., Doyle, S.H., Gusmeroli, A., and Kulessa, Y.B. (2013). Seismic evidence of mechanically weak sediments underlying Russell Glacier, West Greenland. *Annals of Glaciology* 54, 135-141.

Doyle, S.M., Montross, S.N., Skidmore, M.L., and Christner, B.C. (2013). Characterizing microbial diversity and the potential for metabolic function at− 15° C in the Basal Ice of Taylor Glacier, Antarctica. *Biology* 2, 1034-1053.

Dubnick, A., Kazemi, S., Sharp, M., Wadham, J., Hawkings, J., Beaton, A., and Lanoil, B. (2017). Hydrological controls on glacially exported microbial assemblages. *Journal of Geophysical Research: Biogeosciences* 122, 1049-1061.

Etiope, G., and Sherwood Lollar, B. (2013). Abiotic methane on Earth. *Reviews of Geophysics* 51, 276-299.

Ettwig, K.F., Butler, M.K., Le Paslier, D., Pelletier, E., Mangenot, S., Kuypers, M.M.M., Schreiber, F., Dutilh, B.E., Zedelius, J., De Beer, D., Gloerich, J., Wessels, H.J.C.T., Van Alen, T., Luesken, F., Wu, M.L., Van De Pas-Schoonen, K.T., Op Den Camp, H.J.M., Janssen-Megens, E.M., Francoijs, K.-J., Stunnenberg, H., Weissenbach, J., Jetten, M.S.M., and Strous, M. (2010). Nitrite-driven anaerobic methane oxidation by oxygenic bacteria. *Nature* 464, 543-548.

Fedorova, I., Chetverova, A., Bolshiyanov, D., Makarov, A., Boike, J., Heim, B., Morgenstern, A., Overduin, P.P., Wegner, C., Kashina, V., Eulenburg, A., Dobrotina, E., and Sidorina, I. (2015). Lena Delta hydrology and geochemistry: long-term hydrological data and recent field observations. *Biogeosciences* 12, 345-363.

Fiedler, B., Fietzek, P., Vieira, N., Silva, P., Bittig, H.C., and Körtzinger, A. (2012). In Situ CO2 and O2 Measurements on a Profiling Float. *Journal of Atmospheric and Oceanic Technology* 30, 112-126.

Fietzek, P., Fiedler, B., Steinhoff, T., and Körtzinger, A. (2013). In situ Quality Assessment of a Novel Underwater pCO2 Sensor Based on Membrane Equilibration and NDIR Spectrometry. *Journal of Atmospheric and Oceanic Technology* 31, 181-196.

Finneran, K.T., Johnsen, C.V., and Lovley, D.R. (2003). Rhodoferax ferrireducens sp. nov., a psychrotolerant, facultatively anaerobic bacterium that oxidizes acetate with the reduction of Fe (III). *International Journal of Systematic and Evolutionary Microbiology* 53, 669-673.

Fountain, A.G., and Walder, J.S. (1998). Water flow through temperate glaciers. *Reviews of Geophysics* 36, 299-328.

Hall, R.O., Kennedy, T.A., and Rosi-Marshall, E.J. (2012). Air–water oxygen exchange in a large whitewater river. *Limnology and Oceanography: Fluids and Environments* 2, 1-11.

Hamilton, T.L., Peters, J.W., Skidmore, M.L., and Boyd, E.S. (2013). Molecular evidence for an active endogenous microbiome beneath glacial ice. *ISME J* 7, 1402-1412.

Harper, J.T., Humphrey, N.F., Meierbachtol, T.W., Graly, J.A., and Fischer, U.H. (2017). Borehole Measurements Indicate Hard Bed Conditions, Kangerlussuaq Sector, Western Greenland Ice Sheet. *Journal of Geophysical Research: Earth Surface*, n/a-n/a.

Hatton, J.E., Hendry, K.R., Hawkings, J.R., Wadham, J.L., Kohler, T.J., Stibal, M., Beaton, A.D., Bagshaw, E.A., and Telling, J. (2019). Investigation of subglacial weathering under the Greenland Ice Sheet using silicon isotopes. *Geochimica et Cosmochimica Acta*.

Hawkings, J., Wadham, J., Tranter, M., Telling, J., Bagshaw, E., Beaton, A., Simmons, S.-L., Chandler, D., Tedstone, A., and Nienow, P. (2016). The Greenland Ice Sheet as a hot spot of phosphorus weathering and export in the Arctic. *Global Biogeochemical Cycles* 30, 191-210.

Hawkings, J.R., Wadham, J.L., Benning, L.G., Hendry, K.R., Tranter, M., Tedstone, A., Nienow, P., and Raiswell, R. (2017). Ice sheets as a missing source of silica to the polar oceans. *Nature Communications* 8, 14198.

Hawkings, J.R., Wadham, J.L., Tranter, M., Lawson, E., Sole, A., Cowton, T., Tedstone, A.J., Bartholomew, I., Nienow, P., Chandler, D., and Telling, J. (2015). The effect of warming climate on nutrient and solute export from the Greenland Ice Sheet. *Geochemical Perspectives Letters* 1, 94-104.

Hawkings, J.R., Wadham, J.L., Tranter, M., Raiswell, R., Benning, L.G., Statham, P.J., Tedstone, A., Nienow, P., Lee, K., and Telling, J. (2014). Ice sheets as a significant source of highly reactive nanoparticulate iron to the oceans. *Nat Commun* 5, 3929.

Hodson, A., Anesio, A.M., Tranter, M., Fountain, A., Osborn, M., Priscu, J., Laybourn-Parry, J., and Sattler, B. (2008). Glacial ecosystems. *Ecological Monographs* 78, 41-67.

Hoffman, M.J., Andrews, L.C., Price, S.A., Catania, G.A., Neumann, T.A., Lüthi, M.P., Gulley, J., Ryser, C., Hawley, R.L., and Morriss, B. (2016). Greenland subglacial drainage evolution regulated by weakly connected regions of the bed. *Nature Communications* 7, 13903.

Hoffman, M.J., Perego, M., Andrews, L.C., Price, S.F., Neumann, T.A., Johnson, J.V., Catania, G., and Lüthi, M.P. (2018). Widespread Moulin Formation During Supraglacial Lake Drainages in Greenland. *Geophysical Research Letters* 45, 778-788.

Hoffman, P.F., Kaufman, A.J., Halverson, G.P., and Schrag, D.P. (1998). A Neoproterozoic Snowball Earth. *Science* 281, 1342-1346.

Hubbard, B.P., Sharp, M.J., Willis, I.C., Nielsen, M.K., and Smart, C.C. (1995). Borehole water-level variations and the structure of the subglacial hydrological system of Haut Glacier d'Arolla, Valais, Switzerland. *Journal of Glaciology* 41, 572-583.

Karl, D.M., Beversdorf, L., Björkman, K.M., Church, M.J., Martinez, A., and Delong, E.F. (2008). Aerobic production of methane in the sea. *Nature Geoscience* 1, 473.

Kiene, R.P., Oremland, R.S., Catena, A., Miller, L.G., and Capone, D.G. (1986). Metabolism of Reduced Methylated Sulfur Compounds in Anaerobic Sediments and by a Pure Culture of an Estuarine Methanogen. *Applied and Environmental Microbiology* 52, 1037.

Kim, B.-R., Shin, J., Guevarra, R.B., Lee, J.H., Kim, D.W., Seol, K.-H., Lee, J.-H., Kim, H.B., and Isaacson, R.E. (2017). Deciphering diversity indices for better understanding of the microbial communities. *J Microbiol Biotechnol* 27, 2089-2093.

Kim, Y.J., Lee, H.S., Kim, E.S., Bae, S.S., Lim, J.K., Matsumi, R., Lebedinsky, A.V., Sokolova, T.G., Kozhevnikova, D.A., Cha, S.-S., Kim, S.-J., Kwon, K.K., Imanaka, T., Atomi, H., Bonch-Osmolovskaya, E.A., Lee, J.-H., and Kang, S.G. (2010). Formate-driven growth coupled with H2 production. *Nature* 467, 352.

Kirschke, S., Bousquet, P., Ciais, P., Saunois, M., Canadell, J.G., Dlugokencky, E.J., Bergamaschi, P., Bergmann, D., Blake, D.R., Bruhwiler, L., Cameron-Smith, P., Castaldi, S., Chevallier, F., Feng, L., Fraser, A., Heimann, M., Hodson, E.L., Houweling, S., Josse, B., Fraser, P.J., Krummel, P.B., Lamarque, J.-F., Langenfelds, R.L., Le Quere, C., Naik, V., O'doherty, S., Palmer, P.I., Pison, I., Plummer, D., Poulter, B., Prinn, R.G., Rigby, M., Ringeval, B., Santini, M., Schmidt, M., Shindell, D.T., Simpson, I.J., Spahni, R., Steele, L.P., Strode, S.A., Sudo, K., Szopa, S., Van Der Werf, G.R., Voulgarakis, A., Van Weele, M., Weiss, R.F., Williams, J.E., and Zeng, G. (2013). Three decades of global methane sources and sinks. *Nature Geosci* 6, 813-823.

Kivimaki, A.-L. (2005). *Presence and activity of microbial populations in glaciers and their impact on rock weathering at glacial beds.* PhD, University of Bristol.

Kohler, T.J., Žárský, J.D., Yde, J.C., Lamarche-Gagnon, G., Hawkings, J.R., Tedstone, A.J., Wadham, J.L., Box, J.E., Beaton, A.D., and Stibal, M. (2017). Carbon dating reveals a seasonal progression in the source of particulate organic carbon exported from the Greenland Ice Sheet. *Geophysical Research Letters*, 6209-6217.

Kozich, J.J., Westcott, S.L., Baxter, N.T., Highlander, S.K., and Schloss, P.D. (2013). Development of a Dual-Index Sequencing Strategy and Curation Pipeline for Analyzing Amplicon Sequence Data on the MiSeq Illumina Sequencing Platform. *Applied and Environmental Microbiology* 79, 5112-5120.

Kulessa, B., Hubbard, A.L., Booth, A.D., Bougamont, M., Dow, C.F., Doyle, S.H., Christoffersen, P., Lindbäck, K., Pettersson, R., Fitzpatrick, A.a.W., and Jones, G.A. (2017). Seismic evidence for complex sedimentary control of Greenland Ice Sheet flow. *Science Advances* 3.

Lamarche-Gagnon, G., Wadham, J.L., Sherwood Lollar, B., Arndt, S., Fietzek, P., Beaton, A.D., Tedstone, A.J., Telling, J., Bagshaw, E.A., Hawkings, J.R., Kohler, T.J., Zarsky, J.D., Mowlem, M.C., Anesio, A.M., and Stibal, M. (2019). Greenland melt drives continuous export of methane from the ice-sheet bed. *Nature* 565**,** 73-77.

Lanoil, B., Skidmore, M., Priscu, J.C., Han, S., Foo, W., Vogel, S.W., Tulaczyk, S., and Engelhardt, H. (2009). Bacteria beneath the West Antarctic ice sheet. *Environ Microbiol* 11**,** 609-615.

Lawson, E.C., Wadham, J.L., Tranter, M., Stibal, M., Lis, G.P., Butler, C.E.H., Laybourn-Parry, J., Nienow, P., Chandler, D., and Dewsbury, P. (2014). Greenland Ice Sheet exports labile organic carbon to the Arctic oceans. *Biogeosciences* 11**,** 4015-4028.

Lindbäck, K., Pettersson, R., Hubbard, A.L., Doyle, S.H., Van As, D., Mikkelsen, A.B., and Fitzpatrick, A.A. (2015). Subglacial water drainage, storage, and piracy beneath the Greenland ice sheet. *Geophysical Research Letters* 42**,** 7606-7614.

Lofton, D.D., Whalen, S.C., and Hershey, A.E. (2014). Effect of temperature on methane dynamics and evaluation of methane oxidation kinetics in shallow Arctic Alaskan lakes. *Hydrobiologia* 721**,** 209-222.

Macdonald, M.L., Wadham, J.L., Telling, J., and Skidmore, M.L. (2018). Glacial Erosion Liberates Lithologic Energy Sources for Microbes and Acidity for Chemical Weathering Beneath Glaciers and Ice Sheets. *Frontiers in Earth Science* 6.

Macgregor, J.A., Fahnestock, M.A., Catania, G.A., Aschwanden, A., Clow, G.D., Colgan, W.T., Gogineni, S.P., Morlighem, M., Nowicki, S.M.J., Paden, J.D., Price, S.F., and Seroussi, H. (2016). A synthesis of the basal thermal state of the Greenland Ice Sheet. *Journal of Geophysical Research: Earth Surface* 121**,** 1328-1350.

Maurice, L., Rawlins, B.G., Farr, G., Bell, R., and Gooddy, D.C. (2017). The Influence of Flow and Bed Slope on Gas Transfer in Steep Streams and Their Implications for Evasion of CO2. *Journal of Geophysical Research: Biogeosciences* 122**,** 2862-2875.

Mcmurdie, P., and Holmes, S. (2013). phyloseq: An R Package for Reproducible Interactive Analysis and Graphics of Microbiome Census Data. *PLoS ONE* 8**,** e61217-e61217.

Michaud, A.B., Dore, J.E., Achberger, A.M., Christner, B.C., Mitchell, A.C., Skidmore, M.L., Vick-Majors, T.J., and Priscu, J.C. (2017). Microbial oxidation as a methane sink beneath the West Antarctic Ice Sheet. *Nature Geosci* 10**,** 582-586.

Mikucki, J.A., Pearson, A., Johnston, D.T., Turchyn, A.V., Farquhar, J., Schrag, D.P., Anbar, A.D., Priscu, J.C., and Lee, P.A. (2009). A Contemporary Microbially Maintained Subglacial Ferrous "Ocean". *Science* 324, 397-400.

Mitchell, A.C., Lafreniere, M.J., Skidmore, M.L., and Boyd, E.S. (2013). Influence of bedrock mineral composition on microbial diversity in a subglacial environment. *Geology* 41, 855-858.

Miteva, V., Teacher, C., Sowers, T., and Brenchley, J. (2009). Comparison of the microbial diversity at different depths of the GISP2 Greenland ice core in relationship to deposition climates. *Environmental Microbiology* 11, 640-656.

Miteva, V.I., Sheridan, P.P., and Brenchley, J.E. (2004). Phylogenetic and Physiological Diversity of Microorganisms Isolated from a Deep Greenland Glacier Ice Core. *Applied and Environmental Microbiology* 70, 202-213.

Montross, S., Skidmore, M., Christner, B., Samyn, D., Tison, J.-L., Lorrain, R., Doyle, S., and Fitzsimons, S. (2013a). Debris-Rich Basal Ice as a Microbial Habitat, Taylor Glacier, Antarctica. *Geomicrobiology Journal* 31, 76-81.

Montross, S.N., Skidmore, M., Tranter, M., Kivimäki, A.-L., and Parkes, R.J. (2013b). A microbial driver of chemical weathering in glaciated systems. *Geology* 41, 215-218.

Moreira-Turcq, P., Seyler, P., Guyot, J.L., and Etcheber, H. (2003). Exportation of organic carbon from the Amazon River and its main tributaries. *Hydrological Processes* 17, 1329-1344.

Mount, D.W. (2007). Using the Basic Local Alignment Search Tool (BLAST). *Cold Spring Harbor Protocols* 2007, pdb.top17.

Murray, A.E., Kenig, F., Fritsen, C.H., Mckay, C.P., Cawley, K.M., Edwards, R., Kuhn, E., Mcknight, D.M., Ostrom, N.E., Peng, V., Ponce, A., Priscu, J.C., Samarkin, V., Townsend, A.T., Wagh, P., Young, S.A., Yung, P.T., and Doran, P.T. (2012). Microbial life at −13 °C in the brine of an ice-sealed Antarctic lake. *Proceedings of the National Academy of Sciences* 109, 20626-20631.

Muster, S., Langer, M., Heim, B., Westermann, S., and Boike, J. (2012). Subpixel heterogeneity of ice-wedge polygonal tundra: a multi-scale analysis of land cover and evapotranspiration in the Lena River Delta, Siberia. *Tellus B: Chemical and Physical Meteorology* 64, 17301.

Nienow, P., Sharp, M., and Willis, I. (1998). Seasonal changes in the morphology of the subglacial drainage system, Haut Glacier d'Arolla, Switzerland. *Earth Surface Processes and Landforms* 23, 825-843.

Nienow, P.W., Sole, A.J., Slater, D.A., and Cowton, T.R. (2017). Recent Advances in Our Understanding of the Role of Meltwater in the Greenland Ice Sheet System. *Current Climate Change Reports* 3**,** 330-344.

Nixon, S.L., Telling, J., Wadham, J.L., and Cockell, C.S. (2016). Viable cold-tolerant iron-reducing microorganisms in geographically-isolated subglacial environments. *Biogeosciences Discuss.* 2016**,** 1-19.

Overeem, I., Hudson, B.D., Syvitski, J.P.M., Mikkelsen, A.B., Hasholt, B., Van Den Broeke, M.R., Noël, B.P.Y., and Morlighem, M. (2017). Substantial export of suspended sediment to the global oceans from glacial erosion in Greenland. *Nature Geoscience* 10**,** 859.

Palmer, S., Shepherd, A., Nienow, P., and Joughin, I. (2011). Seasonal speedup of the Greenland Ice Sheet linked to routing of surface water. *Earth and Planetary Science Letters* 302**,** 423-428.

Parkes, R.J., Berlendis, S., Roussel, E.G., Bahruji, H., Webster, G., Oldroyd, A., Weightman, A.J., Bowker, M., Davies, P.R., and Sass, H. (2018). Rock-crushing derived hydrogen directly supports a methanogenic community: significance for the deep biosphere. *Environmental Microbiology Reports* 0.

Parkes, R.J., Linnane, C.D., Webster, G., Sass, H., Weightman, A.J., Hornibrook, E.R.C., and Horsfield, B. (2011). Prokaryotes stimulate mineral H2 formation for the deep biosphere and subsequent thermogenic activity. *Geology* 39**,** 219-222.

Petrenko, V.V., Smith, A.M., Schaefer, H., Riedel, K., Brook, E., Baggenstos, D., Harth, C., Hua, Q., Buizert, C., Schilt, A., Fain, X., Mitchell, L., Bauska, T., Orsi, A., Weiss, R.F., and Severinghaus, J.P. (2017). Minimal geological methane emissions during the Younger Dryas–Preboreal abrupt warming event. *Nature* 548**,** 443-446.

Portnov, A., Vadakkepuliyambatta, S., Mienert, J., and Hubbard, A. (2016). Ice-sheet-driven methane storage and release in the Arctic. *Nat Commun* 7.

Quast, C., Pruesse, E., Gerken, J., Peplies, J., Yarza, P., Yilmaz, P., Schweer, T., and Glöckner, F.O. (2012). The SILVA ribosomal RNA gene database project: improved data processing and web-based tools. *Nucleic Acids Research* 41**,** D590-D596.

Raymond, P.A., Hartmann, J., Lauerwald, R., Sobek, S., Mcdonald, C., Hoover, M., Butman, D., Striegl, R., Mayorga, E., Humborg, C., Kortelainen, P., Durr, H., Meybeck, M., Ciais, P., and Guth, P. (2013). Global carbon dioxide emissions from inland waters. *Nature* 503**,** 355-359.

Raymond, P.A., Zappa, C.J., Butman, D., Bott, T.L., Potter, J., Mulholland, P., Laursen, A.E., Mcdowell, W.H., and Newbold, D. (2012). Scaling the gas transfer velocity and hydraulic geometry in streams and small rivers. *Limnology and Oceanography: Fluids and Environments* 2**,** 41-53.

Repeta, D.J., Ferrón, S., Sosa, O.A., Johnson, C.G., Repeta, L.D., Acker, M., Delong, E.F., and Karl, D.M. (2016). Marine methane paradox explained by bacterial degradation of dissolved organic matter. *Nature Geoscience* 9, 884.

Ryser, C., Lüthi, M.P., Andrews, L.C., Catania, G.A., Funk, M., Hawley, R., Hoffman, M., and Neumann, T.A. (2014). Caterpillar-like ice motion in the ablation zone of the Greenland ice sheet. *Journal of Geophysical Research: Earth Surface* 119, 2258-2271.

Sawakuchi, H.O., Bastviken, D., Sawakuchi, A.O., Krusche, A.V., Ballester, M.V.R., and Richey, J.E. (2014). Methane emissions from Amazonian Rivers and their contribution to the global methane budget. *Global Change Biology* 20, 2829-2840.

Schaefer, H., Fletcher, S.E.M., Veidt, C., Lassey, K.R., Brailsford, G.W., Bromley, T.M., Dlugokencky, E.J., Michel, S.E., Miller, J.B., Levin, I., Lowe, D.C., Martin, R.J., Vaughn, B.H., and White, J.W.C. (2016). A 21st century shift from fossil-fuel to biogenic methane emissions indicated by 13CH4. *Science*.

Schloss, P.D., Westcott, S.L., Ryabin, T., Hall, J.R., Hartmann, M., Hollister, E.B., Lesniewski, R.A., Oakley, B.B., Parks, D.H., Robinson, C.J., Sahl, J.W., Stres, B., Thallinger, G.G., Van Horn, D.J., and Weber, C.F. (2009). Introducing mothur: Open-Source, Platform-Independent, Community-Supported Software for Describing and Comparing Microbial Communities. *Applied and Environmental Microbiology* 75, 7537-7541.

Schmidt, M., Linke, P., and Esser, D. (2013). Recent Development in IR Sensor Technology for Monitoring Subsea Methane Discharge. *Marine Technology Society Journal* 47, 27-36.

Schuster, P.F. (2003). Water and sediment quality in the Yukon River basin, Alaska, during water year 2001.

Schuster, P.F. (2005a). "Water and sediment quality in the Yukon River basin, Alaska, during water year 2002", in: *Open-File Report.* - ed.).

Schuster, P.F. (2005b). "Water and sediment quality in the Yukon River basin, Alaska, during water year 2003", in: *Open-File Report.* - ed.).

Schuster, P.F. (2006). "Water and sediment quality in the Yukon River basin, Alaska, during water year 2004", in: *Open-File Report.* - ed.).

Sharp, M., Creaser, R.A., and Skidmore, M. (2002). Strontium isotope composition of runoff from a glaciated carbonate terrain. *Geochimica et Cosmochimica Acta* 66, 595-614.

Sharp, M., Parkes, J., Cragg, B., Fairchild, I.J., Lamb, H., and Tranter, M. (1999). Widespread bacterial populations at glacier beds and their relationship to rock weathering and carbon cycling. *Geology* 27, 107-110.

Sherwood Lollar, B., Hirschorn, S.K., Chartrand, M.M.G., and Lacrampe-Couloume, G. (2007). An Approach for Assessing Total Instrumental Uncertainty in Compound-Specific Carbon Isotope Analysis: Implications for Environmental Remediation Studies. *Analytical Chemistry* 79, 3469-3475.

Skidmore, M., Tranter, M., Tulaczyk, S., and Lanoil, B. (2010). Hydrochemistry of ice stream beds - ”evaporitic or microbial effects? *Hydrological Processes*, 517-523.

Skidmore, M.L., Foght, J.M., and Sharp, M.J. (2000). Microbial Life beneath a High Arctic Glacier. *Applied and Environmental Microbiology* 66, 3214-3220.

Souchez, R., Janssens, L., Lemmens, M., and Stauffer, B. (1995a). Very low oxygen concentration in basal ice from Summit, central Greenland. *Geophysical Research Letters* 22, 2001-2004.

Souchez, R., Jouzel, J., Landais, A., Chappellaz, J., Lorrain, R., and Tison, J.L. (2006). Gas isotopes in ice reveal a vegetated central Greenland during ice sheet invasion. *Geophysical Research Letters* 33, n/a-n/a.

Souchez, R., Lemmens, M., and Chappellaz, J. (1995b). Flow-induced mixing in the GRIP basal ice deduced from the CO2 and CH4 records. *Geophysical Research Letters* 22, 41-44.

Stanley, E.H., Casson, N.J., Christel, S.T., Crawford, J.T., Loken, L.C., and Oliver, S.K. (2016). The ecology of methane in streams and rivers: patterns, controls, and global significance. *Ecological Monographs* 86, 146-171.

Stevens, L.A., Behn, M.D., Mcguire, J.J., Das, S.B., Joughin, I., Herring, T., Shean, D.E., and King, M.A. (2015). Greenland supraglacial lake drainages triggered by hydrologically induced basal slip. *Nature* 522, 73.

Stibal, M., Hasan, F., Wadham, J.L., Sharp, M.J., and Anesio, A.M. (2012a). Prokaryotic diversity in sediments beneath two polar glaciers with contrasting organic carbon substrates. *Extremophiles* 16, 255-265.

Stibal, M., Wadham, J.L., Lis, G.P., Telling, J., Pancost, R.D., Dubnick, A., Sharp, M.J., Lawson, E.C., Butler, C.E.H., Hasan, F., Tranter, M., and Anesio, A.M. (2012b). Methanogenic potential of Arctic and Antarctic subglacial environments with contrasting organic carbon sources. *Global Change Biology* 18, 3332-3345.

Striegl, R.G., Dornblaser, M.M., Mcdonald, C.P., Rover, J.R., and Stets, E.G. (2012). Carbon dioxide and methane emissions from the Yukon River system. *Global Biogeochemical Cycles* 26, n/a-n/a.

Team, R.C. (2018). "R: A language and environment for statistical computing. R Foundation for Statistical Computing".).

Tedesco, M., Fettweis, X., Mote, T., Wahr, J., Alexander, P., Box, J.E., and Wouters, B. (2013). Evidence and analysis of 2012 Greenland records from spaceborne observations, a regional climate model and reanalysis data. *The Cryosphere* 7, 615-630.

Tedstone, A.J., Nienow, P.W., Sole, A.J., Mair, D.W.F., Cowton, T.R., Bartholomew, I.D., and King, M.A. (2013). Greenland ice sheet motion insensitive to exceptional meltwater forcing. *Proceedings of the National Academy of Sciences* 110, 19719-19724.

Telling, J., Boyd, E.S., Bone, N., Jones, E.L., Tranter, M., Macfarlane, J.W., Martin, P.G., Wadham, J.L., Lamarche-Gagnon, G., Skidmore, M.L., Hamilton, T.L., Hill, E., Jackson, M., and Hodgson, D.A. (2015). Rock comminution as a source of hydrogen for subglacial ecosystems. *Nature Geosci* 8, 851-855.

Tian, X. (2014). *Nutrient release by subglacial erosion as simulated by rock crushing under laboratory conditions.* MSc, University of Bristol.

Tison, J.-L., Souchez, R., Wolff, E.W., Moore, J.C., Legrand, M.R., and De Angelis, M. (1998). Is a periglacial biota responsible for enhanced dielectric response in basal ice from the Greenland Ice Core Project ice core? *Journal of Geophysical Research: Atmospheres* 103, 18885-18894.

Tranter, M. (2015). Grand challenge for low temperature and pressure geochemistry—sparks in the dark, on Earth, Mars, and throughout the Galaxy. *Frontiers in Earth Science* 3.

Tranter, M., Sharp, M.J., Lamb, H.R., Brown, G.H., Hubbard, B.P., and Willis, I.C. (2002). Geochemical weathering at the bed of Haut Glacier d'Arolla, Switzerland—a new model. *Hydrological Processes* 16, 959-993.

Tranter, M., Skidmore, M., and Wadham, J. (2005). Hydrological controls on microbial communities in subglacial environments. *Hydrological Processes* 19, 995-998.

Tung, H., Price, P., Bramall, N., and Vrdoljak, G. (2006). Microorganisms metabolizing on clay grains in 3-km-deep Greenland basal ice. *Astrobiology* 6, 69-86.

Tung, H.C., Bramall, N.E., and Price, P.B. (2005). Microbial origin of excess methane in glacial ice and implications for life on Mars. *Proceedings of the National Academy of Sciences of the United States of America* 102, 18292-18296.

U.S. Geological Survey (2016). *National Water Information System data available on the World Wide Web (USGS Water Data for the Nation)* [Online]. Available: http://waterdata.usgs.gov/nwis/ [Accessed March 01 2017].

Vick-Majors, T.J., Mitchell, A.C., Achberger, A.M., Christner, B.C., Dore, J.E., Michaud, A.B., Mikucki, J.A., Purcell, A.M., Skidmore, M.L., Priscu, J.C., and Team, T.W.S. (2016). Physiological Ecology of Microorganisms in Subglacial Lake Whillans. *Frontiers in Microbiology* 7, 1705.

Wadham, J.L., Arndt, S., Tulaczyk, S., Stibal, M., Tranter, M., Telling, J., Lis, G.P., Lawson, E., Ridgwell, A., Dubnick, A., Sharp, M.J., Anesio, A.M., and Butler, C.E.H. (2012). Potential methane reservoirs beneath Antarctica. *Nature* 488**,** 633-637.

Wadham, J.L., De'ath, R., Monteiro, F.M., Tranter, M., Ridgwell, A., Raiswell, R., and Tulaczyk, S. (2013). The potential role of the Antarctic Ice Sheet in global biogeochemical cycles. *Earth and Environmental Science Transactions of the Royal Society of Edinburgh* 104**,** 55-67.

Wadham, J.L., Hawkings, J., Tarasov, L., Gregoire, L., Spencer, R.G.M., Gutjahr, M., Ridgwell, A., and Kohfeld, K. (*In review*). Why ice sheets matter for the global carbon cycle. *Nat Commun*.

Wadham, J.L., Hawkings, J., Telling, J., Chandler, D., Alcock, J., O'donnell, E., Kaur, P., Bagshaw, E., Tranter, M., Tedstone, A., and Nienow, P. (2016). Sources, cycling and export of nitrogen on the Greenland Ice Sheet. *Biogeosciences* 13**,** 6339-6352.

Wadham, J.L., Tranter, M., Hodson, A.J., Hodgkins, R., Bottrell, S., Cooper, R., and Raiswell, R. (2010a). Hydro-biogeochemical coupling beneath a large polythermal Arctic glacier: Implications for subice sheet biogeochemistry. *Journal of Geophysical Research* 115.

Wadham, J.L., Tranter, M., Skidmore, M., Hodson, A.J., Priscu, J., Lyons, W.B., Sharp, M., Wynn, P., and Jackson, M. (2010b). Biogeochemical weathering under ice: Size matters. *Global Biogeochemical Cycles* 24**,** n/a-n/a.

Wadham, J.L., Tranter, M., Tulaczyk, S., and Sharp, M. (2008). Subglacial methanogenesis: A potential climatic amplifier? *Global Biogeochemical Cycles* 22**,** n/a-n/a.

Walter Anthony, K.M., Anthony, P., Grosse, G., and Chanton, J. (2012). Geologic methane seeps along boundaries of Arctic permafrost thaw and melting glaciers. *Nature Geosci* 5**,** 419-426.

Walter, F., Chaput, J., and Lüthi, M.P. (2014). Thick sediments beneath Greenland's ablation zone and their potential role in future ice sheet dynamics. *Geology* 42**,** 487-490.

Wanninkhof, R. (2014). Relationship between wind speed and gas exchange over the ocean revisited. *Limnology and Oceanography: Methods* 12**,** 351-362.

Ward, J.A., Slater, G.F., Moser, D.P., Lin, L.H., Lacrampe-Couloume, G., Bonin, A.S., Davidson, M., Hall, J.A., Mislowack, B., Bellamy, R.E.S., Onstott, T.C., and Sherwood Lollar, B. (2004). Microbial hydrocarbon gases in the Witwatersrand Basin, South Africa: Implications for the deep biosphere. *Geochimica et Cosmochimica Acta* 68**,** 3239-3250.

Wartiainen, I., Hestnes, A.G., Mcdonald, I.R., and Svenning, M.M. (2006). Methylobacter tundripaludum sp. nov., a methane-oxidizing bacterium from Arctic wetland soil on the Svalbard islands, Norway (78° N). *International Journal of Systematic and Evolutionary Microbiology* 56**,** 109-113.

Weitemeyer, K.A., and Buffett, B.A. (2006). Accumulation and release of methane from clathrates below the Laurentide and Cordilleran ice sheets. *Global and Planetary Change* 53, 176-187.

Whiticar, M.J. (1999). Carbon and hydrogen isotope systematics of bacterial formation and oxidation of methane. *Chemical Geology* 161, 291-314.

Whitman, W.B., Coleman, D.C., and Wiebe, W.J. (1998). Prokaryotes: The unseen majority. *Proceedings of the National Academy of Sciences* 95, 6578-6583.

Wiesenburg, D.A., and Guinasso Jr, N.L. (1979). Equilibrium solubilities of methane, carbon monoxide, and hydrogen in water and sea water. *Journal of Chemical and Engineering Data* 24, 356-360.

Wilhelm, L., Singer, G.A., Fasching, C., Battin, T.J., and Besemer, K. (2013). Microbial biodiversity in glacier-fed streams. *ISME J* 7, 1651-1660.

Williams, T.J., Allen, M.A., Demaere, M.Z., Kyrpides, N.C., Tringe, S.G., Woyke, T., and Cavicchioli, R. (2014). Microbial ecology of an Antarctic hypersaline lake: genomic assessment of ecophysiology among dominant haloarchaea. *The Isme Journal* 8, 1645.

Wingham, D.J., Siegert, M.J., Shepherd, A., and Muir, A.S. (2006). Rapid discharge connects Antarctic subglacial lakes. *Nature* 440, 1033-1036.

Wynn, P.M., Hodson, A., and Heaton, T. (2006). Chemical and Isotopic Switching within the Subglacial Environment of a High Arctic Glacier. *Biogeochemistry* 78, 173-193.

Yvon-Durocher, G., Allen, A.P., Bastviken, D., Conrad, R., Gudasz, C., St-Pierre, A., Thanh-Duc, N., and Del Giorgio, P.A. (2014). Methane fluxes show consistent temperature dependence across microbial to ecosystem scales. *Nature* 507, 488.

Žárský, J.D., Kohler, T.J., Yde, J.C., Falteisek, L., Lamarche-Gagnon, G., Hawkings, J.R., Hatton, J.E., and Stibal, M. (2018). Prokaryotic assemblages in suspended and subglacial sediments within a glacierized catchment on Qeqertarsuaq (Disko Island), west Greenland. *FEMS Microbiology Ecology* 94, fiy100-fiy100.